Ca^{2+} cellular compartment-specific deficits in iPSC-derived neuronal models of Parkinson's disease



Maria Claudia Caiazza

Christ Church

Department of Physiology, Anatomy and Genetics

University of Oxford

A thesis submitted for the degree of

Doctor of Philosophy

Trinity 2022

To Michele and my parents

Acknowledgements

This work would have not happened without the continuous support and encouragement of those around me.

To my supervisor prof Richard Wade-Martins. Thank you for offering me the opportunity to join the lab and work on such an interesting and challenging project. Thank you for the discussions, the guidance and the encouragement that have allowed me to grow as a scientist. To my supervisor and friend Dr Charmaine Lang. Thank you for your support both in and out of the lab. You have helped me find my confidence as a scientist.

I would like to thank my Transfer and Confirmation of Status assessors prof Stephanie Cragg and prof Grant Churchill for the helpful discussions over the years. I would like to thank my viva examiners prof Christopher Miller and prof Stephanie Cragg for their feedback and suggestions to improve my thesis, and for the enjoyable viva they conducted.

I would like to thank Dr Brent Ryan, Janine Brandes, Dr Ricardo Marquez Gomez and Parnaz Sharifi for the FASN collaboration. I would like to thank Nora Bengoa-Vergniory for the PLA experiment. I would like to thank Dr Becky Carlyle for the advice on mass spectrometry.

I would like to thank all the present and past members of the Wade-Martins lab. You have all contributed to making the lab an amazing place to work it. However, some special thanks will be needed. To Dr Brent Ryan, William McGuinness, Kaitlyn Cramb, Naroa Ibarra Aizpurua, Ana Belen-Malpartida, Stewart Humble, Rachel Heon-Roberts, Féodora Bertherat and Marta Madureira thank you for the chats and the advice on scientific and personal matters.

I would like to thank Nicholas and the Pitts-Tucker family Trust and Christ Church for funding my DPhil.

I would like to thank Daniel Ebner and Val Millar from the Target Discovery Institute, University of Oxford for technical support for calcium imaging on the INCELL platform.

To Cristina B, Cristina C, Alessio, Giammarco, Filippo, Giacomo and Cristina D who have supported me and encouraged me from all over the World.

To my husband Michele and my parents Rosanna and Peppe for always believing in me and always being there for me.

Abstract

Parkinson's disease is a neurogenerative disease characterised by the degeneration of dopaminergic neurons of the substantia nigra. I employ induced pluripotent stem cell-derived dopaminergic neurons from patients and controls to study cytotoxic mechanisms in Parkinson's disease.

Calcium is crucial in the regulation of many neuronal cellular processes, and even more so, in dopaminergic neurons where continuous calcium oscillations occur. This suggests that even small alterations in calcium homeostasis might be deleterious to dopaminergic neurons.

Therefore, I focused my attention on the role of intracellular calcium in the pathogenesis of Parkinson's disease. To this end, I employed compounds to stimulate intracellular calcium release in conjunction with Fura-2 AM to monitor gross changes in calcium dynamics, and organelle-entrapped genetically encoded calcium indicators to trace back the subcellular source of the defect in dopaminergic neurons derived from Parkinson's patients harbouring mutations in the *SNCA* and *GBA* genes respectively encoding for the protein α-synuclein and the enzyme β-glucocerebrosidase. From these experiments, it appeared that *SNCA*-Trp and *GBA-N370S* DAns display decreased intracellular calcium release upon ionomycin stimulation in a Fura-2 AM-based assay as well as decreased endoplasmic reticulum calcium release upon ionomycin stimulation using the ER Ca^{2+} sensor GCEPIA*er*. *SNCA*-Trp and *GBA-N370S* DAns also display decreased mitochondrial calcium uptake upon ionomycin stimulation using the mitochondrial Ca^{2+} sensor RGECO*mt*. Further investigation of the source of the deficit was pursued in a functional genetics experiment which employs CRISPRi knockdown of calcium channels and calcium regulators.

I also optimised a proteomic analysis of the endoplasmic reticulum membrane and the outer mitochondrial membrane using proximity bi-

otinylation. In APEX2-catalised proximity labelling subcellular proteomics, spatial resolution is obtained through genetic targeting of the peroxidase APEX2. The experimental design followed the one described by Prof Alice Ting laboratory and involved the use of an endoplasmic reticulum membrane-targeted APEX2 (ERM-APEX2) and an outer mitochondrial membrane-targeted APEX2 (APEX2-OMM) to label the two compartments as well as a cytoplasmic APEX2 (APEX-NES) as a control. I cloned these constructs into an all-in-one doxycycline-inducible PiggyBac transposon construct which I delivered to 3 control iPSC lines and 3 *SNCA* iPSC lines via nucleofection. We evaluated APEX2 activity in the cells using streptavidin blot analysis and optimised APEX2-biotinylated protein enrichment.

In collaboration with AstraZeneca, Janine Brandes and Dr Brent Ryan in the lab have recently screened more than 4000 compounds for their ability to recover the calcium response to ionomycin in *GBA-N370S* DAns using a Fura-2 AM-based assay. This screening highlighted a novel potential druggable target for Parkinson's disease in FASN. In this thesis, I evaluated the ability of FASN inhibitors to revert other phenotypes in *GBA-N370S* DAns. In particular, I focused on calcium handling defects in the endoplasmic reticulum using GCEPIA*er*. I also explored their efficacy against endoplasmic reticulum stress and autophagy defects.

Contents

1 Introduction **1**

1.1 Parkinson's Disease 1

1.1.1 Histopathological features of PD 2

1.1.2 Genetics of PD 4

1.1.3 Preferential vulnerability of DAns 7

1.2 Role of Ca^{2+} in PD 10

1.2.1 Cytoplasmic Ca^{2+} buffers 11

1.2.2 ER Ca^{2+} dynamics and function 12

1.2.3 Mitochondrial Ca^{2+} dynamics and function 13

1.2.4 Lysosomal Ca^{2+} dynamics and function 14

1.2.5 Ca^{2+} flux through the plasma membrane 15

1.2.6 Ca^{2+} and PD 16

1.3 Mitochondria-associated ER membranes in PD 19

1.3.1 MAMs and Ca^{2+} dynamics 20

1.3.2 MAMs and ER physiology 22

1.3.3 MAMs and mitochondrial physiology 22

1.3.4 MAMs and lipid biosynthesis 23

1.3.5 MAMs and autophagy 23

1.3.6 MAMs and PD 24

1.4 iPSC-derived neuronal models of PD [1] 27

1.4.1 The advent of cell reprogramming into iPSCs 28

1.4.2 Differentiation into DAns 28

1.4.3 iPSC-derived DAns for disease modelling 30

1.4.4 i^3 neurons for disease modelling 32

1.4.5 Pitfalls of iPSC-based models 33

1.5 Aims of the thesis 36

[1] Part of the content of this section is adapted from [Caiazza et al., 2020]

2 Materials and Methods **37**
2.1 Cell Culture . . . 37
2.1.1 Human iPSCs culture, expansion and cryopreservation . . . 37
2.1.1.1 Thawing iPSC . . . 37
2.1.1.2 Colony passaging of iPSCs to generate a masterstock 38
2.1.1.3 Single-cell passaging of iPSCs . . . 39
2.1.1.4 Cryopreservation of iPSCs . . . 40
2.1.2 Establishment of polyclonal human iPSC lines . . . 40
2.1.2.1 Nucleofection of iPSCs with PiggyBac constructs . 40
2.1.2.2 Selection of transgene-expressing cells . . . 41
2.1.3 DAns differentiation and mFPP cryopreservation . . . 42
2.1.3.1 Differentiation of DAns . . . 42
2.1.3.2 Viral transduction of dopaminergic neurons . . . 46
2.1.3.3 Cryopreservation of mFPP . . . 47
2.1.4 List of lines used . . . 48
2.1.5 Differentiation of i^3 neurons . . . 49
2.1.6 Materials . . . 49
2.2 Lentivirus packaging . . . 50
2.3 DNA manipulation . . . 50
2.3.1 Bacterial culture . . . 50
2.3.2 Preparation of chemically competent bacteria (Stbl3 E. coli) . 51
2.3.3 Transformation of chemically competent bacteria . . . 52
2.3.4 Generation of an insert using PCR (from template plasmid) for HiFi assembly . . . 53
2.3.4.1 Primer design for PCR amplification of the insert from a donor plasmid . . . 53
2.3.4.2 PCR reaction for PCR amplification of the insert from a donor plasmid . . . 54
2.3.5 gBlock design for HiFi cloning into I56-EF1α-mApple backbone 55
2.3.6 Generation of sgRNA inserts for restriction cloning into H25-U6-sgRNA-NucBlue backbone . . . 56
2.3.7 Linearisation of a backbone via restriction enzyme digestion 57
2.3.8 Agarose gel electrophoresis of DNA and DNA purification from gel . . . 59
2.3.9 HiFi DNA Assembly . . . 60

2.3.10 Ligation for restriction cloning of sgRNA inserts into H25-U6-sgRNA-NucBlue . . . 61
2.3.11 Colony screening via colony PCR . . . 61
2.3.12 DNA prepping . . . 62
2.3.13 Colony screening via sequencing . . . 63
2.3.14 Materials . . . 63
2.4 Ca^{2+} imaging in iPSC derived neuronal models . . . 73
2.4.1 Fura-2 AM Ca^{2+} imaging . . . 73
2.4.2 Ca^{2+} imaging using subcellular compartment-entrapped GECI 74
2.5 Other assays . . . 76
2.5.1 RT-qPCR . . . 76
2.5.2 Western Blot . . . 76
2.5.3 APEX2 labelling and pull-down . . . 77
2.6 Statistical Analysis . . . 77

3 Investigation of Ca^{2+} deficits in iPSC-derived DAns from PD patients 79
3.1 Introduction and aims . . . 79
3.2 Investigation of Ca^{2+} dynamics in DAns harbouring mutations in the *SNCA* or *GBA* genes using a Fura-2 AM-based assay . . . 82
3.3 Cloning of GECI into a lentiviral backbone . . . 85
3.4 Expression and photostability of GCEPIA*er* and RGECO*mt* in DAn . 87
3.5 Investigation of ER Ca^{2+} dynamics in DAns harbouring mutations in the *SNCA* or *GBA* genes using a GCEPIA*er*-based assay . . . 87
3.6 Investigation of mitochondrial Ca^{2+} dynamics in DAns harbouring mutations in the *SNCA* or *GBA* genes using a RGECO*mt*-based assay . . . 92
3.7 Single-cell distribution of the Ca^{2+} response in DAn . . . 95
3.8 Dose-response of Ca^{2+} channel modulators in DAns . . . 98
3.9 Pharmacological dissection of the ER Ca^{2+} deficit using CPA, chlorocresol and caffeine . . . 101
3.10 Discussion . . . 104

4 CRISPRi screening of genes involved ER and mitochondrial Ca^{2+} handling 109
4.1 Introduction and aims . . . 109
4.2 Generation of the ER and mitochondrial membrane protein CRISPRi panel . . . 113

4.3 Titration of the lentivirus driving the expression of the sgRNA 115
4.4 Investigation of the effect of the ER and mitochondrial Ca^{2+} CRISPRi panel on Ca^{2+} release using a Fura-2 AM-based assay in i^3 neurons 119
4.5 Establishment of dCas9-KRAB polyclonal patient-derived iPS cell lines 121
4.6 Discussion 124

5 Study of ER and mitochondrial membrane proteins using APEX2-based spatial proteomics 128
5.1 Introduction and Aims 128
5.2 ERM-APEX2, APEX2-OMM and APEX2-NES cloning into a Tet-ON expression system 132
5.3 Establishment of ERM-APEX2, APEX2-OMM and APEX2-NES polyclonal patient-derived iPS cell lines 133
5.4 Optimisation of ERM-APEX2, APEX2-OMM and APEX2-NES in iPSC-derived DAns 135
5.5 Preliminary mass spectrometry experiment to assess the ability of ERM-APEX2 to label ERM proteins in iPSC-derived DAns 137
5.6 Discussion 140

6 Evaluation of FASN as a novel target for PD 144
6.1 Introduction and Aims 144
6.2 Toxicity of FASN inhibitor 1 147
6.3 Effect of FASN inhibitor 1 on ER health 147
6.4 Effect of FASN inhibitor 1 on lysosomal health 150
6.5 Lipidomic analysis of FASN inhibitor 1-treated cells 151
6.6 Discussion 155

7 Discussion 158
7.1 Main findings and discussion 160
7.2 Conclusions and future directions 165

Bibliography 168

List of Figures

1.1 Ca^{2+} distribution in the cell 10
1.2 MAM functions in the cell 19
1.3 Applications for iPSC-derived neurons in PD 32

2.1 Schematics of cloning primer design 54
2.2 GECI Columbus analysis pipeline 75

3.1 *SNCA*-Trp and *SNCA-A53T* DAns display decreased intracellular Ca^{2+} release upon ionomycin stimulation in a Fura-2 AM-based assay 83
3.2 *GBA-N370S* but not *GBA-L444P* DAns display decreased intracellular Ca^{2+} release upon ionomycin stimulation in a Fura-2 AM-based assay 84
3.3 Cloning of GECIs into a lentiviral backbone 86
3.4 Expression of GCEPIA*er* and RGECO*mt* in DAn cultures 88
3.5 Photostability of GCEPIA*er* and RGECO*mt* in DAn cultures 89
3.6 *SNCA*-Trp DAn cultures display decreased ER Ca^{2+} levels upon ionomycin stimulation in a GCEPIA*er*-based assay 90
3.7 *GBA-N370S* DAn cultures display decreased ER Ca^{2+} levels upon ionomycin stimulation in a GCEPIA*er*-based assay 91
3.8 *SNCA*-Trp DAn cultures display decreased Ca^{2+} uptake into mitochondria upon ionomycin stimulation in a RGECO*mt*-based assay . 93
3.9 *GBA-N370S* DAn cultures display decreased Ca^{2+} uptake into mitochondria upon ionomycin stimulation in a RGECO*mt*-based assay . 94
3.10 TH^+ percentage of transduced cells and single-cell distribution of the Ca^{2+} response in DAns 96
3.11 Dose-response of Ca^{2+} channel modulators in DAns 99
3.12 Confirmation of expression of SERCA pumps and RyR 100
3.13 Pharmacological dissection of the ER Ca^{2+} deficit in *SNCA*-Trp and *GBA-N370S* DAns using CPA, chlorocresol and caffeine 102

3.14 Percentage of TH+ neurons in iPSC-derived DAn cultures 108

4.1 Cartoon depicting CRSPRi function 110
4.2 Cloning of sgRNAs into their lentiviral expression vector 115
4.3 Titration of the lentiviruses for the expression of sgRNA (batch #1) . 116
4.4 Titration of the lentiviruses for the expression of sgRNA (batch #2) . 117
4.5 Titration of the lentiviruses for the expression of sgRNA (batch #3) . 118
4.6 Effect of knock-down of ER and mitochondrial Ca^{2+}-related genes on Ca^{2+} dynamics 120
4.7 Generation of dCas9-KRAB polyclonal patient-derived iPS cell lines using a PiggyBac system 122

5.1 APEX2 catalysis of proximity biotinylation reaction 129
5.2 Proximity biotinylation for spatially-resolved proteomics 130
5.3 Cloning ERM-APEX2, APEX2-OMM and APEX2-NES into an all-in-one Tet-ON expression system 132
5.4 Generation of ERM-APEX2, APEX2-OMM and APEX2-NES polyclonal patient-derived iPS cell lines using a PiggyBac system 133
5.5 Diagram showing the lines generated 134
5.6 Optimisation of APEX2-NES, ERM-APEX2 and APEX2-OMM in iPSC-derived DAns 136
5.7 Mass spectrometry experiment to assess the ability of ERM-APEX2 to label ERM proteins in iPSC-derived DAn 138

6.1 Screening pipeline 145
6.2 ToxiLight assay to evaluate FASN inhibitor 1 toxicity 147
6.3 Effect of FASN inhibitor 1 on ER health 148
6.4 Effect of FASN inhibitor 1 on lysosomal function using a DQ BSA-based assay 150
6.5 Effect of FASN inhibitor 1 on lysosomal function using a DQ BSA-based assay 152
6.6 Effect of FASN inhibitor 1 on phospholipids levels 153

7.1 Thesis outline 159
7.2 Proximity ligation assay showing the interaction between MAMs proteins IP3R and VDAC1 163
7.3 Summary of the observations made in this Thesis and future directions 164

List of Tables

1.1 Principal genetic variants associated with PD. Adapted from [Hernandez et al., 2016] 6
1.2 Summary of the main VGCC subunits expressed in the brain [Schampel and Kuerten, 2017] 16
1.3 Non-comprehensive list of cellular phenotypes discovered in iPSC-derived neurons from different genetic backgrounds 31

2.1 Composition of the iPSC freezing medium 40
2.2 Antibiotic selection of transfected iPSCs 42
2.3 DAns differentiation protocol media 42
2.4 Basal media composition 46
2.5 Coating volumes 46
2.6 Amount of DAns plated per well 47
2.7 Feeding and mitomycin C volumes 47
2.8 Composition of the mFPP freezing medium 48
2.9 List of lines used 48
2.10 List of reagents used for cell culture 49
2.11 Buffer used for the preparation of competent bacteria 51
2.12 Reagents used for the amplification of an insert of interest from a donor plasmid 54
2.13 PCR conditions for the amplification of an insert from a donor plasmid 55
2.14 Reagents used for oligonucleotides annealing 57
2.15 Reagents used to prepare 2X annealing buffer 57
2.16 Reagents used for the digestion of I56-EF1α-mApple 58
2.17 Reagents used for the digestion of K4-PB-TO-hNGN2 58
2.18 Reagents used for the digestion of H25-U6-sgRNA-NucBlue 59
2.19 Reagents used for 1 ml of NEB buffer 2.1-to-3.1 spike (6X) 59

2.20 Agarose concentrations used to separate DNA fragments of different sizes 59
2.21 Reagents used for HiFi DNA assembly 60
2.22 Reagents used for ligation of sgRNA inserts into H25-U6-sgRNA-NucBlue 61
2.23 PCR conditions for the amplification of an insert from a donor plasmid 62
2.24 List of reagents used for DNA manipulation 63
2.25 List of plasmids used in this thesis. The following abbreviations are used in the Table: A.O. for annealed oligonucleotides and Rest. C. for restriction cloning 65
2.26 List of primers used for cloning 71

4.1 List of genes included in the ER and mitochondrial membrane CRISPRi panel 111
4.2 List of guides included in the ER and mitochondrial membranes proteins panel 113

Abbreviations

AUC	Area under the curve
BDNF	Brain-derived growth factor
Ca^{2+}	Calcium
CICR	Ca^{2+}-induced Ca^{2+} release
CPA	Cyclopiazonic acid
DA	Dopamine
DAn	Dopaminergic neuron
DAT	Dopamine transporter
db-cAMP	Dibutyryl-cAMP
ddH_2O	Double-distilled water
ER	Endoplasmic reticulum
ERM	ER membrane
FASN	Fatty-acid synthase
FFA	Free fatty acid
FGF8	Fibroblast growth factor 8
GCase	β-Glucocerebrosidase
GDNF	Glia-derived growth factor
GECI	Genetically-encoded Ca^{2+} indicators
GWAS	Genome-wide association analysis
IMM	Inner mitochondrial membrane
IP3	Inositol trisphosphate
IP3R	IP3 receptor
iPSC	Induced pluripotent stem cell
MCU	Mitochondrial calcium uniporter
mFPP	Midbrain floorplate progenitors
NEAA	Non-essential amino acids
OD_{600nm}	Optical density at 600 nm
OMM	Outer mitochondrial membrane

PBS	Phosphate-buffered saline
PD	Parkinson's disease
RCF	Relative centrifugal force
ROS	Reactive oxygen species
RT	Room temperature
RyR	Ryanodine receptor
SERCA	Sarco/endoplasmic reticulum Ca^{2+}-ATPases
SHH	Sonic hedgehog
SNpc	Substantia nigra pars compacta
SOCE	Store-operated Ca^{2+} channel
TGFβ	Transforming growth factor β
TH	Tyrosine hydroxylase
UPR	Unfolded protein response
VDAC	Voltage-dependent anion channels
VMAT2	Vesicular monoamine transporter 2
VTA	Ventral tegmental area

Chapter 1

Introduction

1.1 Parkinson's Disease

Parkinson's disease (PD) is the second most common neurodegenerative disease affecting 0.3% of the world's population. It is an age-related condition with a prevalence increasing to 1.5% in those over 70 [Pringsheim et al., 2014]. PD is classically associated with motor symptoms such as bradykinesia, resting tremor and rigidity, but encompasses several non-motor symptoms such as anhedonia, sleep disorders, olfactory dysfunction and gastrointestinal symptoms all of which severely affect one's quality of life [Jankovic, 2008].

Despite the high prevalence of PD in our population, and the prediction that the number of patients might increase dramatically with life expectancy [Dorsey and Bloem, 2018], this disabling disease is still incurable. This makes the study of PD disease mechanisms and the development of disease-modifying treatments that can slow or even halt the progression of the disease one of our top priorities.

1.1.1 Histopathological features of PD

PD is a neurodegenerative disease and histologically it is characterised by the progressive degeneration of dopaminergic neurons (DAns) of the *substantia nigra pars compacta* (SNpc). DAns are characterised by the release of dopamine (DA), their primary neurotransmitter. They can be identified by the expression of enzymes and other proteins involved in the synthesis, the vesicle loading and the reuptake of the released DA. One of the most used markers to identify DAns is tyrosine hydroxylase (TH), the rate-limiting enzyme for synthesising DA and the other catecholamines. DA is loaded into synaptic vesicles by the vesicular monoamine transporter 2 (VMAT2) and the process reuptake from the extracellular space after release is carried out by the dopamine transporter (DAT). Using these markers it was possible to localise DAn in the nervous system; three distinct populations – namely A8 in the retrorubral field, A9 in the SNpc and A10 in the ventral tegmental area – were identified in the midbrain. More recently it has been suggested that these anatomically-identified classes are quite inhomogeneous and can be further divided into subclasses [Kamath et al., 2022]. However, it is still widely accepted that the degeneration mostly affects A9 neurons and that their loss is at the origin of the motor symptoms of the disease. The degeneration of DAns of the SNpc may cause a dysfunction of the circuitry in which these cells are involved, i.e. the basal ganglia loop.

The basal ganglia loop is a circuitry involved in motor control. Some nuclei of the basal ganglia (the striatum, the globus pallidus, the *substantia nigra pars reticulata* and the SNpc), the thalamus – that relays information to the cortex – and the motor cortex contribute to this circuitry. In particular, the DAns of the SNpc exert a crucial modulatory function in this network, therefore, it is believed that the loss of these neurons may cause defects in the motor regulation circuit [Rodriguez-Sabate et al., 2021].

DAns are responsible for the modulation of the activity of medium spiny neurons in the striatum. DAns resort to two different types of electrical activity; in steady conditions, DAns display a tonic, low-frequency spiking activity, while in the presence of salient stimuli DAns present burst firing that can reach up to 80 Hz in frequency. The DA tone can be increased by the phasic, high-frequency activity of DAn in the presence of a salient stimulus, which results in the facilitation of the initiation of a movement [Duda et al., 2016].

Other cell types in different regions of the brain have been also been reported to specifically degenerate in PD. Several other nuclei of the midbrain and of the hindbrain appear to be affected, including cholinergic neurons in the pedunculopontine nucleus, noradrenergic neurons in the locus coeruleus, cholinergic neurons in the nucleus basalis of Meynert and others. Degeneration of the olfactory bulb has been observed and linked to the early olfactory dysfunction observed in PD. Unfortunately, to date, the order of neuronal loss in the disease is still not clear. However, it is thought that studying commonalities between the affected areas could provide insight into the specific vulnerability mechanisms that lead to cell loss in PD [Giguère et al., 2018].

Another histopathological feature of PD is the accumulation of macromolecule aggregates called Lewy bodies and Lewy neurites. These inclusions appear to have a strong proteinaceous component, which includes the protein α-synuclein [Spillantini et al., 1998], and others including ubiquitin [Kuzuhara et al., 1988]. Lewy pathology also displays a lipid component made up of membranes and organelles [Shahmoradian et al., 2019]. Lewy pathology is very heterogeneous by nature, however, it is believed that α-synuclein aggregation might be at the core of Lewy pathology and ultimately responsible for the further aggregation of the other components and for the spreading of the disease [Visanji et al., 2013]. In particular,

it is thought that α-synuclein can form small toxic oligomers that can then further aggregate into Lewy bodies.

Lewy pathology in the central nervous system appears to originate in the medulla oblongata and then spread in a pretty reproducible fashion through the connectome to other vulnerable areas [Braak et al., 2003]. Regions that are not afflicted by Lewy pathology can display α-synuclein oligomerisation, which corresponds to an early sign of aggregation [Roberts et al., 2015].

1.1.2 Genetics of PD

Age is the major risk factor for PD, but also a number of genetic risk factors have been described over the years. Traditionally, PD is classified as familial and sporadic/idiopathic, the former being often associated with a rare and potentially causative monogenic factor and the latter appearing in the population without a clear cause. The first genetic variant to be associated with PD was a point mutation (A53T) in the gene *SNCA* encoding for the protein α-synuclein. Originally, loci associated with familial PD were named *PARK* loci and the candidate genes called *PARK* genes. *SNCA* corresponds to *PARK1* and *PARK4* and to date a total of 18 *PARK* genes have been discovered (see Table 1.1) [Hernandez et al., 2016]. Of particular interest for this thesis is the *PARK* gene *SNCA*, which encodes for α-synuclein a synaptic protein at the core of Lewy pathology in PD. Others include *LRRK2*, which encodes for LRRK2, a multidomain protein containing kinase, GTPase and scaffolding functions; it is proposed to be involved in protein trafficking and autophagy, both of which are altered in PD, and *PINK1* and *PRKN* which encode for Pink1 and Parkin which are involved in mitophagy.

More recently, it has become clear that the genetics of PD is more complex than originally imagined. It is estimated that the *PARK* genes only account for about 30% of familial cases [Kumar et al., 2011]. In addition, even when a clear, large

effect-size genetic factor can be found to be associated with the development of the symptomatic disease, the pattern of inheritance of the disease can be complicated by incomplete penetrance, which causes some mutation carriers to never develop the disease; for example, this is the case for mutations in the *LRRK2* gene, which cause PD with a dominant pattern of inheritance, but with just 30% penetrance which increases to 75% in those over 80 [Healy et al., 2008]. Finally, even for highly penetrant mutations, the age of onset of the disease or the severity of the symptoms can vary from patient to patient. This evidence suggests that even for monogenic PD other genetic or environmental risk factors must play a role.

Conversely, in recent years, genome-wide association studies (GWAS) have suggested a potential involvement of genetic risk factors in the development of idiopathic PD. GWAS highlighted a number of genetic variants at different loci which are enriched in PD patients. It is thought that individually these risk factors have a small effect on the development of the disease, but that a combination of several risk factors can contribute to a genetic landscape that is favourable to the apparently sporadic appearance of symptomatic PD. To date, 90 risk factors have been highlighted by GWAS. These include the *SNCA* and the *LRRK2* genes, which appear to be the site of several rare causative mutations and also the site of common variants that can modify vulnerability to PD [Nalls et al., 2019]. Other GWAS hits include the genes *GBA*, *SCARB2* and *MAPT*. *GBA* encodes for the enzyme β-glucocerebrosidase (GCase), a lysosomal hydrolytic enzyme that – when mutated – is associated with lysosome and autophagy dysfunction in PD, *SCARB2* encodes for LIMP2 which is involved in endolysosomal transport and is thought to be able to chaperone GCase to the lysosomes [Reczek et al., 2007] and *MAPT* encodes for Tau protein that is involved in Alzheimer's disease and other tauopathies.

Table 1.1: Principal genetic variants associated with PD. Adapted from [Hernandez et al., 2016]

Locus	Gene	Protein	Inheritance
PARK1/4	*SNCA*	α-synuclein	Autosomal dominant
PARK2	*PRKN*	Parkin	Autosomal recessive
PARK3	*Unknown*	Unknown	Autosomal dominant
PARK5	*UCHL1*	Ubiquitin c terminal hydrolase	Autosomal dominant
PARK6	*PINK1*	Pink1	Autosomal recessive
PARK7	*DJ-1*	DJ-1	Autosomal recessive
PARK8	*LRRK2*	LRRK2	Autosomal dominant
PARK9	*ATP13A2*	Lysosomal type 5 ATPase	Autosomal recessive
PARK10	*Unknown*	Unknown	Risk locus
PARK11	*GIGYF2*	GRB interacting GYF protein 2	Autosomal dominant
PARK12	*Unknown*	Unknown	X-linked
PARK13	*HTRA2*	HTRA serine peptidase 2	Autosomal dominant
PARK14	*PLA2G6*	Phospholipase A2	Autosomal recessive
PARK15	*FBXO7*	F-box only protein 7	Autosomal recessive
PARK17	*VPS35*	Vacuolar protein sorting 35	Autosomal dominant
PARK18	*EIF4G1*	Eukaryotic translation initiation factor 4 gamma 1	Autosomal dominant
PARK19	*DNAJC16*	DNAJ/HSP40 homolog subfamily C member 6	Autosomal recessive
–	*SNCA*	α-synuclein	Risk locus
–	*LRRK2*	Leucine-rich repeat kinase 2	Risk locus
–	*GBA*	GCase	Risk locus
–	*SCARB2*	LIMP2	Risk locus
–	*MAPT*	Tau protein	Risk locus

Over the years, it has become clear that PD has complex aetiology where genetics may play a crucial role. However, it has also become clear that patients can have very inhomogeneous genetics which may make disease modelling very complex. On one hand, one may be tempted to rely on causative or large effect size mutations, which can be introduced in *in vivo* and *in vitro* traditional models and may be associated with large phenotypic effects. On the other, data show even the effect of these mutations can be influenced by other genetic risk factors. Therefore, in this Thesis stem-cell models derived from patients – and therefore carrying the whole genetic background of these patients – are used to model PD (see Sec-

tion 1.4). In particular, patients bearing mutations in the *SNCA* and *GBA* genes were selected as α-synuclein and GCase pathologies are thought to be common features of PD.

1.1.3 Preferential vulnerability of DAns

Degeneration of DAns of the SNpc appears to be responsible for the motor symptoms among the clinical manifestations of PD. There is a big enthusiasm around trying to address the motor symptoms of PD. Therefore, there is an increasing interest in trying to understand what makes these neurons especially vulnerable.

Recently, there has been increasing interest in integrating single-cell RNA sequencing (scRNA-seq) with GWAS data with the ultimate goal of demonstrating that SNpc DAns are enriched for the expression of genetic risk factors for PD [Agarwal et al., 2020, Kamath et al., 2022] (see Section 1.1.2 for more details on the genetic bases of PD). The fact that genes that have been linked to increased risk of PD are highly expressed in DAn suggests that, in a PD patient, the gene variant that might have contributed to the development of the disease was mostly expressed and therefore might have had a greater chance to exert its negative effect in the very DAns. This piece of evidence suggests that there might be an intrinsic vulnerability mechanism afflicting SNpc DAns and that PD research might benefit from an improved human SNpc DAn model of PD (see Section 1.4)

It is also thought that the peculiar metabolic needs of SNpc DAns may contribute to their specific vulnerability.

Firstly, DAns might be more vulnerable simply because of the use of DA as a neurotransmitter. DA can be oxidised in the cell to quinones that appear to impact on mitochondrial and lysosomal function [Burbulla et al., 2017]. It is thought that during the progression of the disease, VMAT2 decreases and – with less DA being

loaded into the vesicles – more DA is left in the cytoplasm to be oxidised into the toxic quinones [Giguère et al., 2018].

In addition, DAns display a very big and complex axonal arbour to innervate the striatum to help maintain DA tone in the striatum. The sheer size of the axonal arbour is thought to increase the metabolic demand of DAns and their proteostatic burden, therefore exposing these cells to vulnerability [Giguère et al., 2018].

Finally, in order to maintain DA tone in the striatum, DAns rely on autonomous action potentials. These action potentials are autonomous as they do not require synaptic input. Despite the sustained electrical activity and DA release being effective at maintaining high DA levels in the striatum, a drawback is that DAns require high energy levels to restore intracellular ion concentrations and recycle neurotransmitters.

The pacemaking activity of DAns is accompanied and sustained by intracellular calcium (Ca^{2+}) oscillations due to the presence of L-type Ca^{2+} channels at the plasma membrane of DAns. SNpc DAns are characterised by very poor cytoplasmic Ca^{2+} buffering, even when compared to other DAn such as ventral tegmental area (VTA) neurons. This is due to the low expression of Ca^{2+}-buffering proteins like calbindin [Foehring et al., 2009, Dopeso-Reyes et al., 2014].

Because of the low intrinsic Ca^{2+}-buffering properties of SNpc DAns, in these cells, Ca^{2+} is buffered mostly by the endoplasmic reticulum (ER) and mitochondria. It is actually thought that this element is crucial to meet the high energy demand of the cell; the poorly buffered Ca^{2+} oscillations cause a Ca^{2+} influx into the mitochondria where Ca^{2+} ions activate enzymes of the citric acid cycle (namely pyruvate-, isocitrate-, and α-ketoglutarate dehydrogenases), *de facto* increasing energy production [Díaz-García et al., 2021].

The increased citric acid cycle activity and the subsequent increase in oxidative phosphorylation driven by the Ca^{2+} oscillations may help DAns meet their

high energy demand. However, sustained oxidative phosphorylation may cause an increase in reactive oxygen species (ROS) production, thus making DAns particularly vulnerable to oxidative stress [Görlach et al., 2015].

Despite Ca^{2+} oscillations may help DAns meet their energy needs, the continuous Ca^{2+} oscillations occurring in DAns place them in an environment where even small alterations in Ca^{2+} homeostasis and dynamics might impact cellular function. Therefore, a number of works summarised in Section 7 have been published over the years to try and elucidate the role Ca^{2+} in PD.

1.2 Role of Ca^{2+} in PD

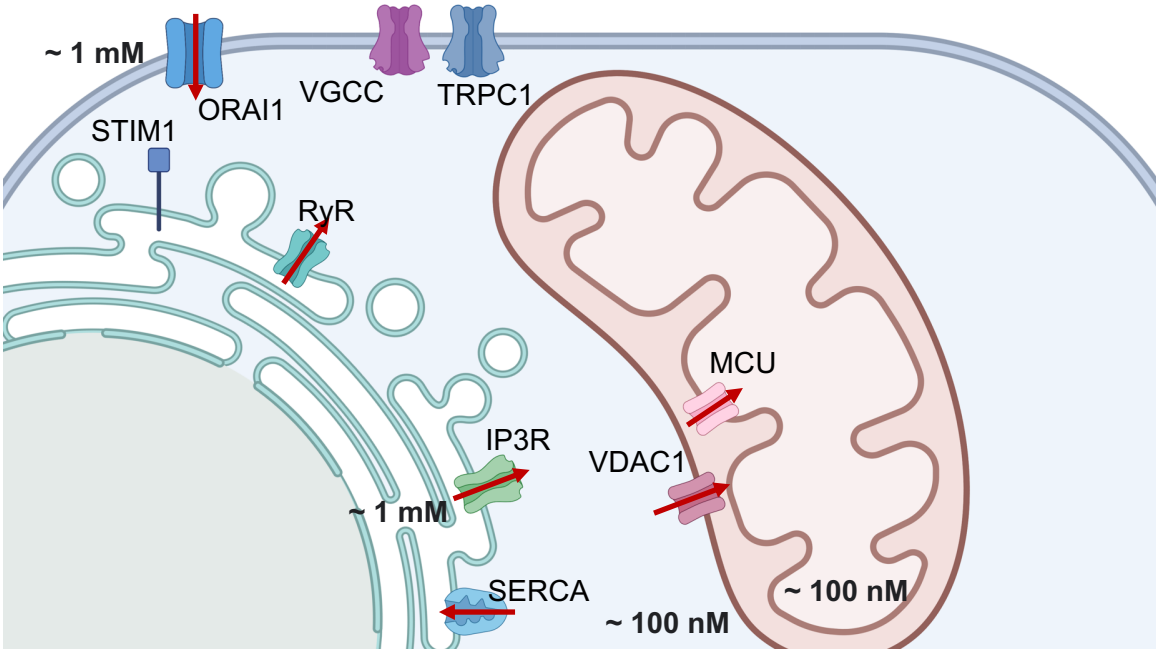


Figure 1.1: Ca^{2+} distribution in the cell

Ca^{2+} concentration in the cell is tightly regulated. Here are depicted some of the crucial players in Ca^{2+} regulation and Ca^{2+} concentration in the different compartments.

Ca^{2+} is a key signalling molecule involved in a plethora of cellular functions such as signal transduction, gene regulation, metabolism and autophagy. In neurons, Ca^{2+} is involved in synaptic transmission, neurotransmitter release and synaptic plasticity. Moreover, in DAns, L-type Ca^{2+} channels support their crucial pace-maker activity. The continuous Ca^{2+} oscillations occurring in DAns, however, place them in an environment where even small alterations in Ca^{2+} homeostasis and dynamics might impact cellular function. Therefore Ca^{2+} signalling and shuttling in the cells have drawn the attention of researchers in the field of PD.

Ca^{2+} levels are tightly regulated in the cell. The cellular milieu is characterised by high Ca^{2+} concentration, in the molar range, while cytoplasmic free-Ca^{2+} has been measured to be in the 100 nM range [Clapham, 2007] 1.1. Low cytoplasmic Ca^{2+} concentrations are maintained thanks to a fine-tuned system of regulation

that involves cytoplasmic proteins with Ca^{2+} buffering capacity, short-term storage in organelles (mostly mitochondria and lysosomes), long-term storage in the ER and extrusion in the extracellular space.

The maintenance of low levels of cytoplasmic Ca^{2+} makes this molecule a perfect candidate for cell signalling and regulation of cellular functions.

1.2.1 Cytoplasmic Ca^{2+} buffers

Many proteins have Ca^{2+}-binding domains. The most common Ca^{2+}-chelating structures are called EF-hand domains; they consist of helix-turn-helix structures characterised by the presence of negatively charged amino acids that coordinate the Ca^{2+} ions [Clapham, 2007].

Other common Ca^{2+}-binding domains are the C2 domains. Ca^{2+}-binding to these domains creates a charge imbalance that makes the protein particularly affine to the negatively charged cytoplasmic sides of the outer mitochondrial membrane (OMM) and of the cell membrane [Clapham, 2007].

Among the most expressed Ca^{2+} buffers in the brain are calmodulin, calbindin, calretinin and parvalbumin, all involved in Ca^{2+} signalling. Evidence shows that – in rodents – calmodulin and calretinin are expressed in DAns of the SNpc [Kamata et al., 2006, Shioda et al., 2015, González-Hernández and Rodríguez, 2000]. Calbindin appears to be expressed in DAns in the midbrain, but it appears to be enriched in the VTA [Poulin et al., 2014, Kamath et al., 2022]. Parvalbumin does not appear to be expressed in DAns of the SNpc [Alfahel-Kakunda and Silverman, 1997].

1.2.2 ER Ca^{2+} dynamics and function

ER Ca^{2+} is kept in the mM range (Figure 1.1), where it regulates the function of several ER chaperones and can be released upon stimulation.

Ca^{2+}release from the ER is accomplished by two main ligand-gated Ca^{2+} channels, i.e. inositol trisphosphate receptors (IP3R) and ryanodine receptors (RyR) (Figure 1.1).

Ca^{2+} is pumped into the ER against a gradient by sarco/endoplasmic reticulum Ca^{2+}-ATPases (SERCA pumps) (Figure 1.1). SERCA pumps are monomeric and exist in 7 different isoforms encoded by the paralog genes *ATP2A1*, *ATP2A2* and *ATP2A3* [Periasamy and Kalyanasundaram, 2007].

When a G_q-coupled receptor at the plasma membrane is stimulated, its α subunit activates the phospholipase C which catalyses the hydrolysis of phosphatidylinositol bisphosphate into diacylglycerol and IP3. IP3 increases the opening probability of IP3R, thus inducing ER Ca^{2+} efflux through the ER membrane (ERM) into the cytoplasm.

IP3 receptors are heterotetrameric channels and their subunits exist in three different subtypes expressed by the paralog genes *ITPR1*, *ITPR2* and *ITPR3*. The channel is positively modulated by IP3 and low cytoplasmatic Ca^{2+} concentrations and negatively modulated by high cytoplasmatic Ca^{2+} concentrations [Chandrasekhar et al., 2016].

When cytoplasmic Ca^{2+} levels are increased, RyRs increase their opening probability to reinforce the signal for a mechanism known as Ca^{2+}-induced Ca^{2+} release (CICR).

RyRs are homotetrameric channels and their subunits exist in three different

subtypes expressed by the paralog genes *RYR1*, *RYR2* and *RYR3*. The channel is positively modulated by high cytoplasmatic Ca^{2+} [Lanner et al., 2010].

When ER Ca^{2+} levels are depleted, a mechanism called store-operated Ca^{2+} entry (SOCE) is initiated.

STIM1 and STIM2 are single-pass ERM integral proteins encoded by the genes *STIM1* and *STIM2* (Figure 1.1). They have a Ca^{2+} sensing domain on the ER side of the ERM and when ER Ca^{2+} levels are depleted it activates and contacts Orai [Prakriya and Lewis, 2015] (Figure 1.1).

Orai channels are Ca^{2+} channels located in the plasma membrane, and they exist in three different subtypes encoded by *ORAI1*, *ORAI2* and *ORAI3*. When STIM contacts Orai, Orai opens which results in Ca^{2+} influx through the cell membrane [Prakriya and Lewis, 2015]. The opening of the Orai channels can create a large Ca^{2+} flux into the cytoplasm of the cell, and said Ca^{2+} can then be pumped back into the ER by SERCA to replenish ER Ca^{2+} levels.

1.2.3 Mitochondrial Ca^{2+} dynamics and function

Mitochondrial Ca^{2+} is kept in the 100 nM range (Figure 1.1), where it regulates the function of pyruvate-, isocitrate-, and α-ketoglutarate dehydrogenases – enzymes of the citric acid cycle – which need Ca^{2+} as a cofactor for their function. Mitochondrial Ca^{2+} influx has also a role in programmed cell death.

Ca^{2+} permeability through the OMM is granted by voltage-dependent anion channels (VDACs) (Figure 1.1). This pore exists in three different isoforms encoded by the genes *VDAC1*, *VDAC2* and *VDAC3*. VDAC has a very heterogeneous permeability which includes organic anions. Interestingly VDAC is permeable to Ca^{2+} in its closed conformation [Camara et al., 2017]. VDAC1 was found to inter-

act with IP3R, therefore VDAC1 uptakes Ca^{2+} upon IP3R opening, which creates a high local Ca^{2+} concentration.

Ca^{2+} ions cross the inner mitochondrial membrane (IMM) following the electrochemical gradient through the mitochondrial Ca^{2+} uniporter (MCU) (Figure 1.1), a low-affinity transporter. In order to reach the elevated Ca^{2+} concentrations needed by MCU to transfer Ca^{2+} the cell relies on the high Ca^{2+} concentration generated upon IP3R stimulation at the IP3R-VDAC1 contact sites [Rizzuto et al., 1998, Szabadkai et al., 2003].

MCU activity is regulated by MICU1 and MICU2 at the IMM [Tanwar et al., 2021].

Mitochondrial Ca^{2+} levels are maintained thanks to the action of $Na^{+}Ca^{2+}$ exchangers (NCX). These pumps are located in the IMM and extrude one Ca^{2+} ion in exchange for three Na^{+} ions thus creating a net charge at the IMM [Tanwar et al., 2021].

1.2.4 Lysosomal Ca^{2+} dynamics and function

Lysosomal Ca^{2+} concentration is thought to average around 500 nM, where it plays a crucial role in autophagy regulation.

Ca^{2+} is regulated by two families of channels, i.e. two-pore channels (TPC) encoded by the genes *TPCN1* and *TPCN2* and transient receptor potential mucolipin 1 (TRPML1) encoded by the gene *MCOLN1*. TPCs release Ca^{2+} into the cytoplasm in response to NAADP, whereas TRPML channels release Ca^{2+} in response to phosphatidylinositol bisphosphate [Medina, 2021]

1.2.5 Ca^{2+} flux through the plasma membrane

Cytoplasmic Ca^{2+} levels are tightly regulated. We have mentioned the role of Ca^{2+}-binding proteins and organelles in Ca^{2+} buffering, and the role of the ER in Ca^{2+} release upon stimulation. However, a number of Ca^{2+} channels and pumps are involved in the generation of a Ca^{2+} signal and the subsequent restoration of steady-state cytoplasmic Ca^{2+} concentration.

The cell relies on NCX and on the plasma membrane Ca^{2+} pump (PMCA) to extrude Ca^{2+} through the plasma membrane.

Plasma membrane NCX acts similarly to mitochondrial NCX; it exchanges one Ca^{2+} ion for three Na^{+} ions, therefore it dissipates the Na^{+} gradient generated by the Na^{+}/K^{+} ATPase to extrude Ca^{2+} against a gradient of concentration. This exchanger shows a low affinity to Ca^{2+} and therefore works best at high intracellular Ca^{2+} concentrations [Brini and Carafoli, 2010].

PMCA is an ATPase that uses ATP to pump Ca^{2+} out of the cell. It has a high affinity to Ca^{2+} and therefore works best at lower Ca^{2+} concentrations than NCX. There are four different isoforms of PMCA encoded by *PMCA1*, *PMCA2*, *PMCA3* and *PMCA4* [Brini and Carafoli, 2010].

Ligand-gated ion channels are crucial for neuronal function as many neurotransmitters bind and activate them to change membrane polarisation. Several cation-permeable channels are permeable to Ca^{2+}. For example, NMDA receptors, some AMPA receptor subtypes, purinergic receptors and nicotinic acetylcholine receptors are permeable to Ca^{2+} and therefore contribute to the Ca^{2+} spikes in the cell [Pankratov and Lalo, 2014].

Voltage-gated Ca^{2+} channels (VGCCs) are also crucial for neuron function as

Table 1.2: Summary of the main VGCC subunits expressed in the brain [Schampel and Kuerten, 2017]

Type	Voltage	Compartment	Subunit (gene name)
L-type	High voltage activated	Somato-dendritic	Cav1.2 (*CACNA1C*) Cav1.3 (*CACNA1D*)
P/Q-type	High voltage activated	Axonal	Cav2.1 (*CACNA1A*)
N-type	High voltage activated	Axonal	Cav2.2 (*CACNA1B*)
R-type	Intermediate voltage activated	Somato-dendritic	Cav2.3 (*CACNA1E*)
T-type	Low voltage activated	Somato-dendritic	Cav3.1 (*CACNA1G*) Cav3.2 (*CACNA1H*) Cav3.3 (*CACNA1I*)

they contribute to neurotransmitter release, membrane depolarisation and changes in gene expression. They are expressed in excitable cells such as muscle cells, neurons and some glial cells. They are divided into five main classes and each class encompasses several subunits. Table 1.2 summarises the main subunits found in the brain, their subcellular compartment and their physiological properties in neurons. Generally, P/Q and N-type VGCCs are considered to be the most involved in neurotransmitter release as they interact with SNARE proteins [Kim and Catterall, 1997]. However, an increasing body of evidence suggests that L and T-type VGCCs are involved in DA release [Brimblecombe et al., 2015].

1.2.6 Ca^{2+} and PD

PD patients show signs of ER stress, which can be caused by ER Ca^{2+} depletion. Interestingly, in a fly model of PD, it has been shown that oxidative stress can cause the appearance of aberrant post-translational modifications of intracellular proteins and affect their function. In particular, this was the case for SERCA pumps, which appeared to be less functional than in controls. This has the potential to result in increased cytoplasmic Ca^{2+} and reduced ER Ca^{2+}, which may be the cause of ER stress in PD iPSC-derived DAns [Solana-Manrique et al., 2021].

Lysosomal Ca^{2+} is considered to be crucial to the initiation of autophagy [Boot-

man et al., 2018]. Autophagy has been demonstrated to be dysfunctional in a number of PD models, which has been correlated with changes in lysosomal Ca^{2+} release. Fibroblasts obtained from PD patients carrying the *GBA-N370S* mutation display decreased lysosomal Ca^{2+}. LRRK2 has been found to interact with and activate TPC, thus causing depletion of lysosomal $Ca^{2+}$and increased autophagosomal formation [Gómez-Suaga et al., 2011].

DAns pacemaking activity is associated with Ca^{2+} oscillations that occur thanks to VGCCs. These Ca^{2+} oscillations are thought to be associated with increased mitochondrial Ca^{2+} levels which boosts energy production. However, the increase in mitochondrial respiration as a consequence of the increased mitochondrial Ca^{2+} levels also causes an increase in ROS production thus increasing oxidative stress in the cell. This problem might be exacerbated in PD, as in several PD models L-type channels appear to be more expressed than in controls, thus causing an increase in intracellular Ca^{2+} oscillations [Hurley et al., 2013]. This theory is supported by epidemiological studies showing a protective effect of VGCC inhibitors against the development of PD [Pasternak et al., 2012]. It has been shown that other VGCC might be differentially expressed in PD [Benkert et al., 2019, Sharifi et al., 2022]. The Ca^{2+} oscillations are poorly buffered in the cytoplasm of SNpc DAns compared to others, for instance, SNpc DAns express lower levels of the Ca^{2+} buffer calbindin compared to the neighbouring VTA DAns.

Finally, α-synuclein has been shown to be more prone to aggregation in the presence of high Ca^{2+} levels [Lautenschläger et al., 2018]. Increased Ca^{2+} oscillations combined with poor cytoplasmic Ca^{2+}-buffering and decreased ER Ca^{2+} replenishment, can increase cytoplasmic free Ca^{2+}. This can increase α-synuclein tendency to aggregate and start the formation of Lewy bodies in PD.

All these pieces of evidence suggest that even small changes in Ca^{2+} dynamics might be extremely detrimental for DAns, and might be at the base of their

preferential vulnerability.

1.3 Mitochondria-associated ER membranes in PD

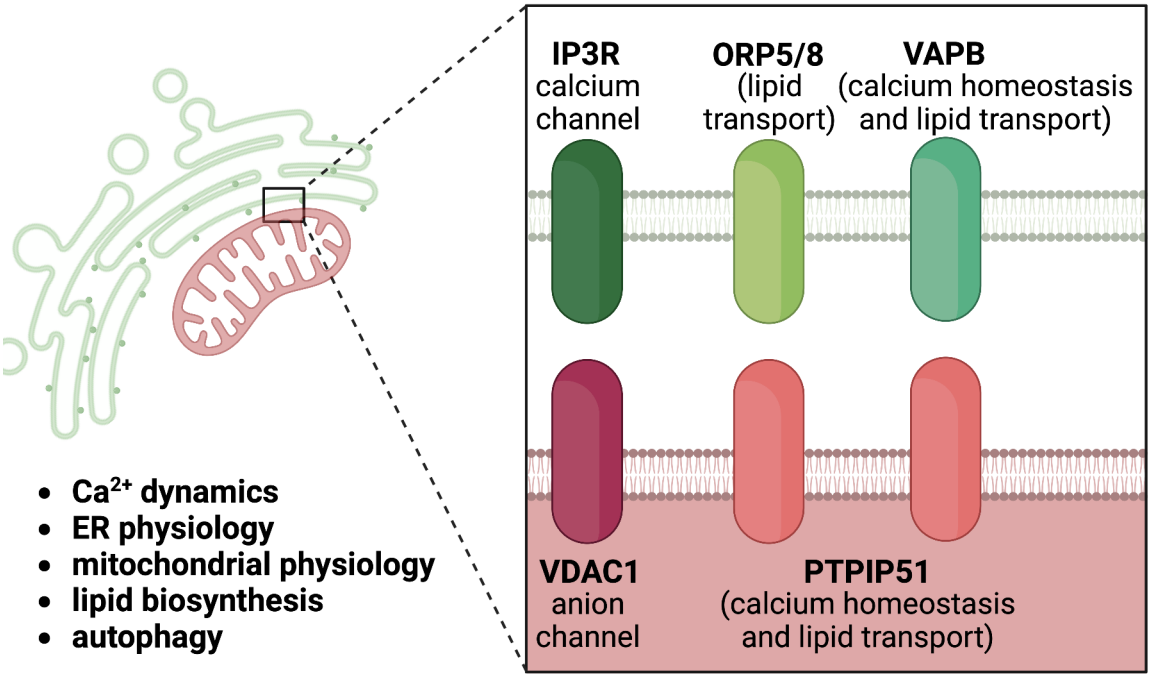


Figure 1.2: MAM functions in the cell

MAMs are regions where the ERM (green) and the OMM (red) are in close proximity. These regions are characterised by specific biochemistry, proteomics and physiology that distinguish them from other regions of the ERM and the OMM. Some of the most distinctive proteins and functions of MAMs are listed in the figure.

The ER is the biggest organelle of the cell and pervades it. In neurons, ER tubules have been observed even in the dendritic arbour [Cooney et al., 2002]. Besides being spatially pervasive, the ER also contacts several other organelles, such as mitochondria, Golgi, and lysosomes. These contacts do not involve membrane fusion, but rather they rely on membrane tethering into close proximity to favour the exchange of ions and macromolecules. The contacts are transient, highly dynamic and tunable, and they could be at the base of many cellular functions.

The first contact sites to be described were mitochondria-associated ER membranes (MAMs), and they are still the most widely studied. MAMs consist of juxtaposed ER and mitochondrial membranes that are tethered by specific proteins so that the membranes are 10 nm apart in regions of smooth ER and 25 nm in

regions of rough ER [Csordaś et al., 2006]. These contacts are quite extensive and in HeLa cells, it has been estimated that 5-20% of the total OMM surface is in contact with the ER [Rizzuto et al., 1998].

It is thought that MAMs have specific biochemical properties that distinguish them from the other ER domains; in particular, it has been shown that they are enriched in gangliosides, cholesterol and ceramides which suggests that they have lipid raft-like features [Sano et al., 2009, Hayashi and Fujimoto, 2010]. Lipid rafts are microdomains of membranes that are characterised by increased rigidity which is pivotal for certain transmembrane proteins function.

MAMs also appear to have specific functions which are distinguishable from those of other domains of the ER membrane, which will be expanded on in the following Sections. These functions are possible thanks to a distinctive proteome, which has been studied using different compartment-specific proteomic analyses, including recent works using proximity biotinylation to increase spatial resolution [Hung et al., 2017, Cho et al., 2020] . The specific proteome of the MAMs, includes a number of proteins of the ERM and OMM that interact and function as tethers between the two membranes [Csordas et al., 2018].

1.3.1 MAMs and Ca^{2+} dynamics

ER and mitochondria are the main Ca^{2+} stores of the cell. ER Ca^{2+} concentrations are several orders of magnitude higher than any other part of the cell and ER Ca^{2+} is used as a response to specific stimuli such as increased IP3 and Ca^{2+} levels. This is thought to be important for signal transduction and changes in gene expression. However, Ca^{2+} release from the ER is also used to refill mitochondrial Ca^{2+}. Most of these Ca^{2+}-handling activities take place at MAMs.

The ER Ca^{2+} channel IP3R is located at MAMs and is in touch with the VDAC1 channels at the OMM. When Ca^{2+} is released by IP3R, this creates a high local

concentration of Ca^{2+} called a Ca^{2+} puff, then Ca^{2+} moves across the OMM into the mitochondrion through the VDAC1 channel and then across the inner mitochondrial membrane following the electrochemical gradient through MCU, a low-affinity transporter. In order to reach the elevated Ca^{2+} concentrations needed by MCU to transfer Ca^{2+} the cell relies on the Ca^{2+} puffs at MAMs [Rizzuto et al., 1998, Szabadkai et al., 2003]. This mechanism is necessary for fast Ca^{2+} buffering after a signal and is crucial to increase mitochondrial Ca^{2+}. Increases in mitochondrial Ca^{2+} can result in increased energy production through boosting of the citric acid cycle and of oxidative phosphorylation, therefore ER-mitochondria Ca^{2+} shuttling is also pivotal for energy regulation.

MAMs are also involved in Ca^{2+} regulation in the ER. The ER luminal proteins calnexin and calreticulin are ER Ca^{2+}-sensing chaperones involved in the ER-associated degradation (ERAD) of misfolded proteins; they sense and bind to misfolded proteins in the ER and retain them in the ER lumen. However, calnexin and calreticulin are also able to change the structure of mature ER-resident proteins such as SERCA pumps and IP3Rs, and in this way, they can negatively modulate their function [John et al., 1998, Roderick et al., 2000, Higo et al., 2005]. The two chaperones tend to be confined in MAMs region, and the MAM protein PACS2 is responsible for the localisation of calnexin at MAMs [Myhill et al., 2008].

Another mechanism through which ER Ca^{2+} is modulated at MAMs is through the MAM-resident receptor Sigma-1 (Sig1R). Sig1R is a Ca^{2+}-sensing chaperone in the ER. Active Sig1R is also able to stabilise IP3R at MAMs, thus increasing ER-mitochondria Ca^{2+} shuttling [Hayashi and Su, 2007].

The ER-mitochondria tethering complex VAPB-PTPIP51 was demonstrated to modulate ER-mitochondria Ca^{2+} release [Vos et al., 2011].

ER-mitochondria Ca^{2+} release is tightly regulated, therefore it is thought that this might be a crucial physiological mechanism for signal transduction and metabolism. In fact, dysfunctions in the ER-mitochondrial Ca^{2+} exchange might have catastrophic consequences for the cell such as apoptosis [Pinton et al., 2008].

1.3.2 MAMs and ER physiology

One of the main functions of the ER is to synthesise and traffic membrane and secreted proteins. During this process, a number of chaperones help protein folding and – when folding fails – retain the misfolded and unfolded proteins in the ER and send them to degradation in a process called ERAD. If the number of misfolded proteins builds up, the ER starts a stress response called the unfolded-protein response (UPR). The outcome of the UPR is to increase the expression of ER chaperones, while overall decreasing transcription.

Interestingly, several ER chaperones and other players in the UPR reside in MAMs, making this region a hub for ER health. As mentioned in Section 1.3.1, the Ca^{2+}-sensing ER chaperones calreticulin, calnexin and Sig1R have a preferential localisation in MAMs. Ero1 is another crucial ER chaperone found in MAMs. Ero1 – together with PDI – is responsible for the formation of disulfide bonds [Shergalis et al., 2020].

1.3.3 MAMs and mitochondrial physiology

Mitochondria are highly dynamic organelles, which continuously undergo remodelling by dividing (fission) and joining together (fusion). These mechanisms are used to maintain a healthy mitochondrial network. Both fission and fusion initiate at and are modulated by MAMs. For example, MAM resident proteins Mfn1 and Mfn2 are involved in mitochondrial fusion, while Fis1 is involved in mitochondrial

fission [Westermann, 2008].

Mitochondrial dynamics also involves mitochondrial transportation to different parts of the cell. Miro1 is involved in mitochondrial trafficking and is located in MAMs [Modi et al., 2019].

Finally, mitophagy is the process through which damaged mitochondria are degraded. There are different pathways that lead to mitophagy, but the best characterised is the so-called PINK1/Parkin dependent-mitophagy. Both PINK1 and Parkin together with other elements of this pathway are located at MAMs [Yang et al., 2020].

1.3.4 MAMs and lipid biosynthesis

One of the first functions of MAMs to be discovered was their involvement in lipid biosynthesis [Vance, 1990]. One of the functions of the ER is the metabolism of lipids, for example, anabolism of membrane lipids, such as phosphatidylserine; phosphatidylserine is then shuttled to mitochondria through MAMs to be transformed into phosphatidylethanolamine [Vance, 1990, Xu and Huang, 2020]. Therefore, MAMs and the subsequent interplay between ER and mitochondria are essential for the metabolism of certain classes of lipids. This finding has been supported over the years by several proteomic studies that have in fact demonstrated that several proteins involved in lipid metabolism are enriched at MAMs [Xu and Huang, 2020].

1.3.5 MAMs and autophagy

An increasing body of evidence has linked MAMs to macroautophagy initiation as reviewed in [Yang et al., 2020]. Autophagy is the physiological process through which the cell degrades damaged organelles, proteins and other macromolecules.

There are two main types of autophagy, i.e. macroautophagy (herby referred to as autophagy) where the damaged elements are engulfed by autophagosomes and then delivered to lysosomes, and chaperone-mediated autophagy employs chaperones to deliver the damaged item directly to lysosomes.

It is thought that MAMs might be involved in the initiation process of autophagy. In fact, the autophagic protein ATG16 is localised in MAMs and this localisation is necessary for autophagy initiation [Hamasaki et al., 2013, Yang et al., 2020]. Besides, as described earlier in this Section, MAMs are involved in phospholipid synthesis and the protein LC3 – involved in autophagy – binds to phosphatidylethanolamine during phagosome formation.

1.3.6 MAMs and PD

PD is a complex disease, which displays a complex range of symptoms, a complex histopathological landscape and complex genetics. Even at the cellular level, it is characterised by dysfunctions affecting different parts and processes of the cell. These altered cellular processes include Ca^{2+} dyshomeostasis (see Section 7), ER stress [Colla, 2019], mitochondrial dynamics [Malpartida et al., 2021] and autophagy [Hou et al., 2020]. Interestingly, all of these processes are regulated by and involve MAMs and MAM proteins. This suggests that MAMs might be involved in the cytotoxic events leading to PD.

One of the main hallmarks of PD is the presence of α-synuclein aggregates. In addition, different variants of the *SNCA* gene cause PD or have been associated with PD. Although a link between α-synuclein in neurodegeneration has become established over the years, the exact pathogenic mechanism remains elusive.

Intriguingly, it has been demonstrated that α-synuclein shows a high affinity for lipid rafts and raft-like membranes like MAMs [Fortin, 2004]. Besides, over the

years, an increasing body of evidence has demonstrated that α-synuclein might localise to MAMs, using different orthogonal techniques [Guardia-Laguarta et al., 2013, Paillusson et al., 2017, Vicario et al., 2019].

It is possible that the interaction of α-synuclein with MAMs might be important for MAM physiology and the accumulation of pathological α-synuclein might disrupt MAM function. The first piece of evidence that α-synuclein might regulate MAMs came from Calì *et al.* who showed that overexpression of α-synuclein in cell lines could positively modulate ER-mitochondria Ca^{2+} release and increase the interaction between the two organelles [Calì et al., 2012].

Follow-up studies confirmed that α-synuclein can modulate MAM interaction and function, but mostly negatively. In fact, it was demonstrated that overexpression of α-synuclein could decrease MAM interaction, decrease ER-mitochondria Ca^{2+} release and decrease phospholipid synthesis [Guardia-Laguarta et al., 2013, Paillusson et al., 2017, Erustes et al., 2021]. In particular, Paillusson *et al.* demonstrated that α-synuclein interacts with the ERM/MAM protein VAPB and – when the levels of α-synuclein increase – it disrupts the interaction between VAPB and PTPIP51, both in cell lines overexpressing α-synuclein and iPSC-derived DAn harbouring the *SNCA*-Triplication (*SNCA*-Trp) mutation.

Recently, it has been demonstrated that α-synuclein may modulate MAMs distance in a dose-response manner, and low levels of overexpression may increase the interaction while higher levels may decrease the interaction. This finding may explain the different results observed by different groups and may suggest that low and physiological levels of α-synuclein might positively regulate the formation of MAMs, while high, toxic levels that might boost oligomerisation of α-synuclein may cause a loss of this function [Calì et al., 2019]. Nonetheless, some toxic α-synuclein species have been found to be localised to MAMs [Grassi et al., 2018].

In conclusion, this evidence suggests that α-synuclein itself might be the source

of the vulnerability of MAMs, which might prove to be a potential pathogenic mechanism at the base of PD.

Intriguingly, MAMs-resident Sig1R receptor has been extensively studied as a potential therapeutic target for PD [Francardo, 2014] and a phase 2 clinical trial to evaluate the efficacy of blarcamesine – a Sig1R agonist – on PD progression has just concluded (ClinicalTrials.gov Identifier: NCT04575259).

In conclusion, MAMs appear to be highly dysfunctional in PD and might be a very interesting therapeutic target for the disease.

1.4 iPSC-derived neuronal models of PD [1]

PD has very complex pathophysiology and there are no disease-modifying drugs to treat the disease. Therefore, accelerating the process of drug discovery requires accurate disease models. The most common disease models are divided into *in vitro* models including cell lines and primary cultures and *in vivo* models including worms, flies, fish, rodent models, and non-human primates. *In vitro* models are easily tractable, which makes them the most suitable for the earliest phases of drug discovery as they allow large-scale phenotypic screening of large libraries. However, cell lines are usually immortalised cells with aberrant cell biology. Additionally, primary cultures, derived from animal models, may not completely share the same biology as humans.

In addition, in recent years, a consensus has been building around the idea that stopping cell toxicity mechanisms and preventing neurons from degenerating might be the way forward to develop disease-modifying drugs to treat neurodegenerative diseases. Therefore, there has been an increasing interest in trying to understand and target pathological events occurring early in the disease timeline in order to stop DAns from degenerating. However, this requires that researchers employ the use of laboratory models that recapitulate these early pathogenic events.

In recent years, the advent of induced pluripotent stem cell (iPSC) reprogramming and differentiation technologies have made it possible to obtain *in vitro* cultures of virtually any human cell type, including DAns from PD patients. iPSCs offer the possibility to study human DAns from PD patients in order to shed some light on the early disease mechanisms responsible for neurodegeneration.

[1] Part of the content of this section is adapted from [Caiazza et al., 2020]

1.4.1 The advent of cell reprogramming into iPSCs

The advent of iPSC technology by the Yamanaka group revolutionised the field of human *in vitro* disease modelling. Pluripotent stem cells can be artificially derived from adult somatic cells by inducing the expression of the Yamanaka factors: Oct3/4, Sox2, Klf4, c-Myc [Takahashi and Yamanaka, 2006]. Oct3/4 and Sox2 are required for pluripotency, whereas, c-Myc and Klf4 increase the efficiency of iPSC production by interfering with apoptosis and senescence.

Originally, reprogramming was achieved by employing integrating viruses such as lentiviruses and retroviruses to induce the expression of the Yamanaka factors [Takahashi and Yamanaka, 2006, Takahashi et al., 2007]. However, the random integration of these genes of interest and their promoters carries a risk of inducing insertional mutagenesis in the host genome. Therefore a non-integrating approach is now favoured, through the use of non-integrating viruses such as Sendai and adenovirus [Stadtfeld et al., 2008, Fusaki et al., 2009, Zhou and Freed, 2009], episomal plasmids [Okita et al., 2008], proteins [Kim et al., 2009] or small molecules [Hou et al., 2013]. However, non-integrating approaches may display a lower reprogramming efficiency, therefore excisable integrating vectors have also been developed; these systems harness the efficacy of integrating vectors but also offer the possibility of being removed from the genome at any moment, through the use of lentiviral or retroviral vectors with a floxed integration region [Chang et al., 2009] or piggyBac transposons [Kaji et al., 2009].

1.4.2 Differentiation into DAns

The earliest, and still popular, technique for the generation of DAns from iPSCs goes through the generation of embryoid bodies (EBs). EBs are 3D colonies of pluripotent stem cells which undergo spontaneous differentiation towards the three

germ layers (endoderm, mesoderm and ectoderm) recapitulating the early phases of *in vivo* development. Neurons derive from the ectoderm and in order to enrich for neuroectodermal cells, it is possible to plate embryoid bodies in an adherent culture so that the culture starts forming neural tube-like rosettes which can be isolated. These neuronal precursors express the neuroectoderm marker PAX6. A pivotal study demonstrated that exposure of these $PAX6^+$ cells to FGF8 and SHH could produce midbrain DAns [Yan et al., 2005]. In particular, early exposure to FGF8 was necessary to pattern the precursors towards a more posterior fate (caudalisation) and subsequent exposure to FGF8 and SHH allowed differentiation into midbrain DAns [Yan et al., 2005]. This protocol generated a rather mixed population of electrophysiologically active cells of which 32% were positive for TH.

In the following years, there has been an increasing interest in improving the regionalisation of iPSC-derived DAns. Recent neurodevelopmental studies demonstrated that SNc DAns derive from the midbrain floor plate rather than $PAX6^+$ precursors [Ono et al., 2007]. Therefore, a number of studies aimed at deriving DAns through the *in vitro* generation of midbrain floor plate precursors. Neural differentiation is a default program, but efficiency can be increased by blocking mesoderm and endoderm conversions. In 2009, the Studer laboratory developed the dual inhibition of SMAD signalling to reliably induce neural differentiation. The system employs Noggin (or the agonist dorsomorphin or LDN193189) to block BMP signalling and SB431542 to block Activin and Nodal signalling [Chambers et al., 2009]. The neural precursor cells generated by means of the dual SMAD inhibition default to an anterior neural fate.

However, midbrain neurons derive from the floor plate and, therefore, in 2011 the Studer laboratory slightly modified this protocol to pattern the precursors towards a more posterior and lower fate (caudalisation and ventralisation) therefore inducing midbrain floor-plate progenitors (mFPPs) in the first phases of the dif-

ferentiation [Kriks et al., 2011]. Ventralisation is obtained by activating the Sonic hedgehog signalling pathway using recombinant SHH and puromorphamine. Caudalisation and final patterning of dopaminergic neural progenitors require FGF8a and Wnt signalling activation (achieved with CHIR99021, a potent inhibitor of GSK3B able to activate Wnt signalling). The resultant dopaminergic neural progenitors express the midbrain dopaminergic neural progenitor markers FOXA2 and LMX1A. Furthermore, neuronal differentiation and maturation are achieved using DAPT to inhibit Notch signalling and push towards neuronal differentiation, db-cAMP to stimulate neurite elongation, survival and further maturation, and a cocktail of neurotrophic factors (BDNF, GDNF, ascorbic acid and TGFβ3) for trophic support [Kriks et al., 2011]. The resultant neuronal culture was reported to yield 75% of TH^+ neurons with a ventral midbrain identity (where the SNc is located) from embryonic stem cells. The cells are electrophysiologically active and were successfully transplanted in a murine model of PD [Kriks et al., 2011]. This protocol has been adapted for iPSCs as well, however lower efficiency was reported [Beevers et al., 2017].

More recently it was demonstrated that it is possible to pause the differentiation protocol and expand the pool of mFPPs [Fedele et al., 2017]. This extra step in the differentiation protocol demonstrated to increase the differentiation efficiency of iPSCs into DAns. The expansion of the mFPPs also brought the added benefit of increasing the total number of cells obtained per differentiation and the generation of a pool of precursors able to maintain their differentiating potential upon cryostorage [Fedele et al., 2017].

1.4.3 iPSC-derived DAns for disease modelling

One of the major advantages of iPSC-derived neurons is that they enable researchers to study phenotypes in neurons derived directly from patients with different ge-

netic backgrounds to highlight the shared pathogenic mechanisms in PD. Table 1.3 summarises some of the recent cellular phenotypes discovered in iPSC-derived neurons from different genetic backgrounds.

Table 1.3: Non-comprehensive list of cellular phenotypes discovered in iPSC-derived neurons from different genetic backgrounds

Gene	Phenotype	Reference
GBA	Altered calcium function, altered calcium content	[Schöndorf et al., 2014]
GBA	ER stress increase, UPR increase, lysosomal impairment	[Fernandes et al., 2016]
GBA	ER stress increase, UPR increase, lysosomal impairment, increased α-synuclein levels, alteration in mitochondrial structure, altered mitochondrial respiration, decreased mitochondrial dynamics	[Schöndorf et al., 2018]
GBA	ER stress increase, UPR increase	[Lang et al., 2019]
LRRK2	Altered mitochondrial respiration, decreased mitochondrial motility	[Cooper et al., 2012]
LRRK2	Altered mitophagy	[Hsieh et al., 2016]
LRRK2	Altered endocytosis	[Connor-Robson et al., 2019]
LRRK2	Altered calcium content	[Korecka et al., 2019]
LRRK2	Increased sensitivity to oxidative insults	[Nguyen et al., 2011]
PINK1	Altered mitochondrial respiration	[Cooper et al., 2012]
PINK1	Altered mitochondrial structure, increased ROS levels	[Chung et al., 2013]
PRKN	Altered mitochondrial structure, increased ROS levels	[Chung et al., 2013]
PRKN	Altered mitophagy	[Suzuki et al., 2017]
SNCA	Increased ROS levels	[Byers et al., 2011]
SNCA	Altered mitochondrial respiration, defective mitochondrial biogenesis, increased ROS levels	[Ryan et al., 2013]
SNCA	Lysosomal impairment, altered protein trafficking	[Mazzulli et al., 2016]
SNCA	Altered mitophagy	[Shaltouki et al., 2018]
SNCA	ER stress increase, UPR increase, altered mitochondrial structure, altered mitochondrial respiration, decreased mitochondrial dynamics, defective mitochondrial biogenesis, increased ROS levels	[Zambon et al., 2019]

Through these studies, it is possible to highlight cellular phenotypes that one may aim to correct in phenotypic screenings. It is also possible to reconstruct disease mechanisms with the ultimate goal of discovering new druggable targets (Figure 1.3).

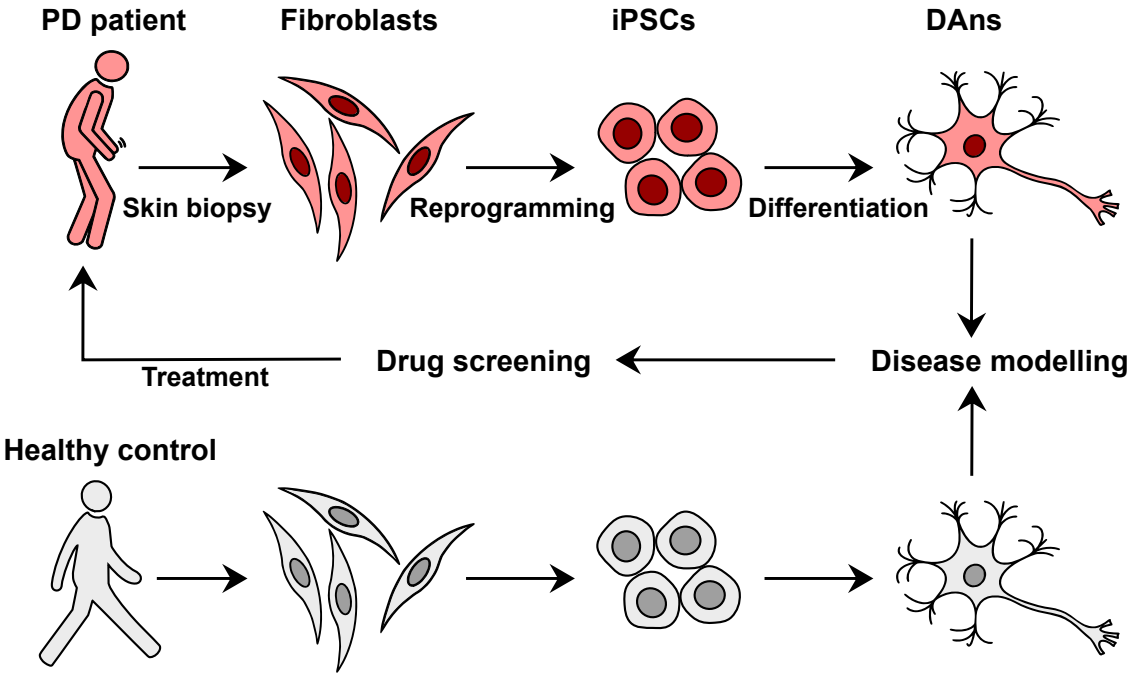


Figure 1.3: Applications for iPSC-derived neurons in PD

iPSCs are derived from patient somatic cells (typically fibroblasts) by the expression of the Yamanaka factors (Oct3/4, Sox2, Klf4, c-Myc), and then they are differentiated into DAns or other disease-relevant cells. iPSCs can be employed to study phenotypes and discover pathogenic mechanisms relevant to PD. This study can be pursued with classic cellular and molecular assays or by novel, unbiased, high-throughput techniques such as transcriptomic or proteomic profiling. High-throughput preclinical drug screenings can be performed on relevant patient cells in order to discover potential therapeutic agents able to reverse the disease phenotypes. Additionally, unveiling new disease mechanisms can lead to the identification of new druggable targets.

1.4.4 i^3 neurons for disease modelling

iPSC-derived DAns offer a great platform to investigate cell-autonomous mechanisms leading to cell toxicity and degeneration of these cells. However, most of the differentiation protocols to generate DAns – or other neurons – using small mo-

lecules only are long and can be hard to scale up. For these reasons, Wang and colleagues have developed a tool to differentiate a homogeneous culture of neurons positive for cortical markers in a 2-step protocol. This tool employs a human iPSC line that underwent a knock-in of a copy of the mouse neurogenin 2 (*Ngn2*) gene regulated by a doxycycline-inducible promoter in the AAVS1 locus [Wang et al., 2017]. The AAVS1 locus is a safe-harbour locus for neurons, meaning that it is not silenced in neurons. This integrated, inducible, and isogenic tool was called i^3 neurons.

The differentiation protocol consists of the induction of the neuronal fate by the induction of the (*Ngn2*) gene and then a maturation phase [Fernandopulle et al., 2018].

These cells provide a very tractable tool to perform chemical [Wang et al., 2017] or genetic screenings to reproduce disease phenotypes or correct them. In particular, this tool has been used in synergy with CRISPR interference for genetic screenings [Tian et al., 2019, Tian et al., 2021].

1.4.5 Pitfalls of iPSC-based models

The advent of iPSC technology has completely revolutionised translational research. Traditional *in vitro* models rely on cell lines, primary cultures from animal models or primary cultures from patients. Cell lines are immortalised and as a result often carry aberrant chromosomes, whereas primary cultures from animal models have the caveat of being from another species. Primary cultures of relevant cell types from patients can be very difficult to handle and for neurodegenerative diseases, almost impossible to obtain. iPSC-derived DAns, therefore, offer the opportunity to culture in a dish the very same neurons that degenerate in the brains of PD patients. However, this technology also has some drawbacks.

It has been demonstrated that iPSCs show a high level of variability reflecting

the genetic differences among donors [Rouhani et al., 2014]. On the one hand, the variability due to different genetic backgrounds makes iPSC-based cell models highly physiological and may help highlight the shared pathogenic mechanisms in PD; on the other hand, this phenotypic noise may mask some specific phenotypes in these cells. This raises the problem of which is the best control for iPSC-derived cellular models. It is possible to employ cells derived from control subjects; however, it may be necessary to include a high number of patient and control lines per experiment in order to separate the control and the disease state. This solution can be extremely expensive and, in some cases, impossible to pursue. In the case of a known mutation, it is also possible to employ genome editing and generate isogenic controls. This way, variance is minimised and it is easier to identify phenotypes that can be definitely attributed to the mutation. However, for low penetrance mutations, the role of the rest of the genetic background may be highly relevant and therefore isogenic controls may be insufficient or even misleading.

Another concern is cell maturity and age. During the process of reprogramming, cells rejuvenate and signs of cellular ageing such as inactivation of telomerase expression, are erased [Marión and Blasco, 2010]. Therefore, the differentiation process starts with immature neurons, goes onto young neurons, then mature neurons and possibly old neurons. However, neuronal maturation is a slow process and transplantation experiments have shown that there is something like an autonomous clock that seems to be species-dependent [Isacson and Deacon, 1997]. This might also be true *in vitro*, therefore making it difficult to obtain fully mature neurons derived from human iPSCs. This issue is not present in iPSC-derived DAns which may be purified using the intracellular marker TH and shown to possess a transcriptomic profile indistinguishable from that of mature post-mortem DAns [Sandor et al., 2017]. Another pitfall to consider is that most small molecule-based protocols generate mixed neuronal cultures with different percentages of TH+ cells. There-

fore, it is possible that observations made in these cultures may be influenced by TH- cells. Utilising iPSC-derived neurons to model PD generates added challenges as PD is an age-related disease. It is common to observe cellular phenotypes such as DNA damage and mtDNA damage, iron accumulation and neuromelanin accumulation in aged cells, which may be quite challenging to reproduce *in vitro*.

However, this model is still one of the most relevant available in the context of human disease modelling and can highlight the cellular defects that are responsible for vulnerability in the progression of PD, and put into evidence pathways of molecular dysfunction occurring early in the disease process which could potentially lead us to the development of treatments to use before the later onset of disease.

1.5 Aims of the thesis

In this thesis we will:

- Chapter 3: Use Ca^{2+} imaging to study intracellular Ca^{2+} dynamics in iPSC-derived DAn from PD patients
- Chapter 4: Use CRISPRi technology to study the role of candidate genes in ER and mitochondrial Ca^{2+} handling in iPSC-derived i^3 neurons
- Chapter 5: Optimise APEX2-based spatial proteomics to study ER and mitochondrial membrane proteins
- Chapter 6: Evaluate FASN as a novel target for PD

Chapter 2

Materials and Methods

2.1 Cell Culture

2.1.1 Human iPSCs culture, expansion and cryopreservation

2.1.1.1 Thawing iPSC

Day 0 One well of a 6-well plate per line is coated with 1 ml Matrigel or Geltrex (Table 2.10) O/N at 37°C.

Day 1 2 ml per well of mTeSR medium supplemented with ROCK inhibitor (Y-27632) 10 μM (Table 2.10) are prepared and filtered through a 0.22 μm filter. The medium is warmed up to RT. One conical tube per line with 6 ml of Knockout DMEM (Table 2.10) medium is prepared and warmed up to room temperature (RT). Cells are transported from the liquid nitrogen storage tank to tissue culture in dry ice and thawed within half an hour. The cryovials are defrosted in the water bath at 37°C until only a small piece of ice is left. The cryovial is dried and sprayed with ethanol. The contents of the vial are removed into the conical designed for that line and centrifuged at 350 relative centrifugal force (RCF) for 5 min using a Hettich centrifuge and equipped with the 5624 rotor. While the cells are centrifuging, the

Matrigel/Geltrex on the plate is aspirated and replaced with 1 ml of mTeSR with ROCK inhibitor (Y-27632) 10 μM. At the end of the centrifugation, the supernatant is then aspirated and resuspended into 1 ml of mTeSR, which is removed into the well with medium.

Day 2 The cells are observed and fed by replacing 100% of the medium with mTeSR.

Cells are fed until over 80% confluent when they can be passaged.

2.1.1.2 Colony passaging of iPSCs to generate a masterstock

Colony passaging is a gentle non-enzymatic passaging method that uses 0.5 mM EDTA in phosphate-buffered saline (PBS) to detach the cells from the plate in clumps. This gentle method is recommended when cells are propagated to generate a masterstock.

Day 0 One 10 cm dish per line is coated with 4 ml Matrigel or Geltrex (Table 2.10) overnight (O/N) at 37°C.

Day 1 10 ml per well of mTeSR medium supplemented with ROCK inhibitor (Y-27632) 10 μM are prepared and filtered through a 0.22 μm filter. The medium is warmed up to RT. The Matrigel/Geltrex on the plate is aspirated and replaced with 9 ml of mTeSR with ROCK inhibitor (Y-27632) 10 μM. Cells are washed with 1 ml of EDTA and then EDTA is incubated at 37°C for 2 min and then checked. After that, the plate is checked every minute until the cells start becoming round but before they are completely detached from the plate. Then EDTA is gently aspirated and the cells are washed off the plate with 1 ml of mTeSR medium with ROCK inhibitor (Y-27632) 10 μM using a P1000 pipette. The cell suspension is triturated a maximum of 4-5 times in order to keep the colonies intact. The cells are then removed into the plate with medium.

Day 2 The cells are observed and fed by replacing 100% of the medium with

mTeSR.

Cells are fed until over 80% confluent when they can be frozen down or passaged again.

2.1.1.3 Single-cell passaging of iPSCs

For shorter expansion for immediate use (up to 15 days), cells are passaged as single cells using Accutase (Table 2.10). Single-cell passaging obtains more spread-out cultures and is required when starting a new differentiation. When single cell passaged, 95-100% confluent cells are split in a 1:3 (controls) or 1:2 (patients) ratio.

Day 0 The required number of wells of a 6-well plate are coated with 1 ml Matrigel or Geltrex (Table 2.10) O/N at 37°C.

Day 1 2 ml per well of mTeSR medium supplemented with ROCK inhibitor (Y-27632) 10 μM are prepared and filtered through a 0.22 μm filter. The medium is warmed up to RT. One conical tube per line with 6 ml of Knockout DMEM medium is prepared and warmed up to 37°C. 0.5 ml of Accutase per well are warmed up to RT. Cells are washed with 1 ml PBS and then 0.5 ml of Accutase are incubated at 37°C for 3 min. The contents of the wells are triturated gently to obtain a single cell suspension and then removed into the conical designed for that line and centrifuged at 350 RCF for 5 min using a Hettich centrifuge and equipped with the 5624 rotor. While the cells are centrifuging, the Matrigel/Geltrex on the plate is aspirated and replaced with 1.5 ml of mTeSR with ROCK inhibitor (Y-27632) 10 μM. At the end of the centrifugation, the supernatant is then aspirated and resuspended into 1 ml of mTeSR, which is equally split into the destination wells.

Day 2 The cells are observed and fed by replacing 100% of the medium with mTeSR.

Cells are fed until over 95-100% confluent when they can be passaged again.

Table 2.1: Composition of the iPSC freezing medium

Composition	Concentration
Embryonic stem-cell FBS 2.10	90%
DMSO	10%

2.1.1.4 Cryopreservation of iPSCs

For cryostorage, iPSCs are dissociated as single cells with Accutase as described in 2.1.1.3. Before spinning down, 20 µl of the cell suspension in the spinning falcon are saved and used to count the cells using Solution 18 (Table 2.10) as dead/live staining in NC-Slide A8 chamber-slides using the Chemometec NucleoCounter NC-250. After the spinning, the pellet is resuspended to a final concentration of 4E6 cells/ml in cold freezing medium (Table 2.1) per well. The cell suspension is aliquoted into labelled cryovials (1 ml per cryovial). The cryovials are arranged in cold cryovial freezing containers and moved to a -80°C freezer. After 24 hours (h) the cryovials are moved to their final destination in the liquid nitrogen tank.

2.1.2 Establishment of polyclonal human iPSC lines

In order to create iPSC lines expressing transgenes of interest, iPSC lines were nucleofected to deliver the constructs of interest and a selection marker in a PiggyBac transposon and a construct for transposase expression. This way it is possible to have a stable integration of the transgene in a random location in the genome and use the selection to enrich the culture with cells expressing the constructs.

2.1.2.1 Nucleofection of iPSCs with PiggyBac constructs

Before nucleofection, the cells are incubated for 1 h in mTeSR medium supplemented with ROCK inhibitor (Y-27632) 10 µM. The cells are dissociated as single cells with Accutase as described in 2.1.1.3. Before spinning down, 20 µl of the

cell suspension in the spinning falcon are saved and used to count the cells using Solution 18 (Table 2.10) as dead/live staining in NC-Slide A8 chamber-slides using the Chemometec NucleoCounter NC-250. After the spinning, the pellet is resuspended to a final concentration of 30E6 cells/ml in mTeSR medium supplemented with ROCK inhibitor (Y-27632) 10 μM. 10 μl of cells are mixed with 200 ng of transposase plasmid, 400 ng of the construct of interest and 2 μl of buffer R (see Table 2.10). The nucleofection is carried out in a Neon Transfection System using 10 μl tips (see Table 2.10). The settings used for the nucleofection are 'HiTrans' 1400 V, 20 ms width, 1 pulse.

The 10 μl of transfected cells are plated on a Matrigel-coated 24 well in 250 μl of mTeSR supplemented with 1% of Revitacell (see Table 2.10). After 1 h 250 μl of mTeSR supplemented with 1% of Revitacell are added to the attached cells.

2.1.2.2 Selection of transgene-expressing cells

To enrich the cell population with transgene-expressing cells, the cells are selected using the following selection markers:

- Hygromycin for cells transfected with K23-PB-CAG-dCas9-KRAB
- Puromycin for cells transfected with PB-TO-APEX-NES, PB-TO-ERM-APEX, PB-TO-APEX-OMM.

The selection is started on cells 80% confluent and is carried out in 4 bursts of 2 days each. The concentrations of antibiotics used in each burst are summarised in Table 2.2. Every time that a new round of selection is performed, an untreated well is kept and then frozen down as a backup. At the final round of selection, the percentage of transfected cells is assessed and if above 85% the cells can be expanded using colony passaging and cryostored as described in 2.1.1.2 and 2.1.1.4.

Table 2.2: Antibiotic selection of transfected iPSCs

Antibiotic	Concentration (1-2)	Concentration (3-4)
Hygromycin	125 μg/ml	250 μg/ml
Puromycin	1 μg/ml	2 μg/ml

2.1.3 DAns differentiation and mFPP cryopreservation

2.1.3.1 Differentiation of DAns

DAns were differentiated as previously described [Fedele et al., 2017], with slight modifications.

Day -2 iPSCs are passaged as single cells as described in 2.1.1.3. The cells are passaged following a 1:1.5 ratio.

Day -1 The cells are observed and fed by replacing 100% of the medium with mTeSR.

From day 0 on, a single 6-well well is kept in 4 ml of medium (see Table 2.3 for media compositions). On days 0, 1, 3, 5, 7, 9, 11, 13, 15, 17, 19 and exp 2, 4, 6, 8, 10, 12, 14, 16, 19 cells are fed by replacing 100% of the medium with the corresponding medium (see Table 2.3), while, the rest of the days, the cells are fed by replacing only 50% of the medium with the corresponding medium. Media are prepared fresh and filtered every day through a 0.22 μm filter. For details on the materials listed in Table 2.3 refer to Table 2.10.

Table 2.3: DAns differentiation protocol media

	Medium composition	Concentration
Day 0	KO DMEM KSR (Section 2.4)	100%
	LDN-193189	100 nM
	SB-431542	10 μM
Day 1-2	KO DMEM KSR	100%
	LDN-193189	100 nM
	SB-431542	10 μM
	Recombinant sonic hedgehog C24II (SHH C24II)	100 ng/ml
	Purmorphamine	2 μM

	Fibroblast growth factor 8a (FGF8a)	100 ng/ml
Day 3-4	KO DMEM KSR	100%
	LDN-193189	100 nM
	SB-431542	10uM
	SHH C24II	100 ng/ml
	Purmorphamine	2 μM
	FGF8a	100 ng/ml
	CHIR-99021	3 μM
Day 5-6	KO DMEM KSR	75%
	NNB (Section 2.4)	25%
	LDN-193189	100 nM
	SHH C24II	100 ng/ml
	Purmorphamine	2 μM
	FGF8a	100 ng/ml
	CHIR-99021	3 μM
Day 7-8	KO DMEM KSR	50%
	NNB	50%
	LDN-193189	100 nM
	CHIR-99021	3 μM
Day 9-10	KO DMEM KSR	25%
	NNB	75%
	LDN-193189	100 nM
	CHIR-99021	3 μM
Exp 1, 7, 13, 18	KO DMEM KSR	25%
	NNB	75%
	CHIR-99021	3 μM
	ROCK inhibitor (Y-27632)	10 μM
Exp 2-6, 8-12, 14-17, 19	KO DMEM KSR	25%
	NNB	75%
	LDN-193189	100 nM
	CHIR-99021	3 μM
Day 11-12	NB (Section 2.4)	100%
	Brain-derived neurotrophic factor (BDNF)	20 ng/ml
	Glial-derived neurotrophic factor (GDNF)	20 ng/ml
	Transforming growth factor β3 (TGFβ3)	1 ng/ml
	DAPT	10 μM
	Ascorbic acid	200 μM
	Dibutyryl cAMP (db-cAMP)	500 μM

	CHIR-99021	3 μM
Day 13-19	NB	100%
	BDNF	20 ng/ml
	GDNF	20 ng/ml
	TGFβ3	1 ng/ml
	DAPT	10 μM
	Ascorbic acid	200 μM
	db-cAMP	500 μM
Day 20 (re-plating)	NB	100%
	BDNF	20 ng/ml
	GDNF	20 ng/ml
	TGFβ3	1 ng/ml
	DAPT	10 μM
	Ascorbic acid	200 μM
	db-cAMP	500 μM
	ROCK inhibitor (Y-27632)	10 μM
Day 22-harvest	NB	100%
	BDNF	20 ng/ml
	GDNF	20 ng/ml
	TGFβ3	1 ng/ml
	DAPT	10 μM
	Ascorbic acid	200 μM
	db-cAMP	500 μM
	Antibiotic-antimycotic	1%

On exp 1, 7, 13, 18 the mFPPs are passaged as single cells using Accutase (Table 2.10) in a 1:2 ratio (the process is similar to that described in 2.1.1.3 with slight modifications). The needed number of wells of a 6-well plate are coated with 1 ml Matrigel or Geltrex (Table 2.10) O/N at 37°C. The exp 1, 7, 13, 18 medium is prepared, filtered through a 0.22 μm filter and warmed up to 37°C. One (two if more than 4 wells/line are being dissociated) conical tube per line with 6 ml of Knockout DMEM medium is prepared and warmed up to 37°C. 0.5 ml of Accutase per well are warmed up to RT. Cells are washed with 1 ml PBS and then 0.5 ml of Accutase are incubated at 37°C for 5-7 min. The contents of the wells are triturated gently to

obtain a single cell suspension and then removed into the conical designed for that line and centrifuged at 350 RCF for 5 min using a Hettich centrifuge and equipped with the 5624 rotor. While the cells are centrifuging, the Geltrex on the plate is aspirated and replaced with 3.5 ml of medium. At the end of the centrifugation, the supernatant is then aspirated and resuspended into 1 ml of medium for each dissociated well, and then 500 μl of the cell suspension are plated in the destination wells.

On day 20 the cells are replated into their final assay layout. On day 18 the plates are coated with poly-L-ornithine 0.01% (Table 2.10) O/N at 37°C, the coating is then aspirated and replaced with biolaminin 10 μg/ml (Table 2.10), which is incubated O/N at 37°C. The coating is then aspirated and replaced with day 20 medium. The volumes of coating used are summarised in Table 2.5.

The maturing neurons are dissociated with Accutase as described in 2.1.1.3. One (two if more than 4 wells/line are being dissociated) conical tube per line with 6 ml of Neurobasal medium is prepared and warmed up to 37°C. 0.5 ml of Accutase per well are warmed up to RT. Cells are washed with 1 ml PBS and then 0.5 ml of Accutase are incubated at 37°C for 5-7 min. The contents of the wells are triturated gently to obtain a single cell suspension and then removed into the conical designed for that line and centrifuged at 350 RCF for 5 min using a Hettich centrifuge and equipped with the 5624 rotor. The cells are resuspended into 2 ml of day 20 medium and counted using Solution 18 (Table 2.10) as dead/live staining in NC-Slide A8 chamber-slides using the Chemometec NucleoCounter NC-250. The cells are then diluted to 1.7E6 cells/ml and plated down in the final plate layout. The amounts of cells per well plated are summarised in Table 2.6.

On day 22 the cells are treated with mitomycin C 2.10 to induce apoptosis of proliferating cells in culture to enrich for postmitotic neurons. On the day NB supplemented with 1μg/ml mitomycin C is prepared. 100% of the medium on the

Table 2.4: Basal media composition

	Medium composition	Concentration
KO DMEM KSR	Knockout DMEM	82% (v/v)
	KnockOut Serum Replacement	15% (v/v)
	2-mercaptoethanol	1% (v/v)
	L-Glutamine	1% (v/v)
	MEM non-essential amino acids (NEAA)	1% (v/v)
NNB	Neurobasal Medium	97.5% (v/v)
	N2 Supplement	0.5% (v/v)
	B-27 Supplement w/o Vit A	1% (v/v)
	L-Glutamine	1% (v/v)
NB	Neurobasal Medium	97% (v/v)
	B-27 Supplement w/o Vit A	2% (v/v)
	L-Glutamine	1% (v/v)

Table 2.5: Coating volumes

Plate format	Coating volume (µl)
384 well	15
96 well half area	25
96 well	50
12 well	500
6 well	1000

cells is replaced with the mitomycin C solution and incubated for 1 h at 37°C. 100% of the mitomycin C is then replaced with day 22+ medium.

From day 24 on, 50% of the medium is replaced with fresh day 22+ medium on Mondays, Wednesdays and Fridays.

The feeding and mitomycin C treatment volumes are listed in Table 2.7

2.1.3.2 Viral transduction of dopaminergic neurons

DAns are transduced after replating on day 20. For GCEPIA*er* and RGECO*mt*, the viruses produced as described in 2.2 are thawed on ice, mixed in a 1:1 ratio and then spiked on the cells using an E1-ClipTip Electronic Adjustable Tip Spacing Multichannel Equalizer Pipette. In particular, 6 µl of the mixture containing both

Table 2.6: Amount of DAns plated per well

Plate format	Cell #/well	Plating volume	Purpose
384 well	20E3	12 µl	Imaging
	25E3	15 µl	Calcium imaging
96 well half area	27E3	16 µl	Imaging
	35E3	21 µl	Calcium imaging
96 well	60E3	35 µl	Imaging
	85E3	50 µl	Calcium imaging
12 well	1.7E6	1 ml	Protein and/or RNA extraction
6 well	4E6	2.5 ml	Protein extraction

Table 2.7: Feeding and mitomycin C volumes

Plate format	Mitomycin C volume	Full feed volume	Half feed volume
384 well	15 µl	30 µl	15 µl
96 well half area	25 µl	50 µl	25 µl
96 well	50 µl	100 µl	50 µl
12 well	500 µl	1 ml	500 µl
6 well	1 ml	2 ml	1 ml

viruses are spiked in each 96 well half area with 35E3 cells per well, or 14 µl in each 96 well with 85E3 cells per well. The virus is incubated for 48 h until the cells are treated with mitomycin C.

2.1.3.3 Cryopreservation of mFPP

On day exp 18, part of the cells are brought forward to the last stage of differentiation and maturation, and the rest can be cryostored. For cryostorage, the cells are dissociated as single cells with Accutase. One (two if more than 4 wells/line are being dissociated) conical tube per line with 6 ml of Knockout DMEM medium is prepared and warmed up to 37°C. 0.5 ml of Accutase per well are warmed up to RT. Cells are washed with 1 ml PBS and then 0.5 ml of Accutase are incubated at 37°C for 5-7 min. The contents of the wells are triturated gently to obtain a single cell suspension and then removed into the conical designed for that line and centrifuged at 350 RCF for 5 min using a Hettich centrifuge and equipped with the 5624

Table 2.8: Composition of the mFPP freezing medium

Composition	Concentration
KO DMEM KSR	22.5%
NNB	67.5%
DMSO	10%

rotor. The pellet is then resuspended in 1 ml of cold freezing medium (Table 2.8) per well. The cell suspension is aliquoted into labelled cryovials (1 ml per cryovial). The cryovials are arranged in cold cryovial freezing containers and moved to a -80°C freezer. After 24 h the cryovials are moved to their final destination in the liquid nitrogen tank.

2.1.4 List of lines used

Table 2.9: List of lines used

Donor ID	Clone	Genotype	Age / Sex	Reprogramming	Reference
SFC840	03-06	Control	67 / F	Sendai virus	[Lang et al., 2019]
JR053	01	Control	68 / M	Retrovirus	[Lang et al., 2019]
SFC156	03-01	Control	75 / M	Sendai virus	[Lang et al., 2019]
SFC067	03-01	Control	72 / M	Sendai virus	[Lang et al., 2019]
SFC065	03-03	Control	65 / M	Sendai virus	[Lang et al., 2019]
SFC872	03-03	*GBA-L444P*	68 / M	Sendai virus	
SFC866	03-02	*GBA-L444P*	61 / M	Sendai virus	
NH031	02	*GBA-L444P*	50 / F	Sendai virus	
JR065	01	*GBA-L444P*	46 / F	Sendai virus	
MK071	03	*GBA-N370S*	81 / F	Retrovirus	[Lang et al., 2019]
MK082	26	*GBA-N370S*	51 / M	Retrovirus	[Lang et al., 2019]
MK088	01	*GBA-N370S*	46 / M	Retrovirus	[Lang et al., 2019]
SFC871	03-09	*GBA-N370S*	70 / F	Sendai virus	[Lang et al., 2019]
SFC828	03-06	*SNCA-A53T*	51 / F	Cytotune 1	[Zambon et al., 2019]
SFC829	03-06	*SNCA-A53T*	46 / M	Cytotune 1	[Zambon et al., 2019]
SFC830	04-09	*SNCA-A53T*	51 / M	Cytotune 1	[Zambon et al., 2019]
SFC831	03-01	*SNCA-Trp*	55 / F	Cytotune 1	[Zambon et al., 2019]
SFC831	03-03	*SNCA-Trp*	55 / F	Cytotune 1	[Zambon et al., 2019]
SFC831	03-05	*SNCA-Trp*	55 / F	Cytotune 1	[Zambon et al., 2019]

2.1.5 Differentiation of i^3 neurons

The differentiation of i^3 neurons was performed as previously described in [Fernandopulle et al., 2018].

2.1.6 Materials

Table 2.10: List of reagents used for cell culture

Product name	Brand	Catalogue number
2-mercaptoethanol	Gibco	21985023
Antibiotic-antimycotic	Gibco	15240096
Ascorbic acid	Sigma-Aldrich	A4544-25G
B-27 Supplement w/o Vit A	Gibco	12587010
BDNF	Peprotech	450-02
CHIR99021	Tocris	4423/10
DAPT	Abcam	ab120633-50mg
db-cAMP	Sigma-Aldrich	D0627-5X1G
DMEM, high glucose, GlutaMAX Supplement	Gibco	61965059
Fetal Bovine Serum	SAFC	F7524-500ML
FGF8a	SinoBiological	16124-HNAE-SIB-200ug
GDNF	Peprotech	450-10
Geltrex	Gibco	A1413302
hESC-qualified Matrigel	Corning	354277
Knockout DMEM	Gibco	10829018
KnockOut Serum Replacement	Gibco	10828010
L-Glutamine	Thermo Scientific	25030024
LDN193189	Sigma-Aldrich	SML0559-5MG
Lipofectamine 3000 Transfection Reagent	Invitrogen	L3000015
MEM NEAA	Gibco	11140050
MitomycinC	Abcam	ab120797-2mg
mTeSR1 Complete Medium Kit (single pack)	STEMCELL Technologies	85850
N2 Supplement	Gibco	17502048
Neurobasal Medium	Gibco	21103049
Optimem Reduced Serum Media	Gibco	31985070
Penicillin-Streptomycin	Gibco	15140122
Purmorphamine	Tocris	4551/10

ROCK inhibitor (Y27632)	Apex Bio	A3008-APE-10mg
SB431542	Apex Bio	A8249-APE-10mg
Sonic Hedgehog C24II high activity	R&D Systems	1845-SH-500
StemPro Accutase	Gibco	A1110501
TGFβ3	Peprotech	100-36E
Trypsin-EDTA (0.25%), phenol red	Gibco	25200056

2.2 Lentivirus packaging

On day 1, HEK293T cells were seeded at 5E5 cell/cm2 in 150mm plates.

On day 2, cells were transfected with the 3 packaging vectors and the vector of interest using Lipofectamine 3000 according to manufacturer's instructions.

On day 3, cells underwent a full media change with 1X Viralboost (Alstem).

On day 6, media was collected and filtered with 0.45 uM filters. Virus was concentrated using Lenti-X Concentrator (Takara Bio), according to manufacturer's instructions. Virus was resuspended 1/100 of the original volume using PBS.

2.3 DNA manipulation

2.3.1 Bacterial culture

Lysogeny broth (LB) is prepared by stirring 25 g of LB (Table 2.24) in 1 l double-distilled water (ddH_2O) and autoclaving the solution. LB agar is prepared by stirring 37 g of LB agar (Table 2.24) in 1 l ddH_2O and autoclaving the solution. The antibiotics ampicillin and carbenicillin (Table 2.24) are made into a stock solution of 100 mg/ml in ddH_2O and stored at -20°C.

Before use, LB is supplemented with ampicillin at the final concentration of 100 μg/ml, to obtain a selection medium for bacteria expressing the β-lactamase gene.

LB agar is melted, carbenicillin is added at the final concentration of 100 μg/ml, and 15 ml of the resulting solution is added to Petri dishes to obtain selection plates for bacteria expressing the β-lactamase gene. For non-selective medium and dishes, antibiotics are omitted.

Day 0 For the culture, bacteria are streaked on the plate with the correct antibiotic selection and incubated in the Thermo Scientific Heraeus OVEN at 37°C O/N.

Day 1 In the morning, a colony is picked and inoculated in 5 ml of LB in a 15 ml U-bottom centrifuge tube. The culture is shaken at 250 RPM at 37°C in the New Brunswick Scientific Innova 44 incubator shaker. After 8 hours, 55 μl of the starter culture are used to inoculate 55 ml of LB in a 500 ml culture flask and incubated in the shaker at 250 RPM at 37°C O/N.

Day 2 After 16 hours from inoculation, the cells are pelleted by centrifugation at 3,500 RCF for 10 min at 4°C in a 50 ml conical tube using a Hettich centrifuge and equipped with the 5624 rotor.

The pellet is subsequently processed or stored at -20°C.

2.3.2 Preparation of chemically competent bacteria (Stbl3 E. coli)

The preparation of chemically competent Stbl3 E. coli (Table 2.24) is carried out using the kit Mix & Go E. coli Transformation Kit & Buffer Set (Table 2.24) and the ZymoBroth (Table 2.24). The buffers used are listed in Table 2.11.

Table 2.11: Buffer used for the preparation of competent bacteria

Buffer	Storing temperature
Wash buffer (2X)	4℃
Competent buffer (2X)	4℃
Dilution buffer	4℃
ZymoBroth	RT

Day 0 LB-agar plates without any antibiotics are prepared as described in subsection 2.3.1 Stbl3 E. coli are streaked on the plate and incubated in the Thermo Scientific Heraeus OVEN at 37°C O/N.

Day 1 In the evening, a colony is picked and inoculated in 5 ml of LB in a 15 ml U-bottom centrifuge tube. The culture is shaken at 250 RPM at 37°C in the New Brunswick Scientific Innova 44 shaker.

Day 2 5 ml of 1X Wash Buffer and Competent Buffer are prepared by diluting the 2X stocks with the Dilution Buffer provided. The 1X buffers are kept on ice before use. In the morning, 500 µl of the overnight culture are used to inoculate 50 ml ZymoBroth in a 500 ml culture flask. The culture is shaken at 250 RPM at 25°C in the New Brunswick Scientific Innova 44 incubator shaker. Optical density at 600 nm (OD_{600nm}) is checked every hour and cells are transferred on ice when they reached an OD_{600nm} of 0.4 - 0.6. After 10 min of incubation on ice, the cells are pelleted by centrifugation at 1,600 - 2,500 RCF for 10 min at 4°C in a 50 ml conical tube using an Avanti J-E centrifuge (Beckman Coulter). The pellet is gently resuspended in 5 ml of ice-cold Wash Buffer 1X using a rocker at 4°C and pelleted by centrifugation at 1,600 - 2,500 RCF for 10 min at 4°C in a 50 ml conical tube using an Avanti J-E centrifuge (Beckman Coulter). The pellet is gently resuspended in 5 ml of ice-cold Competent Buffer 1X and aliquoted into 25 µl aliquots in sterile PCR tubes. Stbl3 E. coli chemically competent cells are stored at -80°C.

2.3.3 Transformation of chemically competent bacteria

Chemically competent Stbl3 E. coli cells are transformed by adding 1-5 µg of plasmid DNA to the thawed cells and mixing. The mixture is incubated for 5 min on ice and then spread on a pre-warmed plate with the appropriate resistance to isolate a single clone. The plate is incubated in the Thermo Scientific Heraeus OVEN at 37°C O/N.

2.3.4 Generation of an insert using PCR (from template plasmid) for HiFi assembly

2.3.4.1 Primer design for PCR amplification of the insert from a donor plasmid

Inserts for HiFi DNA assembly can be generated by PCR. Primers are designed using the NEBuilder HiFi DNA Assembly function built in the SnapGene software as described below:

- The maps of the backbone and the insert donor vector are opened in SnapGene
- The NEBuilder HiFi DNA Assembly window is opened by following the path:

  `Actions > NEBuilder HiFi DNA Assembly > Insert Fragment...`

- In the “Vector” tab:
  - The backbone map is selected
  - “Linearize with restriction enzymes” is selected and the restriction enzymes as per Section 2.3.7 are added
- In the “Fragment” tab:
  - The map of the insert donor vector is selected
  - The insert of interest is highlighted on the map
- In the “Product” tab:
  - “Choose Overlapping PCR Primers...” is selected
  - T_m for PCR primers is set to 60°C
  - Overlapping bases are set in the interval 20-25 bp
  - T_m for the overlap is set to 50°C
  - The restrictions sites are regenerated

The primers and the assembled products obtained are saved.

For PB-TO-APEX-NES, PB-TO-ERM-APEX and PB-TO-APEX-OMM, a KuD Kozak – predicted to induce a *moderate* overexpression of the insert [Frankenfield

et al., 2020] – is added upstream of the start codon. To do so, the KuD sequence is added to the forward primer between the annealing region and the overlap region as shown in Figure 2.1.

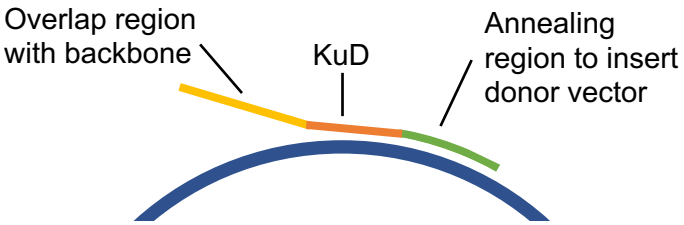


Figure 2.1: Schematics of cloning primer design

The overlap region consists of a 20-25 bp-long homology region to the backbone. If necessary a Kozak can be inserted (KuD). The annealing region anneals to the insert donor vector to allow the PCR amplification.

2.3.4.2 PCR reaction for PCR amplification of the insert from a donor plasmid

A high-fidelity Q5 polymerase (see Table 2.24) is used to amplify the insert, in order to minimise the risk of random mutations in the process. The quantities for each reagent are listed in Table 2.12.

Table 2.12: Reagents used for the amplification of an insert of interest from a donor plasmid

Component	1 rxn (µl)	8 x rxns (µl)
Q5 2x master mix	12.5	100
100 µM Forward primer	0.125	1
100 µM Reverse primer	0.125	1
Template DNA (1 ng/µl)	0.25	2
Nuclease free ddH_2O	12	96

The PCR is run on a Biorad Thermocycler in sterile PCR tubes using a gradient of annealing temperatures in order to maximise the probability of amplifying a single band and enriching for the construct of interest; the gradient is between

56°C and 70°C over 8 tubes. Table 2.13 summarises the complete PCR conditions.

Table 2.13: PCR conditions for the amplification of an insert from a donor plasmid

Step	Temperature (°C)	Time
Template denaturation	98	30 s
	98	10 s
Amplification (35 cycles)	56-70	30 s
	72	30 s/kb
Final extension	72	2 min
Hold	12	∞

2.3.5 gBlock design for HiFi cloning into I56-EF1α-mApple backbone

A.dna file with the insert of interest is created in SnapGene. To the sequence of interest, a Kozak sequence (CCCACC) is added before the start codon. Two homology regions to the backbone need to be added before the Kozak (left homology arm) and after the stop codon (right homology arm). For I56-EF1α-mApple the two homology arms are:

- left homology arm: TTCCATTTCAGGTGTCGTGAGCTAG
- right homology arm: GAATTCGTCGAGGGACCTAATAACT.

The final product is assembled *in silico* by:

- The maps of the backbone and the insert donor vector are opened in SnapGene
- The NEBuilder HiFi DNA Assembly window is opened by following the path:

  `Actions > NEBuilder HiFi DNA Assembly > Insert Fragment...`

- In the “Vector” tab:
  - The backbone map is selected

  - "Linearize with restriction enzymes" is selected and the restriction enzymes as per Section 2.3.7 are added

- In the "Fragment" tab:
  - The newly generated map of the insert of interest is selected
  - On the right the option "use directly as the Fragment" is selected
- In the "Product" tab:
  - Click "Assemble"

The gBlocks are ordered from iDT following this link `https://eu.idtdna.com/site/order/gblockentry`. Before ordering, it is necessary to codon optimise the sequence for chemical synthesis. Codon optimisation can be carried out using the iDT optimisation tool. Only the sequence from the start codon (excluded) to the stop codon is optimised. It is important not to optimise the Kozak and the homology arms because their DNA sequence cannot be altered.

2.3.6 Generation of sgRNA inserts for restriction cloning into H25-U6-sgRNA-NucBlue backbone

It is possible to generate sgRNA inserts for restriction cloning into the H25-U6-sgRNA-NucBlue backbone by ordering two oligonucleotides that will anneal and generate the insert encoding for the sgRNA and sticky ends that will pair with those of the digested backbone. A list of oligonucleotides generating sgRNAs for the whole transcriptome has been generated and published [Horlbeck et al., 2016].

The oligonucleotides are ordered in a plate so that each well contains 10 nmol of the primers couple to be annealed. The oligonucleotides are resuspended in 100 µl of ddH_2O to the final concentration of 100 µM. The annealing reaction takes place in a PCR plate at 95°C for 5 min and then at RT for 20 min; the quantities of reagent are listed in Table 2.14.

Table 2.14: Reagents used for oligonucleotides annealing

Reagent	Amount
Annealing buffer (2X) (see Table 2.15)	25 µg
Oligonucleotides (100 µM)	2 µl
ddH_2O	23 µl

Table 2.15: Reagents used to prepare 2X annealing buffer

Reagent	Concentration
Potassium acetate	200 mM
HEPES-KOH pH 7.4	60 mM
Magnesium acetate	4 mM

2.3.7 Linearisation of a backbone via restriction enzyme digestion

Linearisation of the backbones is achieved via digestion using restriction enzymes. The different backbones used were:

- I56-EF1α-mApple as a lentiviral backbone
- K4-PB-TO-hNGN2 as an all-in-one Tet-On 3G tetracycline-inducible PiggyBac backbone
- H25-U6-sgRNA-NucBlue as a sgRNA expression lentiviral backbone

The lentiviral backbone I56-EF1α-mApple is linearised using the restriction enzymes NheI-HF and EcoRI-HF (Table 2.24) in CutSmart buffer. The digestion is performed in a Biorad Thermocycler in sterile PCR tubes at 37°C for 30 min, then the enzymes are heat-inactivated at 80°C for 20 min. The quantities for each reagent are listed in Table 2.16.

The Tet-On PiggyBac backbone K4-PB-TO-hNGN2 is linearised using the restriction enzymes BamHI-HF and NruI-HF (Table 2.24) in CutSmart buffer. The digestion is performed in a Biorad Thermocycler in sterile PCR tubes at 37°C for 60 min. The quantities for each reagent are listed in Table 2.17. After the digestion,

Table 2.16: Reagents used for the digestion of I56-EF1α-mApple

Reagent	Amount
I56-EF1α-mApple	5 µg
CutSmart Buffer (10X)	1 µl
EcoRI-HF	1 µl
NheI-HF	1 µl
ddH_2O	to 10 µl

the digested backbone is separated from the insert and undigested species on an 0.8% agarose gel as described in 2.3.8. The separated band is then cut out while imaging the gel on a UV-transilluminator. The band is then purified as described in 2.3.8.

Table 2.17: Reagents used for the digestion of K4-PB-TO-hNGN2

Reagent	Amount
K4-PB-TO-hNGN2	5 µg
CutSmart Buffer (10X)	1 µl
BamHI-HF	1 µl
NruI-HF	1 µl
ddH_2O	to 10 µl

The sgRNA expression lentiviral backbone H25-U6-sgRNA-NucBlue is linearised using the restriction enzymes BlpI and BstXI (Table 2.24). The digestion is performed in a Biorad Thermocycler in sterile PCR tubes serially. The BlpI reaction is performed first in NEB buffer 2.1 O/N at 37°C following the quantities listed in Table 2.18. The BstXI reaction is performed in NEB buffer 3.1 O/N at 37°C following the quantities listed in Table 2.18. The change from NEB buffer 2.1 to NEB buffer 3.1 is performed by spiking the extra salts; the quantities for 1 ml of NEB buffer 2.1-to-3.1 spike (6X) are listed in Table 2.19. After the digestion, the digested backbone is run on an 0.8% agarose gel as described in 2.3.8. The band is then cut out while imaging the gel on a UV-transilluminator. The purified band is then purified as described in 2.3.8.

Table 2.18: Reagents used for the digestion of H25-U6-sgRNA-NucBlue

Reagent	Amount	Reagent	Amount
H25-U6-sgRNA-NucBlue	10 µg	BlpI reaction contents	20 µl
NEB buffer 2.1 (10X)	2 µl	NEB buffer 2.1-to-3.1 spike (6X)	5 µl
BlpI	3 µl	BstXI	3 µl
ddH_2O	to 20 µl	ddH_2O	2 µl

Table 2.19: Reagents used for 1 ml of NEB buffer 2.1-to-3.1 spike (6X)

Reagent	Amount
NaCl	17. 5 mg
Tris-HCl	29.1 mg
NEB buffer 2.1 (10X)	200 µl
ddH_2O	800 µl

2.3.8 Agarose gel electrophoresis of DNA and DNA purification from gel

Gel electrophoresis is employed to separate DNA strands according to size. Gels are normally used at different concentrations of agarose according to the size of the fragments that one intends to separate according to Table 2.20.

Table 2.20: Agarose concentrations used to separate DNA fragments of different sizes

Agarose concentration (% w/v)	DNA fragment range (kb)
0.8	0.8-12
1	0.5-10
1.2	0.3-7

Most of the gel electrophoreses in this thesis were performed in 0.8% agarose gels, therefore the method to make 0.8% will be described. 0.8 g of agarose are weighed and added to 100 ml of 1X TBE buffer (Table 2.24). The suspension is microwaved at 900 W in bursts of 1 min until the agarose is dissolved. The solution is left to cool for 10 min and then 10 µl of SYBR Safe (Table 2.24) are added. The solution is poured into the gel casting tray with the combs in place.

Once the gel is set, the tray and the gel can be transferred to the running cham-

ber. TBE is added to cover completely the gel. Samples are supplemented with loading buffer (not necessary for colony PCR) (Table 2.24). Samples and 1kb ladder (Table 2.24) are loaded and the gel is run at 120 V until band separation is achieved (40-50 min).

The gel can be imaged using a UV transilluminator or using a Chemidoc XRS+ system with the SYBR safe filter, which uses an XcitaBlue screen (blue light) for the excitation, which prevents DNA damage.

Gels are cut using a clean scalpel to isolate the individual bands. DNA is isolated from the gel using the Macherey-Nagel Gel and PCR Clean-up Kit (Table 2.24) as per manufacturer instructions.

2.3.9 HiFi DNA Assembly

HiFi assembly is done in a 2:1 insert:vector ratio, starting from 200 ng of the vector. The required insert DNA mass can be calculated using the NEBioCalculator. It is now possible to dilute the PCR product or the gBlock to the concentration: (insert mass needed)/µl. It is now possible to proceed to the HiFi reaction for 15 min at 50°C. The quantities for each reagent are listed in Table 2.21.

Table 2.21: Reagents used for HiFi DNA assembly

Reagent	Amount
I56-EF1α-mApple	200 ng
Insert ((insert mass needed)/µl)	1 µl
Hi-Fi master mix	5 µl
ddH_2O	to 10 µl

5 µl of the reaction are used to transform bacteria as described in subsection 2.3.3.

2.3.10 Ligation for restriction cloning of sgRNA inserts into H25-U6-sgRNA-NucBlue

The annealed oligonucleotides generated as described in subsection 2.3.6 are ligated into the digested and purified backbone H25-U6-sgRNA-NucBlue using the Mighty Mix DNA Ligation Kit (Table 2.24). First, the annealed oligonucleotides are diluted 1:20 in ddH_2O. Then inserts and backbone are ligated for 30 min at 18 °C in a Biorad Thermocycler. The quantities for each reagent are listed in Table 2.22.

Table 2.22: Reagents used for ligation of sgRNA inserts into H25-U6-sgRNA-NucBlue

Reagent	Amount
H25-U6-sgRNA-NucBlue	20 ng
Insert	0.5 µl
Mighty Mix	2.5 µl
ddH_2O	to 5 µl

2.5 µl of the reaction are used to transform bacteria as described in subsection 2.3.3.

2.3.11 Colony screening via colony PCR

In order to screen colonies colony PCR is performed (not possible for sgRNA insert cloning into H25-U6-sgRNA-NucBlue. For colony PCR, primers are designed so that one is on the backbone and the other on the insert and the amplicon is roughly 500 bp long.

A PCR plate with n x wells filled with 5 µl of iTaq Master Mix (Table 2.24) and 0.2 µl of the correct 100 µM primer pair is prepared (n = number of colonies picked). A U-bottom plate with n x wells filled with 100 µl of LB selection medium is prepared. n = number of colonies picked. The insert of a clean 10 ul pipette tip rack (the pink insert) to the top of the U-bottom plate (this will allow you to later remove tips

from the wells without cross-contamination). Single colonies are picked with a 20 µl pipette tip, then the colony is transferred to the PCR plate by pipetting up and down twice (e.g. A1), and then carefully the tip is ejected into the same well on the U-bottom plate (e.g. A1). The U-bottom plate is moved to the 37°C incubator and the PCR plate is run PCR is run on a Biorad Thermocycler. The complete PCR conditions are summarised in Table 2.23.

Table 2.23: PCR conditions for the amplification of an insert from a donor plasmid

Step	Temperature (°C)	Time
Template denaturation	95	2 min
	95	45 s
Amplification (35 cycles)	55	30 s
	72	1 min/kb
Final extension	72	5 min
Hold	12	∞

2.3.12 DNA prepping

For minipreps, colonies are picked and transferred to 6 ml of LB broth with the appropriate selection as described in subsection 2.3.1. Plasmid DNA is purified using the QiaPrep Spin MiniPrep Kit (Table 2.24) according to the manufacturer's instructions.

For midipreps, a 50 ml culture in LB broth with the appropriate selection as described in subsection 2.3.1 is prepared. Plasmid DNA is purified using the ZymoPURE II Plasmid Midiprep Kit (Table 2.24) according to the manufacturer's instructions.

For gigapreps, a 2500 ml culture in LB broth with the appropriate selection as described in subsection 2.3.1 is prepared. Plasmid DNA is purified using the ZymoPURE II Plasmid Gigaprep Kit (Table 2.24) according to the manufacturer's instructions.

2.3.13 Colony screening via sequencing

To confirm that the constructs generated are correct, the clones that passed the colony PCR screening (or two randomly picked for those that cannot be colony PCR screening) are Sanger sequenced.

Primer3plus is used to design the sequencing primers. In the “Main” tab, the insert sequence and 250 bp upstream and downstream of the cloning site are copied in the window. In the “Task” menu “Pick sequencing primers” is selected. Finally “Pick Primers” is clicked. This way primers spanning the length of the insert and on the destination backbone are generated. Primers should be roughly 500 bp apart.

The sequencing is performed by submitting 5 µl of miniprep and the relative primers to SourceBioscience.

2.3.14 Materials

Table 2.24: List of reagents used for DNA manipulation

Item	Supplier	Catalogue number
Ampicillin	Sigma-Aldrich	A0166-5G
BamHI-HF	NEB	R3136L
BlpI	NEB	R0585L
BstXI	NEB	R0113L
Carbenicillin	Gibco	10177012
EcoRI-HF	NEB	R3101L
Gel and PCR Clean-up Kit	Macherey-Nagel	12303368
Gel Loading Dye, Purple (6X)	NEB	B7024S
iTaq Universal Probes Supermix	Bio-Rad	1725131
LB Agar, powder	Invitrogen	22700025
LB Broth, powder	Invitrogen	12780052
Mighty Mix DNA Ligation Kit	Takara Bio	6023
Mix & Go E. coli Transformation Kit & Buffer Set	Zymo	T3002
NEBuilder HiFi DNA Assembly Master Mix	NEB	E2621L
NheI-HF	NEB	R3131L

NruI-HF	NEB	R3192L
Q5 High-Fidelity 2X Master Mix	NEB	M0492L
QiaPrep Spin MiniPrep Kit	Qiagen	27106
Stbl3 Chemically Competent E. coli	Invitrogen	C737303
SYBR Safe DNA Gel Stain	Invitrogen	S33102
Tris-Borate-EDTA Buffer 10x concentrate	Sigma-Aldrich	T4415-4L
ZymoBroth	Zymo	M3015-500
ZymoPURE II Plasmid Gigaprep Kit	Zymo	D4204
ZymoPURE II Plasmid Midiprep Kit	Zymo	D4200

Table 2.25: List of plasmids used in this thesis. The following abbreviations are used in the Table: A.O. for annealed oligonucleotides and Rest. C. for restriction cloning

Plasmid name	Source	Insert	Backbone	Insert linearisation	Cloning technique
I56-EF1α-mApple	courtesy of S. W. Humble				
LV-EF1α-RGECO1mt	This thesis	RGECO*mt* Addgene #46021	I56-EF1α-mApple	gBlock	HiFi DNA assembly
LV-EF1α-GCEPIA1er	This thesis	GCEPIA*er* Addgene #105012	I56-EF1α-mApple	gBlock	HiFi DNA assembly
K13-EF1α-transposase	Transposase, courtesy of S. W. Humble				
K23-PB-CAG-dCas9-KRAB	dCas9, courtesy of S. W. Humble				
K4-PB-TO-hNGN2	courtesy of S. W. Humble				
PB-TO-APEX-NES	This thesis	APEX-NES, Addgene #92158	K4-PB-TO-hNGN2	PCR	HiFi DNA assembly
PB-TO-ERM-APEX	This thesis	ERM-APEX, Addgene #79055	K4-PB-TO-hNGN2	PCR	HiFi DNA assembly
PB-TO-APEX-OMM	This thesis	APEX-OMM, Addgene #79056	K4-PB-TO-hNGN2	PCR	HiFi DNA assembly
H25-U6-sgRNA-NucBlue					
LV-U6-D-7A-ATP2A1-1	This thesis	sgRNA against ATP2A1 gene, [Horlbeck et al., 2016]	H25-U6-sgRNA-NucBlue	A.O.	Rest. C.

LV-U6-D-7B-ATP2A1-2	This thesis	sgRNA against ATP2A1 gene, [Horlbeck et al., 2016]	H25-U6-sgRNA-NucBlue	A.O.	Rest. C.
LV-U6-D-7C-ATP2A2-1	This thesis	sgRNA against ATP2A2 gene, [Horlbeck et al., 2016]	H25-U6-sgRNA-NucBlue	A.O.	Rest. C.
LV-U6-D-7D-ATP2A2-2	This thesis	sgRNA against ATP2A2 gene, [Horlbeck et al., 2016]	H25-U6-sgRNA-NucBlue	A.O.	Rest. C.
LV-U6-D-7E-RYR2-1	This thesis	sgRNA against RYR2 gene, [Horlbeck et al., 2016]	H25-U6-sgRNA-NucBlue	A.O.	Rest. C.
LV-U6-D-7F-RYR2-2	This thesis	sgRNA against RYR2 gene, [Horlbeck et al., 2016]	H25-U6-sgRNA-NucBlue	A.O.	Rest. C.
LV-U6-D-7G-RYR3-1	This thesis	sgRNA against RYR3 gene, [Horlbeck et al., 2016]	H25-U6-sgRNA-NucBlue	A.O.	Rest. C.
LV-U6-D-7H-RYR3-2	This thesis	sgRNA against RYR3 gene, [Horlbeck et al., 2016]	H25-U6-sgRNA-NucBlue	A.O.	Rest. C.
LV-U6-D-8A-RMDN3-1	This thesis	sgRNA against RMDN3 gene, [Horlbeck et al., 2016]	H25-U6-sgRNA-NucBlue	A.O.	Rest. C.
LV-U6-D-8B-RMDN3-2	This thesis	sgRNA against RMDN3 gene, [Horlbeck et al., 2016]	H25-U6-sgRNA-NucBlue	A.O.	Rest. C.
LV-U6-D-8C-SYNJ2BP-1	This thesis	sgRNA against SYNJ2BP gene, [Horlbeck et al., 2016]	H25-U6-sgRNA-NucBlue	A.O.	Rest. C.

LV-U6-D-8D-SYNJ2BP-2	This thesis	sgRNA against SYNJ2BP gene, [Horlbeck et al., 2016]	H25-U6-sgRNA-NucBlue	A.O.	Rest. C.
LV-U6-D-8E-RRBP1-1	This thesis	sgRNA against RRBP1 gene, [Horlbeck et al., 2016]	H25-U6-sgRNA-NucBlue	A.O.	Rest. C.
LV-U6-D-8F-RRBP1-2	This thesis	sgRNA against RRBP1 gene, [Horlbeck et al., 2016]	H25-U6-sgRNA-NucBlue	A.O.	Rest. C.
LV-U6-D-8G-OSBPL5-1	This thesis	sgRNA against OSBPL5 gene, [Horlbeck et al., 2016]	H25-U6-sgRNA-NucBlue	A.O.	Rest. C.
LV-U6-D-8H-OSBPL5-2	This thesis	sgRNA against OSBPL5 gene, [Horlbeck et al., 2016]	H25-U6-sgRNA-NucBlue	A.O.	Rest. C.
LV-U6-D-9A-OSBPL8-1	This thesis	sgRNA against OSBPL8 gene, [Horlbeck et al., 2016]	H25-U6-sgRNA-NucBlue	A.O.	Rest. C.
LV-U6-D-9B-OSBPL8-2	This thesis	sgRNA against OSBPL8 gene, [Horlbeck et al., 2016]	H25-U6-sgRNA-NucBlue	A.O.	Rest. C.
LV-U6-D-9C-FIS1-1	This thesis	sgRNA against FIS1 gene, [Horlbeck et al., 2016]	H25-U6-sgRNA-NucBlue	A.O.	Rest. C.
LV-U6-D-9D-FIS1-2	This thesis	sgRNA against FIS1 gene, [Horlbeck et al., 2016]	H25-U6-sgRNA-NucBlue	A.O.	Rest. C.
LV-U6-D-9E-BCAP31-1	This thesis	sgRNA against BCAP31 gene, [Horlbeck et al., 2016]	H25-U6-sgRNA-NucBlue	A.O.	Rest. C.

LV-U6-D-9F-BCAP31-2	This thesis	sgRNA against BCAP31 gene, [Horlbeck et al., 2016]	H25-U6-sgRNA-NucBlue	A.O.	Rest. C.
LV-U6-D-9G-MFN1-1	This thesis	sgRNA against MFN1 gene, [Horlbeck et al., 2016]	H25-U6-sgRNA-NucBlue	A.O.	Rest. C.
LV-U6-D-9H-MFN1-2	This thesis	sgRNA against MFN1 gene, [Horlbeck et al., 2016]	H25-U6-sgRNA-NucBlue	A.O.	Rest. C.
LV-U6-D-10A-MFN2-1	This thesis	sgRNA against MFN2 gene, [Horlbeck et al., 2016]	H25-U6-sgRNA-NucBlue	A.O.	Rest. C.
LV-U6-D-10B-MFN2-2	This thesis	sgRNA against MFN1 gene, [Horlbeck et al., 2016]	H25-U6-sgRNA-NucBlue	A.O.	Rest. C.
LV-U6-D-10C-PACS2-1	This thesis	sgRNA against PACS2 gene, [Horlbeck et al., 2016]	H25-U6-sgRNA-NucBlue	A.O.	Rest. C.
LV-U6-D-10D-PACS2-2	This thesis	sgRNA against PACS2 gene, [Horlbeck et al., 2016]	H25-U6-sgRNA-NucBlue	A.O.	Rest. C.
LV-U6-A-2A-VAPB-1	sgRNA against VAPB gene, courtesy of S. W. Humble				

LV-U6-A-2B-VAPB-2	sgRNA against VAPB gene, courtesy of S. W. Humble
LV-U6-M-11G-ITPR1-1	sgRNA against ITPR1 gene, courtesy of S. W. Humble
LV-U6-M-11H-ITPR1-2	sgRNA against ITPR1 gene, courtesy of S. W. Humble
LV-U6-M-12A-ITPR2-1	sgRNA against ITPR2 gene, courtesy of S. W. Humble
LV-U6-M-12B-ITPR2-2	sgRNA against ITPR2 gene, courtesy of S. W. Humble
LV-U6-M-12C-VDAC1-1	sgRNA against VDAC1 gene, courtesy of S. W. Humble

LV-U6-M-12D-VDAC1-2	sgRNA against VDAC1 gene, courtesy of S. W. Humble
LV-U6-M-12E-MCU-1	sgRNA against MCU gene, courtesy of S. W. Humble
LV-U6-M-12F-MCU-2	sgRNA against MCU gene, courtesy of S. W. Humble
LV-U6-12A-1872	control non-targeting sgRNA, courtesy of S. W. Humble
LV-U6-12B-1873	control non-targeting sgRNA, courtesy of S. W. Humble

Table 2.26: List of primers used for cloning

Name	Sequence	Task	Plasmid	Binding
A01	CTCACTCCCTTGCTTCTTCG	Sequencing	LV-EF1α-RGECO1mt	Insert
A02	GAGAAGACAGGCGACCAATC	Sequencing	LV-EF1α-RGECO1mt	Insert
A03	TCTCACACAATGAAGACTACACGA	Sequencing	LV-EF1α-RGECO1mt	Insert
A04	GATAGTTCCCTGCAGGATGG	Sequencing	LV-EF1α-RGECO1mt	Insert
A05	ATCCGCGACTCGTATCATCT	Sequencing	LV-EF1α-RGECO1mt	Insert
A06	gggatggagctgtatcatcct	Sequencing	LV-EF1α-GCEPIAer	Insert
A07	gctcgtcggccttgatatag	Sequencing	LV-EF1α-GCEPIAer	Insert
A08	acgtaaacggccacaagttc	Sequencing	LV-EF1α-GCEPIAer	Insert
A09	gggcacaagctggagtaca	Sequencing	LV-EF1α-GCEPIAer	Insert
A10	gccccattcagatcctcttc	Sequencing	LV-EF1α-GCEPIAer	Insert
A16	tggactacaaggatgacgacg	Sequencing	PB-TO-APEX2-OMM	Insert
A17	agcgctaacaacggtcttga	Sequencing	PB-TO-APEX2-OMM	Insert
A18	ctttccgagcttgggtttgc	Sequencing	PB-TO-APEX2-OMM	Insert
A19	ggagcattagaggagcgcat	Sequencing	PB-TO-APEX2-OMM	Insert
A20	tcaccactcaacaactccgt	Sequencing	PB-TO-APEX2-OMM	Insert
A21	accctgtggtcgtgctgg	Sequencing	PB-TO-ERM-APEX2	Insert
A22	cgtttggcattccactctgc	Sequencing	PB-TO-ERM-APEX2	Insert
A23	tgtattccgccctctcgttg	Sequencing	PB-TO-ERM-APEX2	Insert
A24	atcagcactcacagttgggt	Sequencing	PB-TO-ERM-APEX2	Insert
A25	gctccaatagtgtgaccccc	Sequencing	PB-TO-ERM-APEX2	Insert
A26	tggactacaaggatgacgacg	Sequencing	PB-TO-APEX2-NES	Insert
A27	agcgctaacaacggtcttga	Sequencing	PB-TO-APEX2-NES	Insert
A28	gattacgctgaggctcacca	Sequencing	PB-TO-APEX2-NES	Insert
A29	tctcagcgatgaagcctctg	Sequencing	PB-TO-APEX2-NES	Insert
A30	tcaccactcaacaactccgt	Sequencing	PB-TO-APEX2-NES	Insert

C13	AATTGTCAGTGCCCAACAGC	Sequencing	LV-EF1α-RGECO1mt, LV-EF1α-GCEPIAer	Backbone
C31	gacatgataagatacattga	Sequencing	PB-TO-APEX2-NES, PB-TO-ERM-APEX2, PB-TO-APEX2-OMM	Backbone
K4-PB-TO_APEX2-NES_F	caagttggggtgggcgatcgatTCGCGAttagtcc a g g g t c a g g c g c	Cloning	PB-TO-APEX2-NES	
K4-PB-TO_APEX2-NES_R	cgtaccacttcctaccctcgtaaaGGATCCggga tgggttgatttatggactacaaggatgacgacg	Cloning	PB-TO-APEX2-NES	
K4-PB-TO_APEX2-OMM_F	cgtaccacttcctaccctcgtaaaGGATCCggga tgggttgatttatggactacaaggatgacgacg	Cloning	PB-TO-APEX2-OMM	
K4-PB-TO_APEX2-OMM_R	caagttggggtgggcgatcgatTCGCGActagtg c a g a c g c c g c c	Cloning	PB-TO-APEX2-OMM	
K4-PB-TO_ERM-APEX2_F	cgtaccacttcctaccctcgtaaaGGATCCggga t g g g t t g a t t t a t g g a c c c t g t g g t c g	Cloning	PB-TO-ERM-APEX2	
K4-PB-TO_ERM-APEX2_R	caagttggggtgggcgatcgatTCGCGAtcaggt g c t g t c c a g g c	Cloning	PB-TO-ERM-APEX2	

2.4 Ca^{2+} imaging in iPSC derived neuronal models

2.4.1 Fura-2 AM Ca^{2+} imaging

For Fura-2 AM Ca^{2+} imaging, DAns and i^3 neurons are plated down as described in Section 2.1.3.1 at the concentrations listed in Table 2.6. For Fura-2 AM Ca^{2+} imaging assay, the Fura-2 QBT Calcium Kit (Molecular Devices) is used. Fura-2 AM is diluted to a 5 mM stock solution in HBSS without Ca^{2+} or Mg^{2+} and supplemented with 20 mM HEPES buffer, pH 7.4. To load the cells, Fura-2 AM is diluted to 2.5 mM in supplemented medium without growth factors. 100% of cell medium is replaced with the diluted Fura-2 AM following the volumes listed in Table 2.7 and incubated for 1-1.5 h at 37°C. At the end of the incubation, the plate is read using a FlexStation 3 Multi-Mode Microplate Reader. Fura-2 AM has a dual absorption spectrum at 340 nm and 380 nm and a single emission at 510 nm. When Fura-2 AM binds to Ca^{2+} the absorption at 340 nm increases by 3 fold and the one at 380 nm decreases by 10 fold, therefore it is possible to obtain a ratiometric measure of the calcium content by computing the 340/380 ratio.

The FlexStation 3 Multi-Mode Microplate Reader is programmed to read each column of a plate every 4 s for 100 s and to inject ionomycin to the cells at 30 s (between the 8th and the 9th read). Ionomycin is diluted to 3x the working concentration (15 μM) in HBSS without Ca^{2+} or Mg^{2+} and supplemented with 20 mM HEPES buffer, pH 7.4. The correct volume of ionomycin is injected into the cell wells so that it is diluted to the working concentration of 5 μM; for example, 25 μl are injected in a 96 well half area.

For the analysis, the 340/380 ratio is computed, and the first 8 reads (from t = 0 s to t = 28 s, i.e. the baseline) are averaged to obtain the average baseline and then subtracted to all the timepoints, to obtain a normalised trace for each well. The maximum intensity (peak amplitude) of the normalised trace is found and the

area under the curve (AUC) is calculated using the left rectangular approximation method. Non-responding wells are excluded from the analysis. The wells that pass quality control are averaged by line to contribute to the line average for that differentiation.

All results from different differentiations are averaged by line to contribute to the final average for that line. Genotypes are then compared as stated for each individual piece of data.

2.4.2 Ca^{2+} imaging using subcellular compartment-entrapped GECI

For GECI Ca^{2+} imaging, DAns are plated down as described in Section 2.1.3.1 at the concentrations listed in Table 2.6 and double infected with the two viruses (multiplexed) as described in Section 2.1.3.2. Just before imaging, 100% of the medium on the cells is replaced with HBSS with Ca^{2+} or Mg^{2+} and supplemented with 15 mM HEPES buffer and 10 mM glucose, pH 7.4 to a final volume of 40 µl per well in a 96-well half area. Plates are imaged using an INCELL 6000 imager. The imaging was performed using a 20X water objective. GCEPIA*er* and RGECO*mt* were respectively imaged using the FITC (100 ms exposure time, 100% laser power) and dsRed (200 ms exposure, 100% laser power) channels. The imaging takes place at 37°C and the cells are imaged for 64 s. Ionomycin is injected at 16 s (5th read). Ionomycin is diluted to 3x working concentration (15 µM) in HBSS with Ca^{2+} or Mg^{2+} and supplemented with 15 mM HEPES buffer and 10 mM glucose, pH 7.4.

The images are analysed using the Columbus software. The first group of blocks of the analysis pipeline is aimed at finding and selecting out-of-focus regions – mostly, because of cells clumping or peeling. The second group of blocks is aimed at finding cells outside of the out-of-focus region and measuring their mor-

phological properties and fluorescence intensity. The final group of blocks selects the cells that are the most likely to be neuronal cells based on their morphology and cells that express the constructs at too low levels. The cells are then tracked to obtain their coordinates on the image and the intensity of each cell is saved at each time point. The pipeline is summarised in Figure 2.2

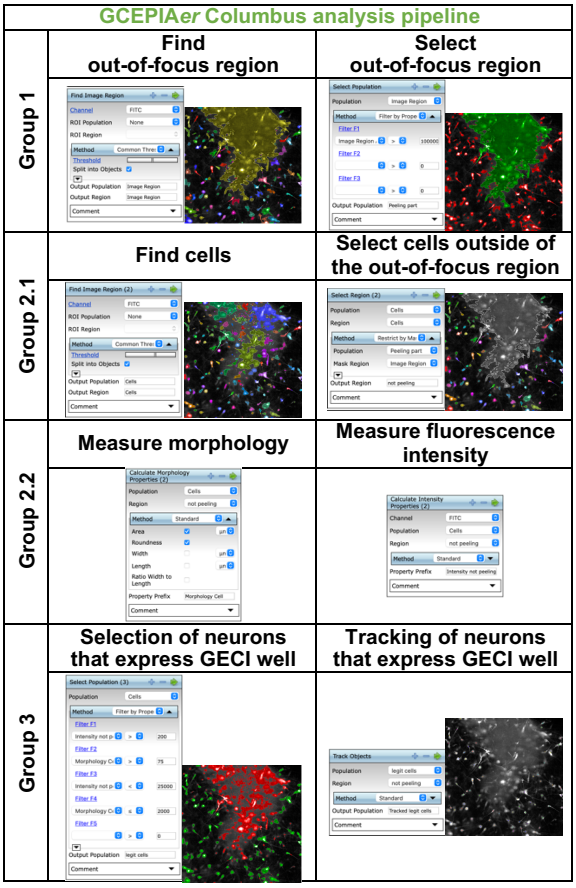


Figure 2.2: GECI Columbus analysis pipeline

The single-cell data is then processed using a MATLAB script that calculates $-(F - F_0)/F_0$ for the ER analysis and $(F - F_0)/F_0$ for the mitochondrial analysis of each individual cell. The first time point is always discarded from the analysis because it is where the biggest drop-off in fluorescence due to bleaching is observed; therefore the F_0 is calculated by averaging timepoints 1 to 4. The AUC is calculated using the left rectangular approximation method. Wells with less than 20 cells and

AUC outliers are excluded from the rest of the analysis. The cells that pass quality control are averaged by line to contribute to the line average for that differentiation.

All results from different differentiation are averaged by line to contribute to the final average for that line. Genotypes are then compared as stated for each individual piece of data.

2.5 Other assays

2.5.1 RT-qPCR

Total RNA are extracted RNeasy mini kit (Qiagen) and cDNA is synthesized using SuperScript III Reverse Transcriptase (Thermo Fisher) according to manufacturers' instructions. qPCR is performed using the SYBR Green qPCR mix (Thermo Fisher). PCR consisted in 40 cycles of amplification with denaturation at 95°C for 15 s, annealing at 60°Cfor 25 s, and extension at 72°Cfor 20 s. Gene expression was calculated using the $\Delta\Delta C_{CT}$ method.

2.5.2 Western Blot

For Western Blot analyses, total cell extracts are prepared in NP-40 lysis buffer (Tris-HCl pH 8 20 mM, NaCl 20 mM, glycerol 10%, NP-40 0.3%, EDTA 10 mM) supplemented with protease and phosphatase inhibitors. Lysis is performed for 30 min on ice, then the extract was clarified by centrifugation at 1500 RCF for 10 min.

Membrane/cytoplasm fractionation is performed by lysing the cells in digitonin lysis buffer (HEPES pH 7.5 50 mM, digitonin 10 mg/ml, NaCl 150 mM) supplemented with protease and phosphatase inhibitors. Lysis is performed for 30 min on ice, then the extract was clarified by centrifugation at 6000 RCF for 5 min. The supernatant represents the cytoplasmic fraction. The pellet is resuspended in NP-

40 membrane solubilisation buffer (HEPES pH 7.5 50 mM, NP-40 0.3%, 150 mM NaCl) and incubated on ice for 10 min. The membrane suspension is spun at 1500 RCF at 4°Cfor 5 min. The supernatant represents the membrane fraction.

Lysates are quantified using Bradford assay or BCA assay and for each sample, 30μg of each fraction were loaded. Proteins were separated by 8% or 4-20% Tris-Glycine SDS-PAGE (Bio-Rad) and electro-blotted onto PVDF membranes (Bio-Rad). Membranes were blocked (5% wt/vol nonfat dry milk) and incubated with the primary antibody (O/N, 4°C) and with HRP-conjugated secondary antibodies (1 h, RT).

2.5.3 APEX2 labelling and pull-down

APEX2 labelling and pull-down are performed as described in [Hung et al., 2016], with the only difference being that samples were lysed in NP-40 lysis buffer to prevent nuclear lysis.

2.6 Statistical Analysis

In each graph, each data point represents an individual patient line averaged across 3-5 differentiations or an individual differentiation, as stated in each Figure legend. Individual patient lines are used as data points when data is obtained from lines derived from different individuals to account for the biological difference across individuals; data is averaged across multiple differentiations to account for technical differences arising from independent differentiations. Individual differentiations are used as data points when data is obtained from isogenic lines compared to their isogenic controls in order to account for differences arising from independent differentiations. Data summary is expressed as the mean (line) ± SEM (whiskers). Significance is indicated as $*$ for $p < 0.05$.

For data analysis, N is intended as the number of data points in each graph. For data analysis, differences between means are assessed using Mann-Whitney, Friedman or t-test, as stated in each figure legend. Non parametric tests are preferred due to the small N numbers. Data from each differentiation is obtained as an average of the data obtained from 100-1000 cells in 3-5 individual wells.

All tests are performed using GraphPad Prism.

Chapter 3

Investigation of Ca^{2+} deficits in iPSC-derived DAns from PD patients

3.1 Introduction and aims

Ca^{2+} is a key signalling molecule involved in a plethora of cellular functions such as synaptic transmission, neurotransmitter release, metabolism and gene regulation [Brini et al., 2012]. ER luminal Ca^{2+} has a role in regulating ER Ca^{2+}-binding chaperones involved in protein folding as well as cytoplasmic Ca^{2+} signalling [Brini et al., 2012]. ER Ca^{2+} measures revealed that ER Ca^{2+} levels (1 mM) are several orders of magnitude higher than cytoplasmic Ca^{2+} (100 nM), but ER Ca^{2+} is mostly bound to proteins which require Ca^{2+} for their function. Alterations in Ca^{2+} levels, particularly within the ER, may affect ER Ca^{2+}-binding chaperones and therefore jeopardise the balanced maintenance of protein folding within the cell, causing accumulation of misfolded proteins. This could be of particular interest for PD and neurodegenerative diseases in general, as these diseases are often associated with the accumulation of proteinaceous aggregates.

The mitochondria provide chemical energy to the cell through the citric acid

cycle and the electron transport chain. Pyruvate-, isocitrate-, and α-ketoglutarate dehydrogenases – enzymes of the citric acid cycle – need Ca^{2+} as a cofactor for their function.

It is particularly interesting to study the contribution of ER and mitochondria to Ca^{2+} homeostasis and dyshomeostasis in PD, as ER and mitochondria are crucial for the regulation of Ca^{2+} homeostasis and, at the same time, Ca^{2+} is central for the physiology of these two organelles.

One of the most common ways to study calcium dynamics is to use Ca^{2+} imaging techniques, including the employment of small molecules and genetically encoded Ca^{2+} indicators (GECIs). Fura-2 AM is a cell-permeant ratiometric fluorescent dye that binds to free cytoplasmic Ca^{2+} [Grynkiewicz et al., 1985]. GECIs are generated by the fusion of fluorescent proteins and Ca^{2+}-binding proteins (often calmodulin). These indicators can be engineered to be suitable to study Ca^{2+}-dynamics at the subcellular compartment level. Although the Fura-2 AM assay has several advantages as it is easy to load in the cells, is not invasive and is ratiometric, it may not be suitable to study in detail Ca^{2+} dynamics in the cell. On the other hand, the use of organelle-entrapped GECIs affords the possibility to obtain precise compartmentalisation of the indicator relying on well-characterised target peptide sequences and therefore allows Ca^{2+} monitoring at the subcellular compartment level. The use of indicators of different colours allows us to multiplex and monitor two organelles and the cytoplasm in the same cell and therefore to monitor specific Ca^{2+} routes in the cell.

Ca^{2+} imaging has only begun to bring new insight into the role of Ca^{2+} in the context of neurodegeneration. Of note, alterations in Ca^{2+} homeostasis have been highlighted this way in DAns derived from patients harbouring the *GBA-L444P* [Schöndorf et al., 2014] and the *LRRK2-G2019S* mutations [Korecka et al., 2019]

and in several other models of PD.

In this chapter, Fura-2 AM, a green intensiometric GECI in the ER referred to as GCEPIA*er* [Suzuki et al., 2014], and a red intensiometric GECI in the mitochondria referred to as RGECO*mt* [Wu et al., 2013] are employed to analyse Ca^{2+} dynamics in PD iPSC-derived DAns at the subcellular compartment level. These tools have been used in conjunction with ionomycin, which increases the permeability of membranes to Ca^{2+} and therefore depletes intracellular stores by transporting ions through their membranes. Therefore, ionomycin-induced Ca^{2+} release can be used as a proxy for intracellular Ca^{2+} content.

We also attempted to employ allosteric modulators of specific Ca^{2+} channels located at the ER membrane, to pharmacologically dissect the source of the deficit.

Aims of the chapter

- Investigate Ca^{2+} dynamics in DAns harbouring mutations in the *SNCA* or *GBA* genes using a Fura-2 AM-based assay
- Optimise organelle-entrapped GECIs in iPSC-derived DAns
- Investigate ER Ca^{2+} dynamics in DAns harbouring mutations in the *SNCA* or *GBA* genes using a GCEPIA*er*-based assay
- Investigate mitochondrial Ca^{2+} dynamics in DAns harbouring mutations in the *SNCA* or *GBA* genes using a RGECO*mt*-based assay
- Attempt a functional dissection of the cause of the changes in Ca^{2+} dynamics in PD patients using a pharmacological approach

3.2 Investigation of Ca^{2+} dynamics in DAns harbouring mutations in the *SNCA* or *GBA* genes using a Fura-2 AM-based assay

Correct intracellular Ca^{2+} handling is required for DAn function. Whole intracellular Ca^{2+} content was measured in DAns using a FlexStation 3 Multi-Mode Microplate Reader. Cells were loaded with the ratiometric cytoplasmic Ca^{2+} sensor Fura-2 AM. Ionomycin (5 μM) was applied to the cells to increase membrane permeability to Ca^{2+}; the application of ionomycin induces an increase in the Fura-2 AM ratio due to permeabilisation of intracellular Ca^{2+} compartments, therefore the Ca^{2+} response can be interpreted as a measure of Ca^{2+} content in the subcellular compartments of the cell.

Cell cultures containing DAns derived from patients carrying the *SNCA*-Trp and *SNCA-A53T* mutations were probed and the average Ca^{2+} traces of controls and patients are shown in Figure 3.1 A and E. No differences between controls and patients were observed at the baseline level (Figure 3.1 B and F). However, the mutated cells showed decreased Ca^{2+} release upon ionomycin stimulation, which was quantified by measuring the amplitude of the peak response and the area under the curve (AUC) (Figure 3.1 C-D and G-H). This suggests that mutated cells display decreased Ca^{2+} concentration in their Ca^{2+} stores, which may be due to alterations in Ca^{2+} homeostasis.

Interestingly, knock-out of the *SNCA* gene appears to not have any effect in Ca^{2+} handling as three *SNCA*-KO clones appear to release the same amount of Ca^{2+} (Figure 3.1 I-L) as their isogenic control.

Ca^{2+} content was also studied in cell cultures containing DAns derived from patients carrying the *GBA-N370S* mutation and the average Ca^{2+} traces of controls

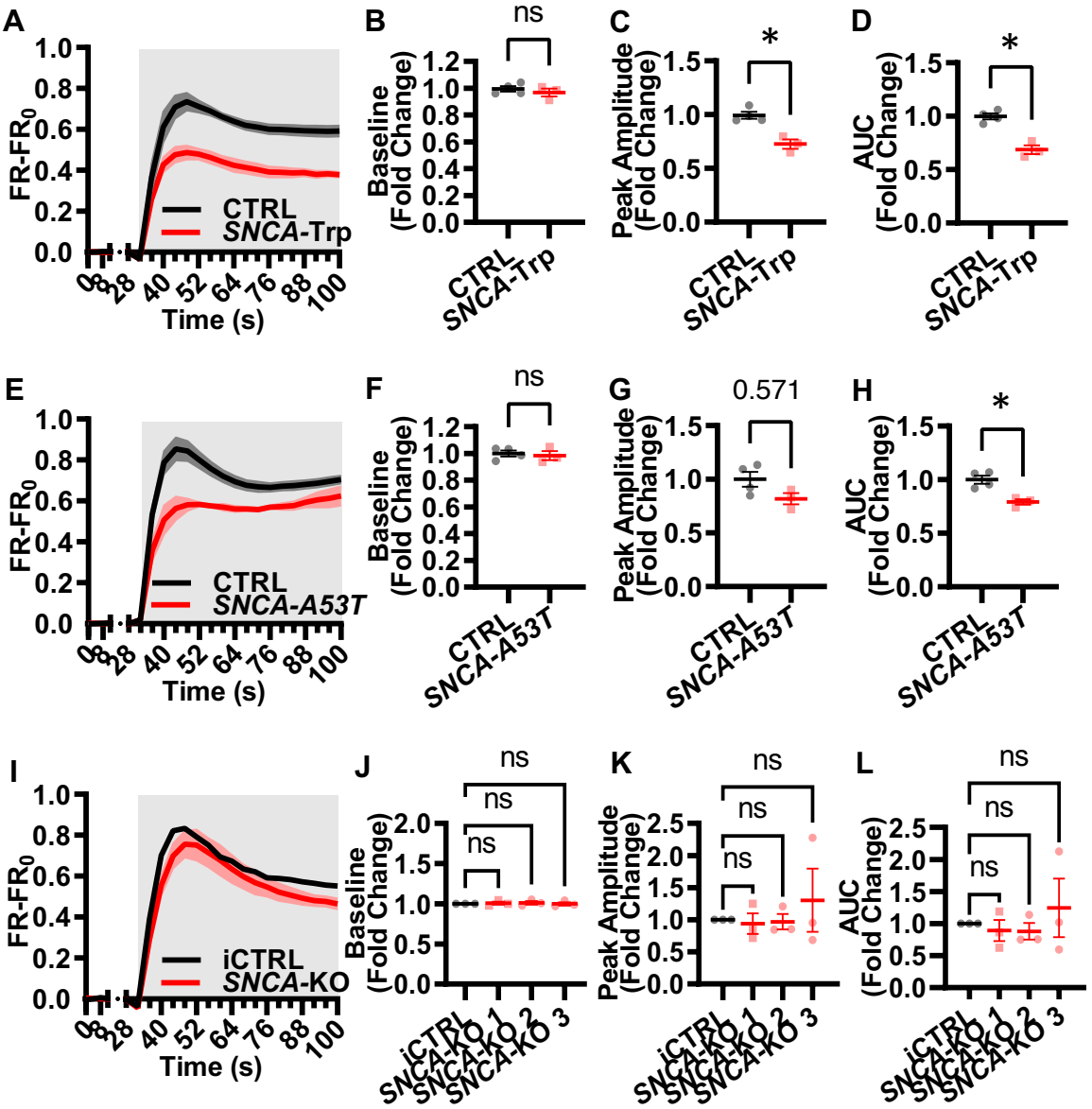


Figure 3.1: *SNCA*-Trp and *SNCA-A53T* DAns display decreased intracellular Ca^{2+} release upon ionomycin stimulation in a Fura-2 AM-based assay

(A) Trace showing the average of the Fura-2 ratio in response to ionomycin (grey box) in controls (4 lines) and *SNCA*-Trp (3 clones of 1 line). **(B-D)** Baseline, peak amplitude and AUC of the Fura-2 trace in *SNCA*-Trp. Each data point represents an individual line averaged across 4 independent differentiations. Comparison between genotypes: one-tailed Mann-Whitney test. $*$ = $p < 0.05$. **(E)** Trace showing the average of the Fura-2 ratio in response to ionomycin (grey box) in controls (4 lines) and *SNCA-A53T* (3 lines). **(F-H)** Baseline, peak amplitude and AUC of the Fura-2 trace in *SNCA-A53T*. Each data point represents an individual line averaged across 3 independent differentiations. Comparison between genotypes: one-tailed Mann-Whitney test. $*$ = $p < 0.05$. **(I)** Trace showing the average of the Fura-2 ratio in response to ionomycin (grey box) in *SNCA*-KO (3 clones of 1 line) and their isogenic WT control (iCTRL). **(J-L)** Baseline, peak amplitude and AUC of the Fura-2 trace in *SNCA*-KO. Each data point represents an individual differentiation. Comparison between genotypes: Friedman test. $*$ = $p < 0.05$.

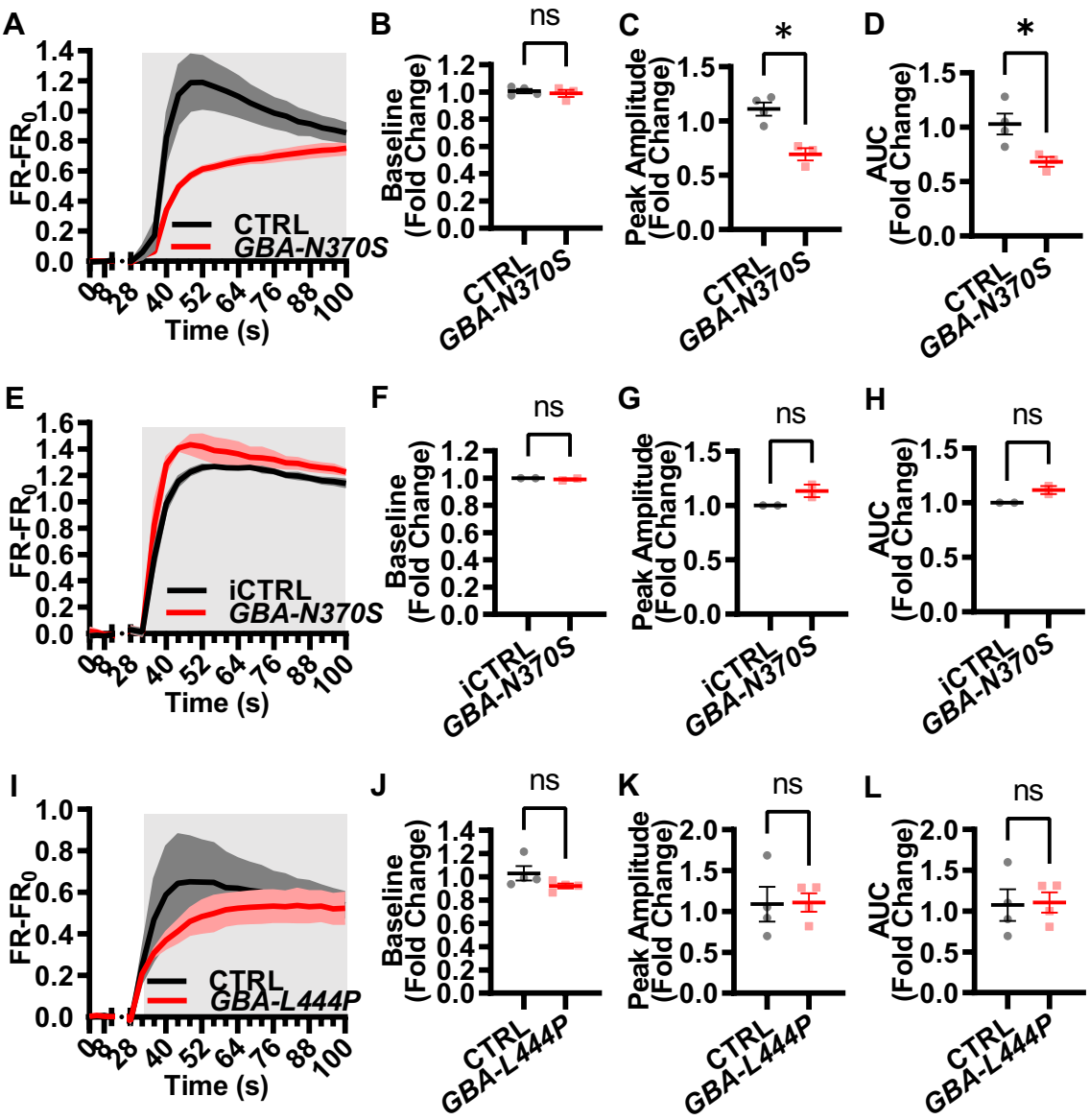


Figure 3.2: *GBA-N370S* but not *GBA-L444P* DAns display decreased intracellular Ca^{2+} release upon ionomycin stimulation in a Fura-2 AM-based assay

(A) Trace showing the average of the Fura-2 ratio in response to ionomycin (grey box) in controls (4 lines) and and *GBA-N370S* (3 lines). **(B-D)** Baseline, peak amplitude and AUC of the Fura-2 trace in *GBA-N370S*. Each data point represents an individual line averaged across 4 independent differentiations. Comparison between genotypes: one-tailed Mann-Whitney test. $*$ = $p < 0.05$. **(E)** Trace showing the average of the Fura-2 ratio in response to ionomycin (grey box) in *GBA-N370S* (1 line) and its isogenic WT control (iCTRL). **(F-H)** Baseline, peak amplitude and AUC of the Fura-2 trace in *GBA-N370S*. Each data point represents an individual differentiation. Comparison between genotypes: one-tailed Mann-Whitney test. $*$ = $p < 0.05$. **(I)** Trace showing the average of the Fura-2 ratio in response to ionomycin (grey box) in controls (4 lines) and *GBA-L444P* (4 lines). **(J-L)** Baseline, peak amplitude and AUC of the Fura-2 trace in *GBA-L444P*. Each data point represents an individual line averaged across 3 independent differentiations. Comparison between genotypes: one-tailed Mann-Whitney test. $*$ = $p < 0.05$.

and patients are shown in Figure 3.2 A and E. No differences between controls and patients were observed at the baseline level (Figure 3.2 B and F). However, the cells harbouring the *GBA-N370S* mutation showed decreased Ca^{2+} release upon ionomycin stimulation, which was quantified by measuring the amplitude of the peak response and the AUC (Figure 3.2 C and D), suggesting that those patients have lower Ca^{2+} concentration in their Ca^{2+} stores.

Heterozygous mutations in the *GBA* gene show very low (10-20%) penetrance, therefore the rest of the genetic landscape and environment play a big role in the aetiology of PD in patients carrying mutations in the gene. Therefore, I sought to investigate whether the *GBA-N370S* mutation might be directly involved in developing the phenotype. To do so, I measured subcellular compartment Ca^{2+} content in a patient carrying the *GBA-N370S* mutation and its isogenic control. In this experimental setting, no significant Ca^{2+} content difference was observed (Figure 3.2 E-H), thus suggesting a potential involvement of other genetic risk factors in the development of a Ca^{2+} content phenotype.

Ca^{2+} content was also studied in DAns derived from patients carrying the *GBA-L444P* mutation. The *GBA-L444P* patients did not appear to be significantly different from controls (Figure 3.2 I-L). However, a large line-to-line and differentiation-to-differentiation variability was observed in these lines. Therefore, no definitive conclusions can be drawn.

3.3 Cloning of GECI into a lentiviral backbone

In order to generate the GECI constructs LV-EF1α-GCEPIAer and LV-EF1α-RGECO1mt, gBlocks were designed for GCEPIA*er* and RGECO*mt* using the sequences respectively developed by [Suzuki et al., 2014, Wu et al., 2013]. The inserts were cloned into the I56-EF1α-mApple backbone. Colonies underwent a first round of

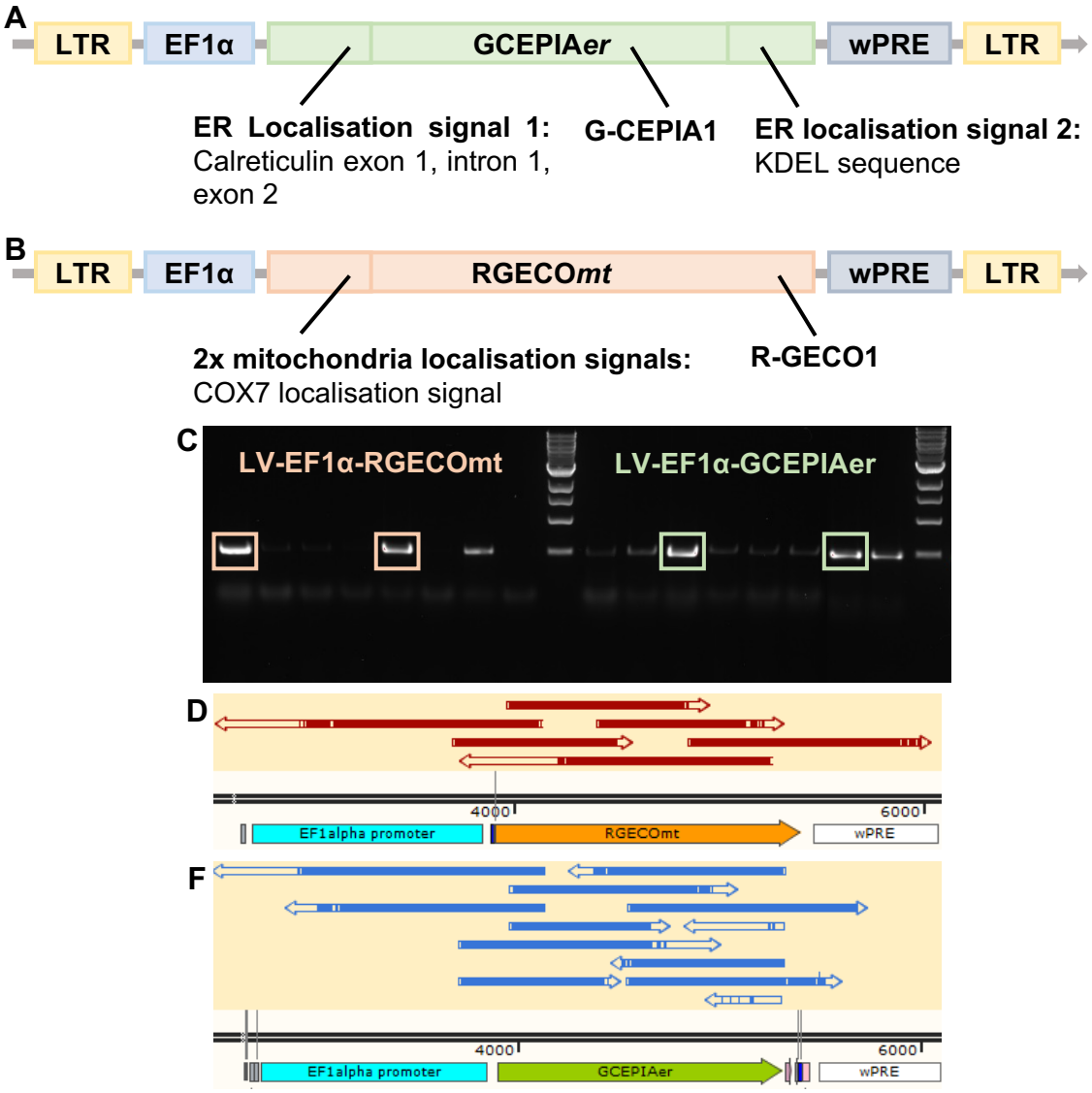


Figure 3.3: Cloning of GECIs into a lentiviral backbone

(A-B) Depictions of LV-EF1α-GCEPIAer and LV-EF1α-RGECO1mt maps. **(C)** cPCR-positive clones. **(D-F)** Sequencing-positive clones; the red and blue arrows show the areas where the sequencing data aligned to the *in silico*-generated construct.

screening using cPCR. Two cPCR-positive colonies underwent further screening via sequencing (see Figure 3.3. The methods are described in Section 2.3.

3.4 Expression and photostability of GCEPIA*er* and RGECO*mt* in DAn

Figure 3.4 shows the expression of GCEPIA*er* and RGECO*mt* in live DAn cultures. Figure 3.4 C Shows representative images of a staining of the transduced cultures with calnexin (ER marker) and TOM20 (mitochondrial marker).

To evaluate the effect of photobleaching and vehicle injection on GCEPIA*er* and RGECO*mt* in DAn cultures, cells were transduced and recorded when injected with the vehicle (HBSS + DMSO) only. The two are adequately photostable as minimal bleaching was observed, mostly at the end of the recording and right after the first time point (see Figure 3.5 A and C). For these reasons, the first timepoint was excluded from the trace and the calculation of F_0. This improved the stability of the trace (see Figure 3.5 B and D). Therefore, the first timepoint has been discarded from all subsequent GECI analyses in this Thesis.

The good photostability of the constructs allows us to exclude potential confounding effects of photobleaching on the collected data.

3.5 Investigation of ER Ca^{2+} dynamics in DAns harbouring mutations in the *SNCA* or *GBA* genes using a GCEPIA*er*-based assay

To elucidate the source of the Ca^{2+} deficit, I employed the ER entrapped intensiometric GECI, GCEPIA*er*. The transduced DAn cultures were imaged using an

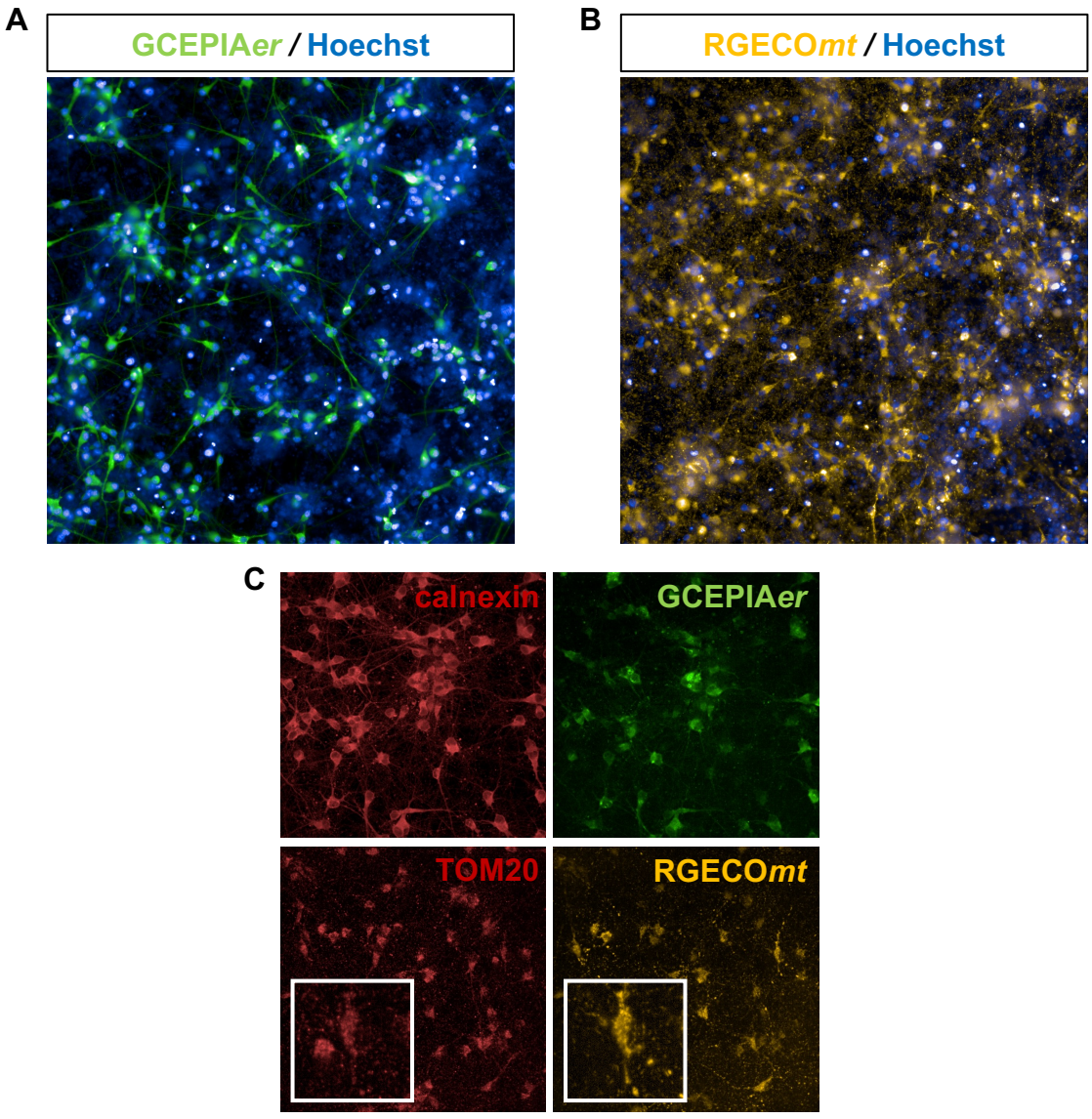


Figure 3.4: Expression of GCEPIA*er* and RGECO*mt* in DAn cultures

Representative images of **(A)** GCEPIA*er*-expressing DAn cultures and **(B)** RGECO*mt*-expressing DAn cultures. **(C)** Staining of the transduced cultures with calnexin (ER marker) and TOM20 (mitochondrial marker).

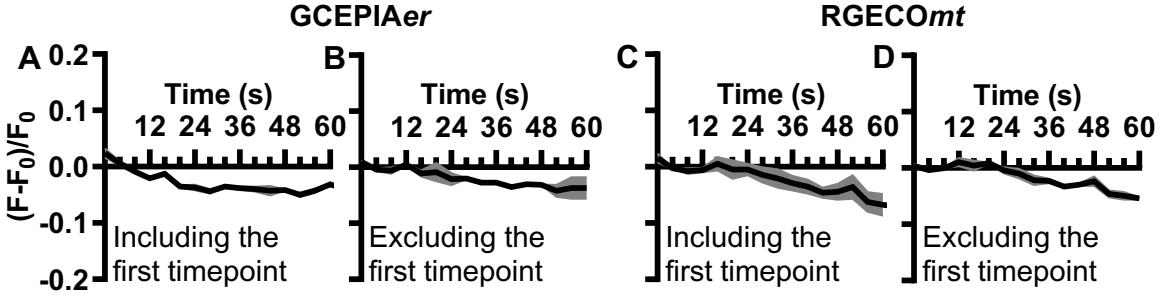


Figure 3.5: Photostability of GCEPIA*er* and RGECO*mt* in DAn cultures

(A-B) Trace of GCEPIA*er*-expressing cells only treated with vehicle, obtained including the first timepoint of the baseline or excluding it. **(C-D)** Trace of RGECO*mt*-expressing cells only treated with vehicle, obtained including the first timepoint of the baseline or excluding it.

INCELL 6000 imager (GE). Ionomycin (5 μM) was applied to the cells to increase membrane permeability to Ca^{2+}; the application of ionomycin induces a decrease in the GCEPIA*er* signal due to permeabilisation of the ER membrane to Ca^{2+} (Figure 3.6 A), therefore the response can be interpreted as a measure of the Ca^{2+} content of the ER.

DAn cultures derived from patients carrying the *SNCA*-Trp mutation were probed and the average Ca^{2+} traces of controls and patients are shown in Figure 3.6 C. The mutated cells showed decreased Ca^{2+} release upon ionomycin stimulation (Figure 3.6 D). This suggests that mutated cells display decreased Ca^{2+} concentration in their Ca^{2+} stores, possibly due to alterations in Ca^{2+} homeostasis.

DAn cultures derived from patients carrying the *SNCA-A53T* mutation and the *SNCA*-KO clones appear not to have any difference in ER Ca^{2+} handling compared to their controls (Figure 3.6 E-H).

DAn cultures derived from patients carrying the *GBA-N370S* mutation were probed and the average Ca^{2+} traces of controls and patients are shown in Figure 3.7 C. Patient cells display decreased Ca^{2+} release upon ionomycin stimulation (Figure 3.7 D). This suggests that mutated cells display decreased Ca^{2+} concentration in their Ca^{2+} stores, which may be due to alterations in Ca^{2+} homeostasis.

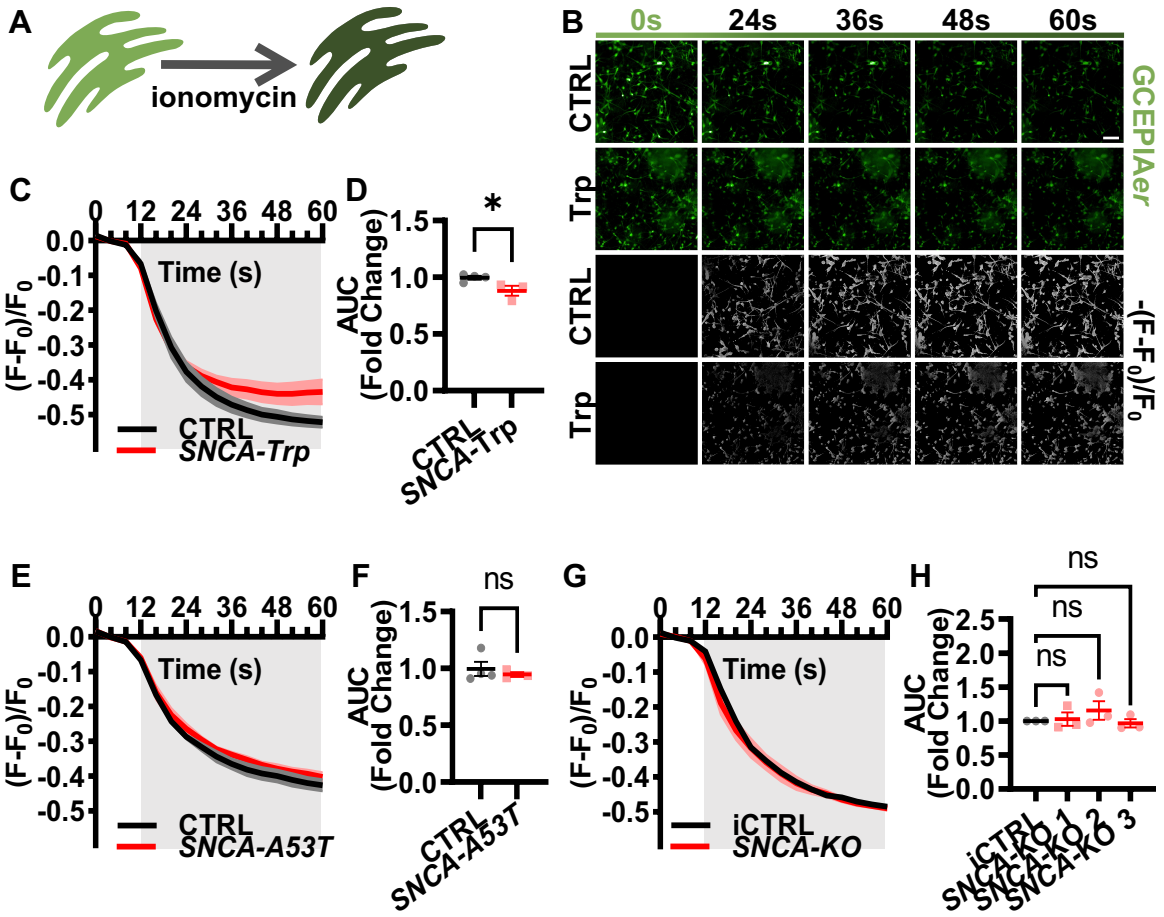


Figure 3.6: *SNCA*-Trp DAn cultures display decreased ER Ca^{2+} levels upon ionomycin stimulation in a GCEPIA*er*-based assay

(A) Cartoon showing the effect of ionomycin on GCEPIA*er* fluorescence; ionomycin permeabilises intracellular membranes causing Ca^{2+} to flow out of the ER which in turn causes a decrease in GCEPIA*er* emission intensity. **(B)** Representative images showing the change in GCEPIA*er* emission intensity in response to ionomycin over time, in both controls and *SNCA*-Trp DAns. The image also shows a rendering of the computation of $(F - F_0)/F_0$ in the same images. The image shows that the decrease in GCEPIA*er* emission intensity is smaller in the *SNCA*-Trp patient cells. **(C)** Trace showing the average of the GCEPIA*er* $(F - F_0)/F_0$ in response to ionomycin (grey box) in controls (4 lines) and *SNCA*-Trp (3 clones of 1 line). **(D)** AUC of the GCEPIA*er* $(F - F_0)/F_0$ trace in *SNCA*-Trp. Each data point represents an individual line averaged across 5 independent differentiations. Comparison between genotypes: one-tailed Mann-Whitney test. $*$ = p < 0.05. **(E)** Trace showing the average of the GCEPIA*er* $(F - F_0)/F_0$ in response to ionomycin (grey box) in controls (4 lines) and *SNCA-A53T* (3 lines). **(F)** AUC of the GCEPIA*er* $(F - F_0)/F_0$ trace in *SNCA-A53T*. Each data point represents an individual line averaged across 4 independent differentiations. Comparison between genotypes: one-tailed Mann-Whitney test. $*$ = p < 0.05. **(G)** Trace showing the average of the GCEPIA*er* $(F - F_0)/F_0$ ratio in response to ionomycin (grey box) in *SNCA*-KO (3 clones of 1 line) and their isogenic control (iCTRL). **(H)** AUC of the GCEPIA*er* $(F - F_0)/F_0$ trace in *SNCA*-KO. Each data point represents an individual differentiation. Comparison between genotypes: Friedman test. $*$ = p < 0.05.

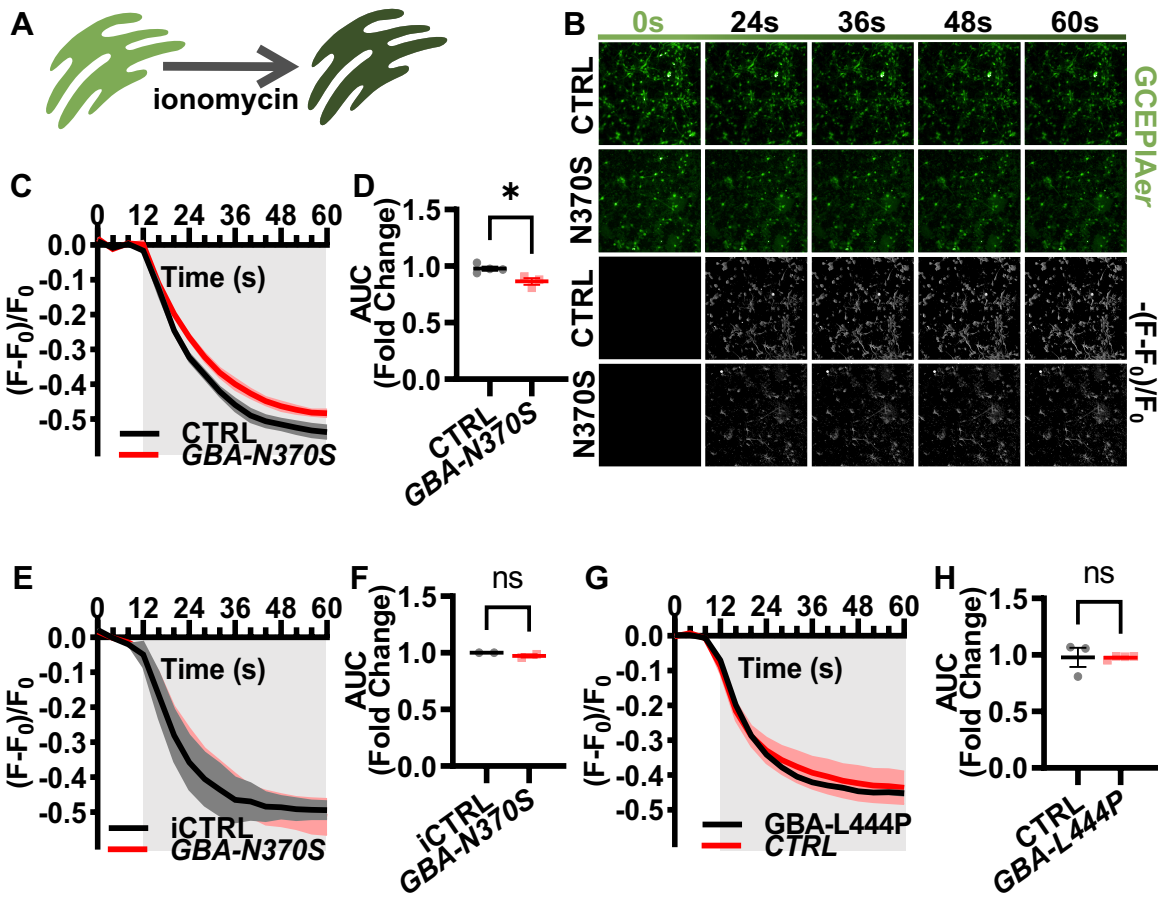


Figure 3.7: *GBA-N370S* DAn cultures display decreased ER Ca^{2+} levels upon ionomycin stimulation in a GCEPIA*er*-based assay

(A) Depiction of the effect of ionomycin on GCEPIA*er* fluorescence; ionomycin permeabilises intracellular membranes causing Ca^{2+} to flow out of the ER which in turn causes a decrease in GCEPIA*er* emission intensity. **(B)** Representative images showing the change in GCEPIA*er* emission intensity in response to ionomycin over time, in both controls and *GBA-N370S* DAns. The image also shows a rendering of the computation of $(F - F_0)/F_0$ in the same images. The image shows that the decrease in GCEPIA*er* emission intensity is smaller in the *GBA-N370S* patient cells. **(C)** Trace showing the average of the GCEPIA*er* $(F - F_0)/F_0$ in response to ionomycin (grey box) in controls (4 lines) and *GBA-N370S* (3 lines). **(D)** AUC of the GCEPIA*er* $(F - F_0)/F_0$ trace in *GBA-N370S*. Each data point represents an individual line averaged across 5 independent differentiations. Comparison between genotypes: one-tailed Mann-Whitney test. $*$ = p < 0.05. **(E)** Trace showing the average of the GCEPIA*er* $(F - F_0)/F_0$ in response to ionomycin (grey box) in *GBA-N370S* (1 line) and its WT isogenic control (iCTRL). **(F)** AUC of the GCEPIA*er* $(F - F_0)/F_0$ trace in *GBA-N370S*. Each data point represents an individual differentiation. Comparison between genotypes: one-tailed Mann-Whitney test. $*$ = p < 0.05. **(G)** Trace showing the average of the GCEPIA*er* $(F - F_0)/F_0$ ratio in response to ionomycin (grey box) in controls (3 lines) and *GBA-L444P* (4 lines). **(H)** AUC of the GCEPIA*er* $(F - F_0)/F_0$ trace in *GBA-L444P*. Each data point represents an individual line averaged across 3 independent differentiations. Comparison between genotypes: one-tailed Mann-Whitney test. $*$ = p < 0.05.

We also measured Ca^{2+} content in a patient carrying the *GBA-N370S* mutation and its isogenic control. However, no significant Ca^{2+} content difference is observed (Figure 3.7 E-F). This suggests that the *GBA* mutation may not directly cause the Ca^{2+} phenotype, and that other genetic risk factors are involved in the development of a Ca^{2+} content phenotype.

DAn cultures derived from patients carrying the *GBA-L444P* mutation also appear to not have any difference in ER Ca^{2+} handling compared to their controls (Figure 3.7 G-H).

Considering the very small N numbers in this study, it is possible that some of the datasets might be underpowered, thus masking potential differences between genotypes.

3.6 Investigation of mitochondrial Ca^{2+} dynamics in DAns harbouring mutations in the *SNCA* or *GBA* genes using a RGECO*mt*-based assay

Mitochondrial Ca^{2+} dynamics were studied using the entrapped intensiometric GECI, RGECO*mt*. The transduced DAn cultures were imaged using a INCELL 6000 imager (GE). Ionomycin (5 μM) was applied to the cells to increase membrane permeability to Ca^{2+}; the application of ionomycin induces an increase in the RGECO*mt* signal due to Ca^{2+} uptake into the mitochondria in response to increased cytoplasmic Ca^{2+} (Figure 3.6 A).

DAn cultures derived from patients carrying the *SNCA*-Trp mutation were probed and the average Ca^{2+} traces of controls and patients are shown in Figure 3.6 C. The patient-derived cells showed decreased Ca^{2+} uptake into mitochondria upon ionomycin stimulation (Figure 3.6 D). This suggests that mutated cells display dys-

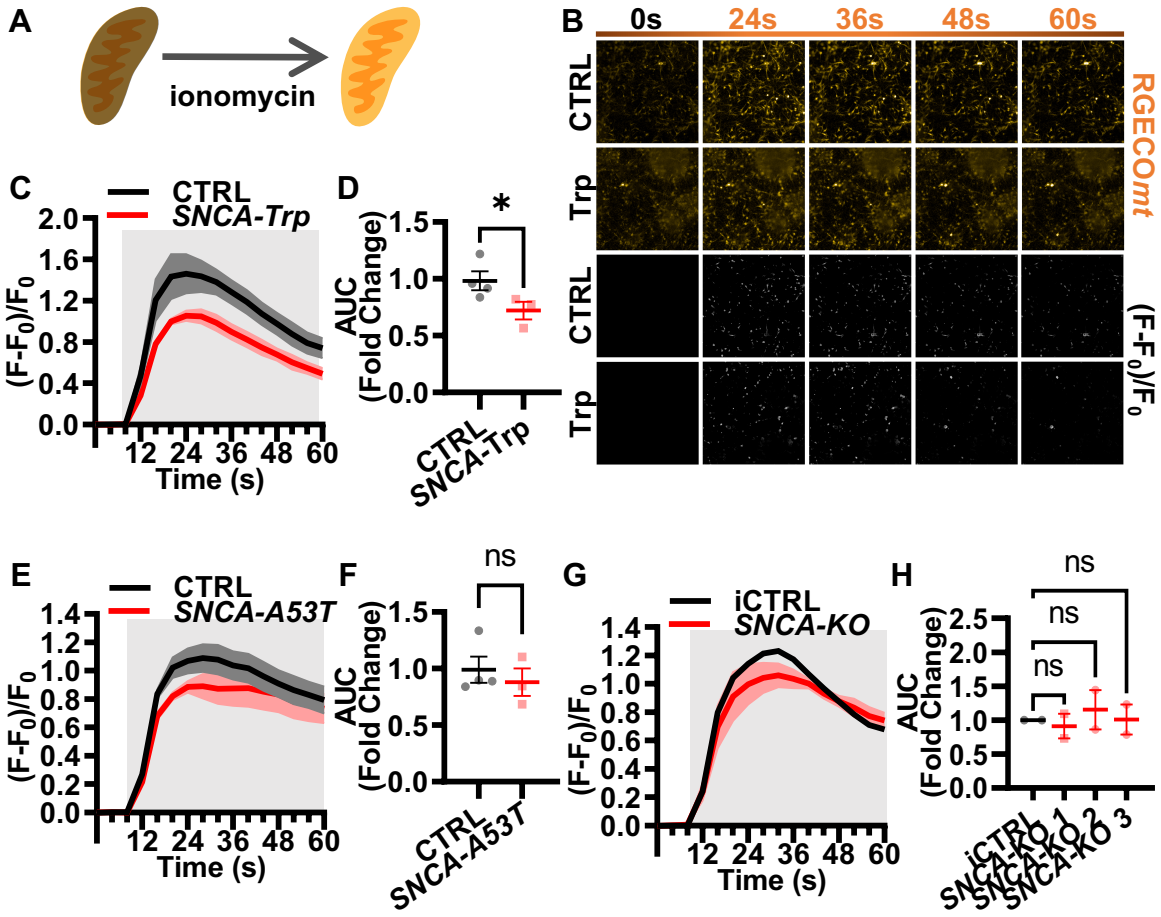


Figure 3.8: *SNCA*-Trp DAn cultures display decreased Ca^{2+} uptake into mitochondria upon ionomycin stimulation in a RGECO*mt*-based assay

(A) Cartoon showing the effect of ionomycin on RGECO*mt* fluorescence; ionomycin permeabilises intracellular and increases intracellular Ca^{2+} which is uptaken by the mitochondrial, therefore causing an increase in RGECO*mt* emission intensity. **(B)** Representative images showing the change in RGECO*mt* emission intensity in response to ionomycin over time, in both controls and *SNCA*-Trp DAns. The image also shows a rendering of the computation of $(F - F_0)/F_0$ in the same images. The image shows that the increase in RGECO*mt* emission intensity is smaller in the *SNCA*-Trp patient cells. **(C)** Trace showing the average of the RGECO*mt* $(F - F_0)/F_0$ in response to ionomycin (grey box) in controls (4 lines) and *SNCA*-Trp (3 clones of 1 line). **(D)** AUC of the RGECO*mt* $(F - F_0)/F_0$ trace in *SNCA*-Trp. Each data point represents an individual line averaged across 3 independent differentiations. Comparison between genotypes: one-tailed Mann-Whitney test. $*$ = p < 0.05. **(E)** Trace showing the average of the RGECO*mt* $(F - F_0)/F_0$ in response to ionomycin (grey box) in controls (4 lines) and *SNCA-A53T* (3 lines). **(F)** AUC of the RGECO*mt* $(F - F_0)/F_0$ trace in *SNCA-A53T*. Each data point represents an individual line averaged across 3 independent differentiations. Comparison between genotypes: one-tailed Mann-Whitney test. $*$ = p < 0.05. **(G)** Trace showing the average of the RGECO*mt* $(F - F_0)/F_0$ ratio in response to ionomycin (grey box) in *SNCA*-KO (3 clones of 1 line) and their isogenic control (iCTRL). **(H)** AUC of the RGECO*mt* $(F - F_0)/F_0$ trace in *SNCA*-KO. Each data point represents an individual differentiation. Comparison between genotypes: Friedman test. $*$ = p < 0.05.

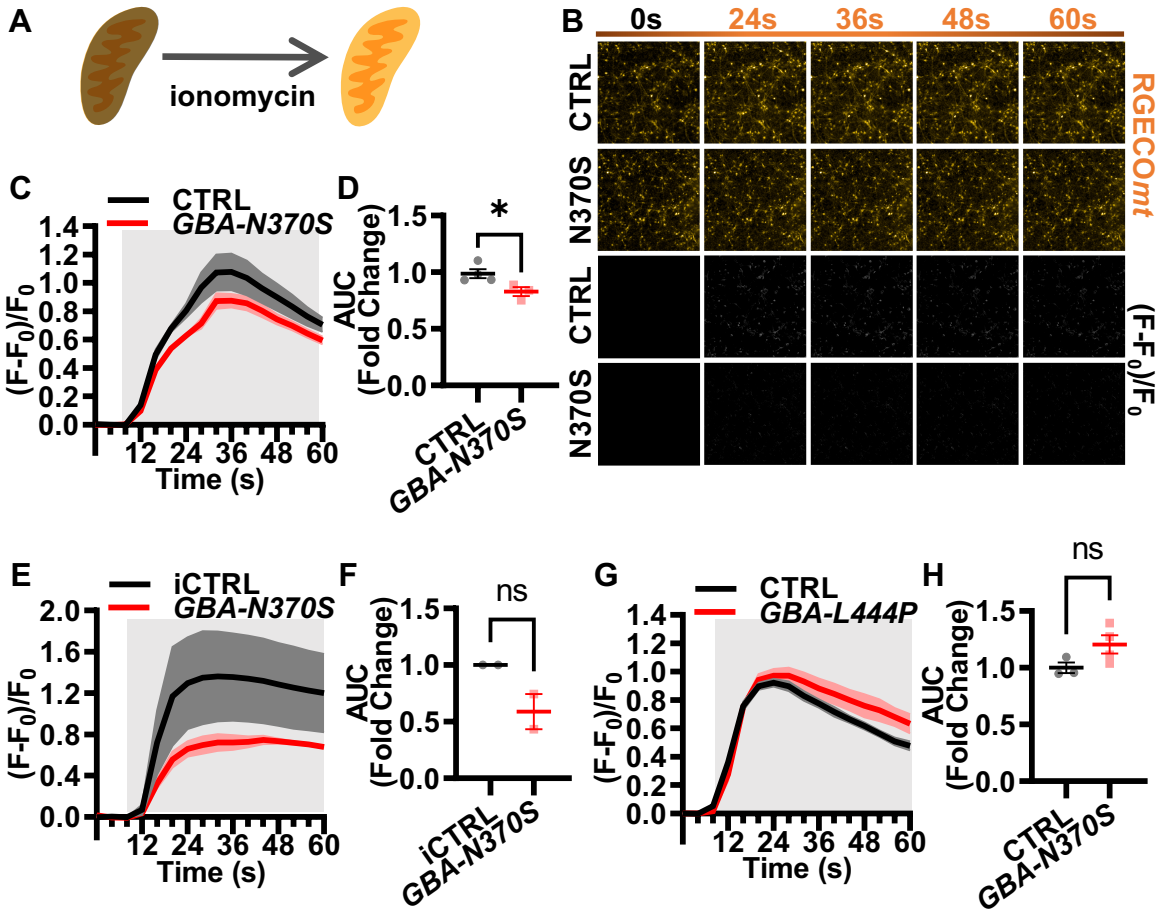


Figure 3.9: *GBA-N370S* DAn cultures display decreased Ca^{2+} uptake into mitochondria upon ionomycin stimulation in a RGECO*mt*-based assay

(A) Depiction of the effect of ionomycin on RGECO*mt* fluorescence; ionomycin permeabilises intracellular membrane to Ca^{2+} and increases intracellular Ca^{2+} which is uptaken by mitochondria, therefore causing an increase in RGECO*mt* emission intensity. **(B)** Representative images showing the change in RGECO*mt* emission intensity in response to ionomycin over time, in both controls and *GBA-N370S* DAns. The image also shows a rendering of the computation of $(F - F_0)/F_0$ in the same images. The image shows that the increase in RGECO*mt* emission intensity is smaller in the *GBA-N370S* patient cells. **(C)** Trace showing the average of the RGECO*mt* $(F - F_0)/F_0$ in response to ionomycin (grey box) in controls (4 lines) and *GBA-N370S* (3 lines). **(D)** AUC of the RGECO*mt* $(F - F_0)/F_0$ trace in *GBA-N370S*. Each data point represents an individual line averaged across 5 independent differentiations. Comparison between genotypes: one-tailed Mann-Whitney test. $*$ = p $<$ 0.05. **(E)** Trace showing the average of the RGECO*mt* $(F - F_0)/F_0$ in response to ionomycin (grey box) in response to ionomycin (grey box) in *GBA-N370S* (1 line) and its WT isogenic control (iCTRL). **(F)** AUC of the RGECO*mt* $(F - F_0)/F_0$ trace in *GBA-N370S*. Each data point represents an individual differentiation. Comparison between genotypes: one-tailed Mann-Whitney test. $*$ = p $<$ 0.05. **(G)** Trace showing the average of the RGECO*mt* $(F - F_0)/F_0$ ratio in response to ionomycin (grey box) in controls (3 lines) and *GBA-L444P* (4 lines). **(H)** AUC of the RGECO*mt* $(F - F_0)/F_0$ trace in *GBA-L444P*. Each data point represents an individual line averaged across 3 independent differentiations. Comparison between genotypes: one-tailed Mann-Whitney test. $*$ = p $<$ 0.05.

functional Ca^{2+} dynamics.

DAn cultures derived from patients carrying the *SNCA-A53T* mutation and the *SNCA*-KO clones do not display any significant decrease in mitochondrial Ca^{2+} handling compared to their controls (Figure 3.6 E-H).

DAn cultures derived from patients carrying the *GBA-N370S* mutation were also studied; the average Ca^{2+} traces of controls and patients are shown in Figure 3.9 C. The patient-derived cells display decreased Ca^{2+} uptake into mitochondria upon ionomycin stimulation (Figure 3.7 D). This suggests that mutated cells display dysfunctional Ca^{2+} dynamics.

We also measured Ca^{2+} content in a patient carrying the *GBA-N370S* mutation and its isogenic control. However, no significant Ca^{2+} content difference was observed (Figure 3.7 E-F). This suggests that the *GBA* mutation may not directly cause a Ca^{2+} phenotype, and that other risk factors in the development of a Ca^{2+} content phenotype.

DAn cultures derived from patients carrying the *GBA-L444P* mutation also appear not to have any difference in mitochondrial Ca^{2+} handling compared to controls (Figure 3.7 G-H).

Considering the very small N numbers in this study, it is possible that some of the datasets might be underpowered, thus masking potential differences between genotypes.

3.7 Single-cell distribution of the Ca^{2+} response in DAn

Different differentiation protocols produce variable percentages of TH^+ (see Section 1.4.2); besides TH^+ neurons, other neurons and other cell types are derived therefore these cultures never purely consist of DAns. One may wonder whether

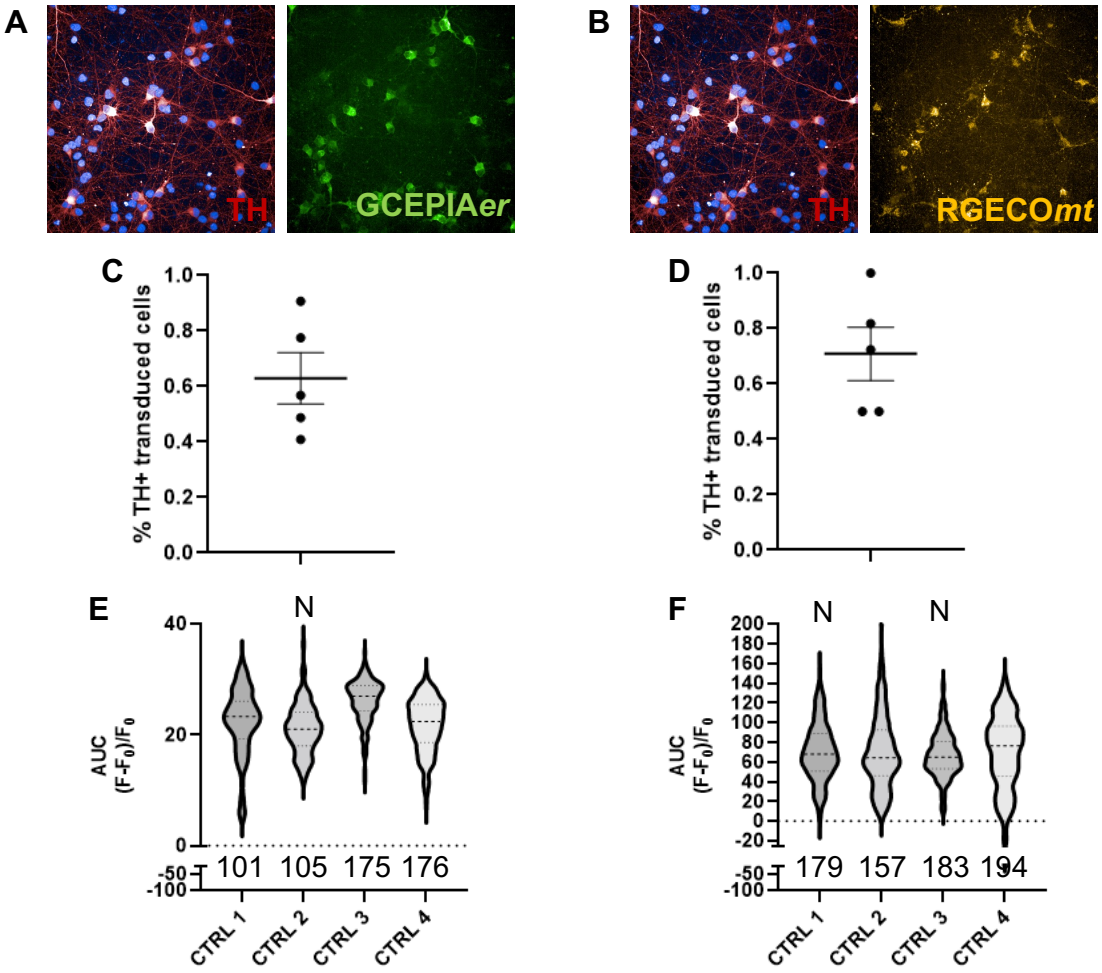


Figure 3.10: TH^+ percentage of transduced cells and single-cell distribution of the Ca^{2+} response in DAns

Example images of cells transduced with LV-EF1α-GCEPIAer **(A)** or LV-EF1α-RGECO1mt **(B)** and stained with a TH antibody. Percentage of TH^+ cells in the population of cells transduced with LV-EF1α-GCEPIAer **(C)** or LV-EF1α-RGECO1mt **(D)**. **(E)** Single cell distribution of ER Ca^{2+} release in response to ionomycin in our cultures. The data are derived from a single differentiation and a single randomly selected technical replicate per line in order to highlight cell-to-cell differences and avoid any potential effect of well-to-well variability. **(F)** Single cell distribution of mitochondrial Ca^{2+} uptake in response to ionomycin in our cultures. The data are derived from a single differentiation and a single randomly selected technical replicate per line in order to highlight cell-to-cell differences. Normality test: Kolmogorov-Smirnov test. N = passed normality test.

the Ca^{2+} handling defect is specific to TH^{+} neurons or shared with other neurons and/or cell types.

In addition, the two GECI constructs – LV-EF1α-GCEPIAer and LV-EF1α-RGECO1mt – use the EF1α promoter. This promoter is a strong promoter but does not confer any cell-type specificity. Over the years, it has become clear that DAns appear to be particularly difficult to transduce with traditional lentiviral transduction systems. While I can exclude some non-neuronal cells from the analysis based on their morphology as described in Section 2.4.2, it is not possible to exclude other neuronal cell types with simple filtering methods. Therefore, it is important to assess whether the GECIs are able to reliably report Ca^{2+} handling in dopaminergic neurons, and, if so, whether there might be any differences between the different cell types in the dish.

In order to assess how efficiently GECIs can transduce DAns, the cells were incubated with lentiviral particles and fixed and stained for TH. It is then possible to measure what percentage of the transduced cells population is positive for TH. As shown in Figure 3.10 A-D, the two constructs are successfully expressed in TH+ neurons with around over 60% of the transduced cells showing a strong TH staining.

Since in this system Ca^{2+} is imaged from different neuronal cell types as well as the DAns of interest, I thought it interesting to observe the distribution of Ca^{2+} responses in different lines to try and give a first preliminary assessment of the homogeneity of the responses of the different neuronal cell types. Figure 3.10 E-F shows the distribution of the Ca^{2+} response to ionomycin in four control lines. The data were derived from a single differentiation and a technical replicate was randomly selected to highlight the variability due to the different cell identities. Using the Kolmogorov-Smirnov test, the normality of the distributions was assessed. As shown in Figure 3.10 E-F some lines appear to be normally distributed, while

others do not. Therefore, at moment it is not possible to exclude that cells with different lineages might show different behaviour.

3.8 Dose-response of Ca^{2+} channel modulators in DAns

In order to evaluate the concentration of Ca^{2+} channel modulators to elicit Ca^{2+} responses in DAns, a dose-response curve to the Ca^{2+} channel modulators was established using the Fura-2 AM assay. In order to evaluate the potential toxicity of the Ca^{2+} channel modulators at different concentrations, the cell-culture medium was collected a ToxiLight assay was run. Establishing a dose-response of a modulator allows us to highlight the pharmacokinetics of the modulator in cell culture. When the dose-response curve reaches an asymptote, it is possible to measure the half-maximal effective concentration. However, in this analysis asymptotic behaviour was not reached for most drugs, therefore for the following assessments, a non-toxic concentration in the linear range of the curve was employed.

For the dose-response analysis, curves were interpolated using a non-linear fit.

Two SERCA pump inhibitors – i.e. cyclopiazonic acid (CPA) and thapsigargin –, two RyR positive modulators – i.e. chlorocresol and caffeine – (shown in Figure 3.11) and one IP3R positive modulator – i.e. carbachol – (not shown).

The SERCA pump inhibitor thapsigargin showed toxicity in the active concentrations and was therefore excluded from further investigations.

The active concentrations for CPA, chlorocresol and caffeine are quite high, however, qPCR and scRNA-seq data (see Figure 3.12) show that the channels are expressed in the cells, therefore I believe that the effect is on target.

Carbachol did not elicit any response even at 10 mM. Carbachol does not directly activate IP3R but rather activates a cascade signal that increases IP3 con-

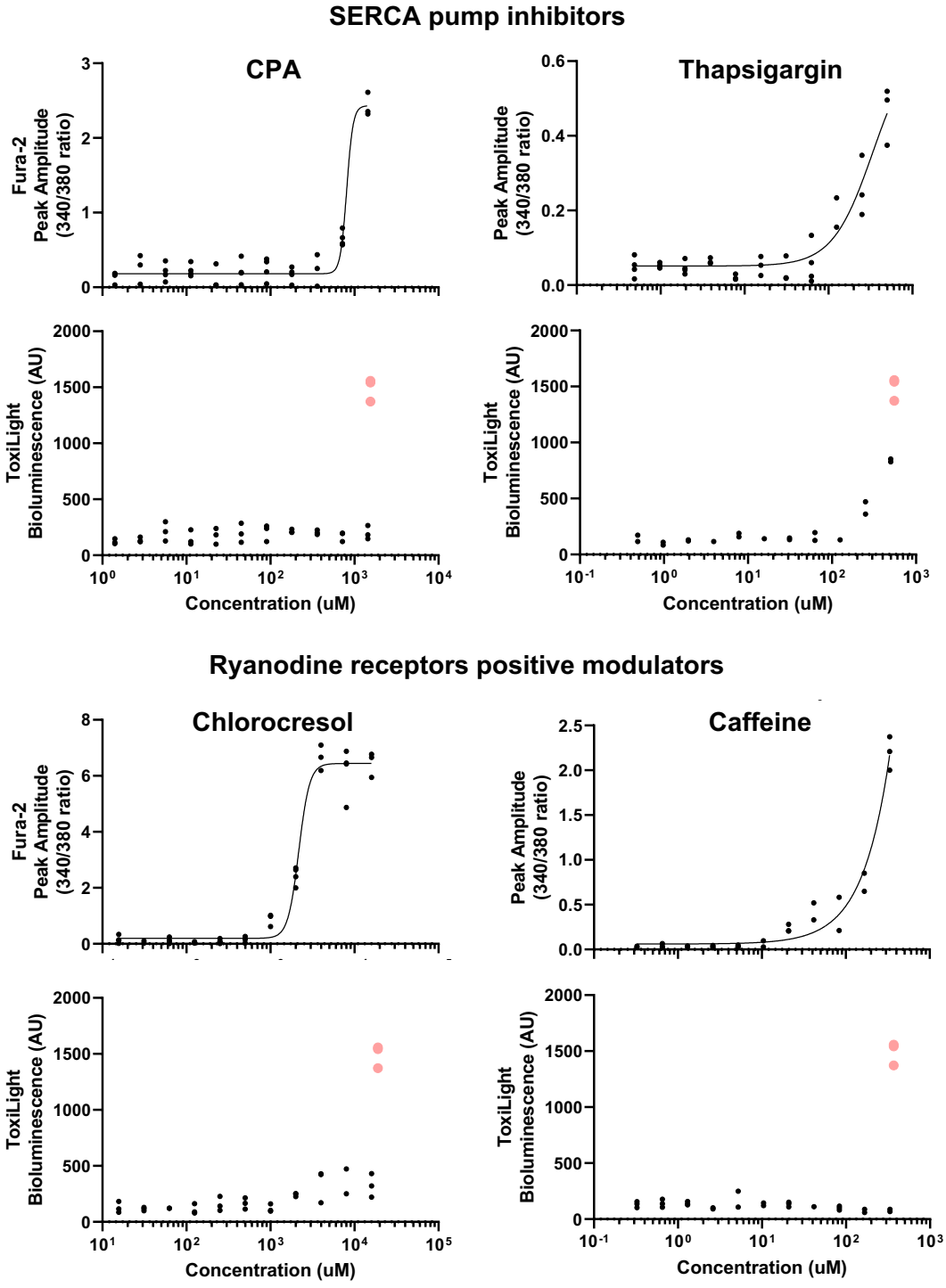
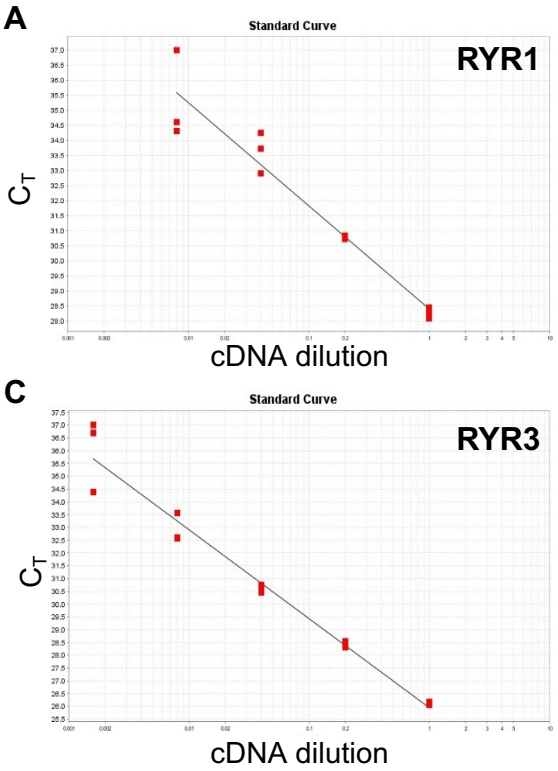


Figure 3.11: Dose-response of Ca^{2+} channel modulators in DAns

Fura-2 AM response to the drug was used to measure the potency of the drug in DAns and ToxiLight response to the drug to evaluate its toxicity.



D

GENE	Expression level (TPM)
SERCA1	80.906
SERCA2	205.828

Figure 3.12: Confirmation of expression of SERCA pumps and RyR

(A-C) qPCR data confirming expression of RyR-encoding genes in iPSC-derived DAn cultures. **(D)** scRNA-seq data confirming expression of SERCA pump-encoding genes in iPSC-derived DAn cultures.

centration in the cytoplasm. Carbachol is a cholinergic agonist, therefore it can bind and activate muscarinic receptors, which are G_q protein-coupled receptors which can in turn activate phospholipase C and increase IP3 levels in the cell. However, our iPSC-derived DAns express very low levels of muscarinic receptors (TPM = 38.287147, data courtesy of Dr Charmaine Lang obtained from the scRNA-seq experiment published in [Lang et al., 2019]), which could explain the lack of response to the drug. For these reasons, carbachol was excluded from further investigations.

3.9 Pharmacological dissection of the ER Ca^{2+} deficit using CPA, chlorocresol and caffeine

Ionomycin induces Ca^{2+} mobilisation by increasing membrane permeability to Ca^{2+}. Therefore, ionomycin-induced Ca^{2+} release can be used as a proxy for intracellular Ca^{2+} content. However, the non-specificity of the drug makes ionomycin alone a sub-optimal tool for mechanistic studies aimed at unveiling the source of the Ca^{2+} deficit.

For this reason, I decided to follow up on the ER Ca^{2+} deficit via a pharmacological dissection of the source of the phenotype. To this end, a number of ER Ca^{2+} modulators were tested (see Section 3.8). After the initial test, the SERCA pumps inhibitor CPA (90 μM) and the RyR positive modulators chlorocresol (500 μM) and caffeine (50 mM) were used in conjunction with GCEPIA*er* to try and obtain more insight into the origin of the phenotype.

SERCA pump inhibition via CPA stops the ER from refilling itself. Therefore, the net Ca^{2+} release from the ER observed using CPA can be interpreted as mostly due to IP3R and RyR leakage. This is a potential mechanism through which ER Ca^{2+} is decreased. However, no differences are observed between DAns derived

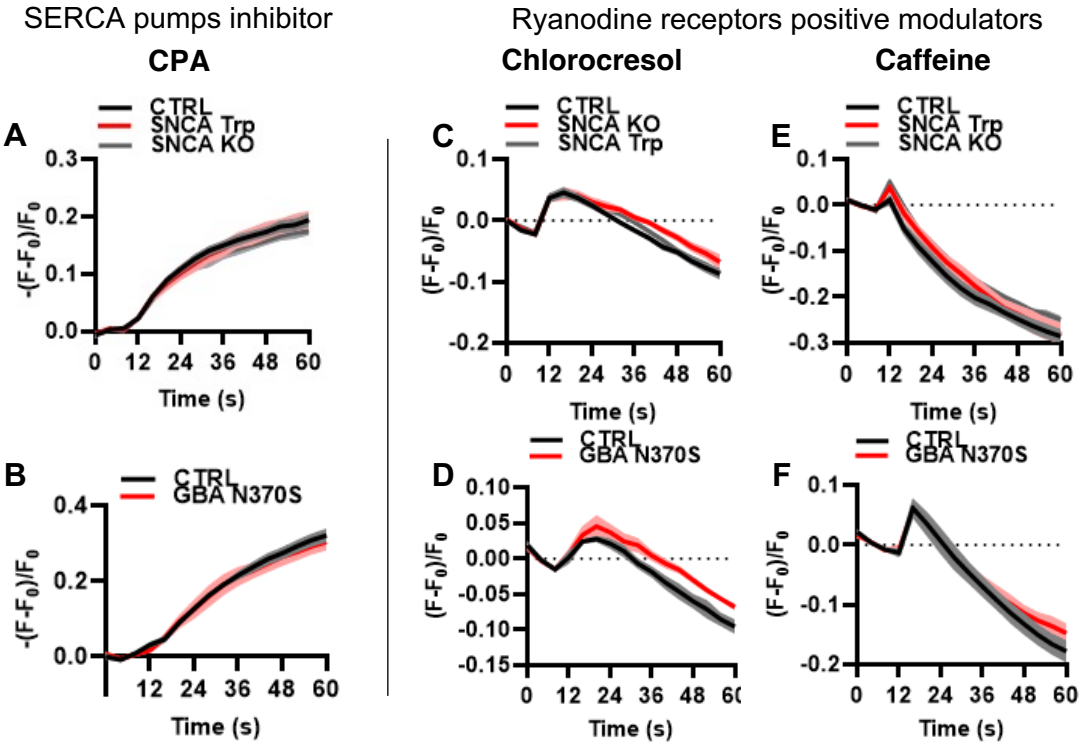


Figure 3.13: Pharmacological dissection of the ER Ca^{2+} deficit in *SNCA*-Trp and *GBA-N370S* DAns using CPA, chlorocresol and caffeine

Traces show the average of the GCEPIA*er* $(F - F_0)/F_0$ in response to ionomycin (grey box) in controls (3 lines), *SNCA*-Trp (3 clones of 1 line) *GBA-N370S* (3 lines). Data derived from 3 independent differentiations. **(A-B)** ER Ca^{2+} leakage highlighted by SERCA pump inhibition using CPA in *SNCA*-Trp and *GBA-N370S* DAns. **(C-D)** ER Ca^{2+} release induced by RyR activation via chlorocresol in *SNCA*-Trp and *GBA-N370S* DAns. **(E-F)** ER Ca^{2+} release induced by RyR activation via caffeine in *SNCA*-Trp and *GBA-N370S* DAns.

from patients carrying the *SNCA*-Trp and the *GBA-N370S* mutations compared to their controls (Figure 3.13 A-B).

It might also be possible that RyR and IP3R are hyperactive in patient-derived DAns and this might lead to ER Ca^{2+} depletion. However, DAns derived from patients carrying the *SNCA*-Trp and the *GBA-N370S* mutations do not display any significant decrease in ER Ca^{2+} release compared to their controls (Figure 3.13 C-F) upon chlorocresol and caffeine stimulation. The function of IP3R could not be probed.

3.10 Discussion

Ca^{2+} ions serve the cells in a plethora of ways including their role in synaptic transmission and as a necessary cofactor for certain enzymes and other proteins. ER and mitochondria are the main Ca^{2+} stores in the cell and several ER chaperones and mitochondrial dehydrogenases require Ca^{2+} for their function. Moreover, L-type Ca^{2+} channels support the crucial pacemaker activity of DAns. Therefore, I suspect that even small alterations in Ca^{2+} homeostasis and dynamics might be detrimental for SNpc DAns, which could explain their vulnerability.

Therefore, in this chapter I sought to study Ca^{2+} dynamics and deficits in disease-relevant human models of PD with the ultimate goal of shedding some light on the pathogenic mechanisms associated with neuronal vulnerability and death in Parkinson's.

To this end, I have employed iPSC-derived DAn cultures from controls and patients carrying mutations in the *SNCA* or *GBA* genes. This model allows us to study *in vitro* the very same neurons that degenerate in PD. In addition, neurons derived from patients will be representative of the complete genetic landscape that might have contributed to the development of the disease.

To probe Ca^{2+} dynamics, I have employed the ionophore ionomycin to release Ca^{2+} from intracellular Ca^{2+} stores in conjunction with Fura-2 AM to monitor gross changes in Ca^{2+} dynamics, GECI entrapped in the ER and the mitochondria (GCEPIA*er* and RGECO*mt* respectively) to trace back the source of the defect in DAns.

In this chapter, I show that *SNCA*-Trp, *SNCA-A53T* and *GBA-N370S* iPSC-derived DAns display decreased intracellular Ca^{2+} levels upon ionomycin stimulation in a Fura-2 AM-based assay, which suggests lower intracellular levels. This

result is supported by the finding that *SNCA*-Trp and *GBA-N370S* iPSC-derived DAn cultures release less ER Ca^{2+} in response to ionomycin in a GCEPIA*er*-based assay. The reduced Ca^{2+} levels in the ER are also accompanied by reduced Ca^{2+} uptake into the mitochondria as demonstrated in a RGECO*mt*-based assay.

These results may be explained by changes in the activity of the Ca^{2+} pumps at the membranes of ER and mitochondria. For example, recent work performed in a fruitfly model of PD showed that SERCA pump function might be impaired in PD due to high levels of carbonyl adducts to the protein [Solana-Manrique et al., 2021]. Low SERCA activity would result in an ineffective refilling of the ER. This in turn would cause higher cytoplasmic Ca^{2+} levels, but mostly decreased ER Ca^{2+} levels.

GCEPIA*er* has been used in conjunction with ionomycin, which increases the permeability of membranes to Ca^{2+} and therefore it depletes the intracellular stores by transporting ions through their membranes. Therefore, ionomycin-induced ER Ca^{2+} release can be used as a proxy for ER Ca^{2+} content. The use of ionomycin does not confer any spatial resolution or specificity of release; however the use of a GECI entrapped in the ER, provides a spatial resolution that can reassure me that the observed Ca^{2+} flux comes from the ER. Therefore, the decrease in ER Ca^{2+} levels in DAn cultures derived from PD patients can be interpreted as decreased Ca^{2+} levels in the ER of the patients. This could be due to decreased SERCA pump activity in PD patients, which could result in decreased ER Ca^{2+} levels and increased Ca^{2+} levels in the cytoplasm. In the data described in this chapter (see Figures 3.1 B, F and J and 3.2 B, F and J), I do not show any differences in baseline Ca^{2+}, which would suggest that potential differences (if any) in cytoplasmic Ca^{2+} levels could not be detected by the assay. It is possible to measure more accurately baseline cytoplasmic levels using Fura-2 AM as described [Williams and Fay, 1990] and it might be interesting to assess this in our patient lines. It would also

be interesting to measure SERCA pump activity as described in [Solana-Manrique et al., 2021]. Interestingly, a SERCA pump positive modulator has also been suggested to be a potential therapeutic target for PD [Dahl, 2017, Solana-Manrique et al., 2021].

Other Ca^{2+} channels might also be involved. A number of chemical compounds can be used to release Ca^{2+} in a channel-specific manner during Ca^{2+} imaging experiments in order to study Ca^{2+} release and dynamics within the cell. In an attempt to investigate the potential involvement of IP3R or RyR, the SERCA pump inhibitor CPA was employed to study IP3R or RyR leakage and the RyR positive regulators chlorocresol and caffeine were used. However, no changes could be detected.

iPSC-derived DAn cultures are not pure as several different neuronal cell types are also differentiated with the DAns of interest. Fura-2 AM, LV-EF1α-GCEPIA1er and LV-EF1α-RGECO1mt do not display any specificity for DAns, therefore the data collected in this chapter are representative of the contribution of all the different cells types cultured in the dish.

Therefore, it would be interesting to assess whether DAns show similar behaviour to the other neuronal cell types or if the different cell types stratify. In order to perform a preliminary assessment, I observed the single-cell distribution of the neuronal responses. As shown in Figure 3.10 E-F some lines appear to be normally distributed, while others do not. Therefore, at moment it is not possible to exclude that cells with different lineages might show different behaviour.

It could be interesting to further investigate this question, by recording the single-cell Ca^{2+} response and then performing post-hoc labelling using the TH marker to identify DAns. This way it could be possible to definitely assess whether DAns behave similarly to other neurons in the culture or whether their Ca^{2+} hand-

ling and mishandling is different.

Changes in the architecture of MAMs could also be responsible for changes in Ca^{2+}, as Ca^{2+} homeostasis is one of the main roles of these contact regions. An increasing body of evidence has shown a potential role of MAMs in cellular dysfunction in PD. More specifically, they have been suggested to be involved in the pathogenicity of α-synuclein. It has been suggested that α-synuclein might misocalise to MAMs and interfere with Ca^{2+} dynamics and homeostasis in the mitochondria [Guardia-Laguarta et al., 2013, Paillusson et al., 2017, Erustes et al., 2021]. Intriguingly, iPSC-derived DAns carrying the *SNCA*-Trp and *GBA-N370S* mutations exhibit increased α-synuclein release in the extracellular medium, suggesting a potential dysfunction of cellular α-synuclein [Fernandes et al., 2016, Zambon et al., 2019]. Therefore, it would be of extreme interest to study MAM proteins in the context of PD and Ca^{2+} dyshomeostasis.

In order to study the possible involvement of ER and mitochondrial Ca^{2+} channels and MAM proteins in Ca^{2+} homeostasis in PD patients and after the inconclusive results from the pharmacological approach, I decided to follow up with two different approaches. One revolving around the knock-down of candidate genes (Chapter 4) and another based on subcellular compartment-specific proteomics (Chapter 5).

Appendix

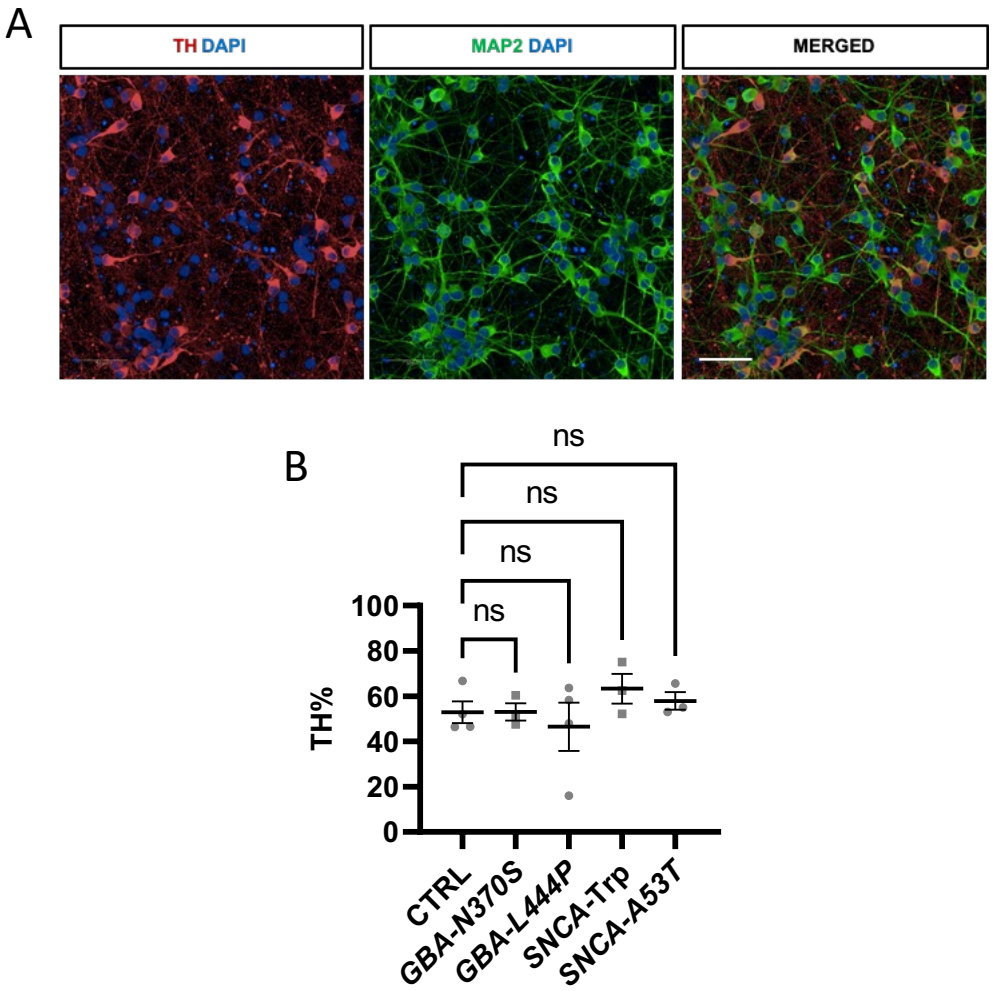


Figure 3.14: Percentage of TH+ neurons in iPSC-derived DAn cultures

(A) Representative images of DAn cultures stained for TH and MAP2 **(B)** Quantification of the percentage of TH positive neurons in the culture. Comparison between genotypes: Friedman test.

Figure 3.14 A shows a figure from a TH and MAP2 staining of a iPSC-derived DAn culture. Figure 3.14 B shows that the quantification of the percentage of TH positive neurons in the culture.

Chapter 4

CRISPRi screening of genes involved ER and mitochondrial Ca^{2+} handling

4.1 Introduction and aims

As our pharmacological attempt to elucidate the role of Ca^{2+} channels in the Ca^{2+} dysfunction observed in patient-derived DAns proved rather inconclusive, we sought to find a different approach to tackle the question.

We decided to use genetic manipulation to accomplish loss-of-function of a panel of genes encoding for proteins of interest and then assess their role in Ca^{2+} release using a Fura-2 AM-based assay.

There are a number of techniques to accomplish genetic loss-of-function, including RNAi, gene knock-out and more recently CRISPR interference (CRISPRi), which we utilised. CRISPRi comes from engineering and repurposing of the CRISPR-Cas9 nuclease (CRISPRn) technology.

Like CRISPRn, CRISPRi relies on two components, i.e. the protein Cas9 and

a sgRNA. In CRISPRn the protein Cas9 binds to and cuts DNA in a region homologous to that of the sgRNA. In CRISPRi, the Cas9 is enzymatically dead (dCas9) and no longer serves as a nuclease, and therefore it can only bind to a specific DNA sequence.

The first generation of CRISPRi only relied on the fact that the dCas9 competed with RNA polymerase causing a net decrease in transcription [Qi et al., 2013]. The second generation of CRISPRi aimed at improving the rate of knock-down by functionalising the dCas9 with the transcription repressor KRAB (see Figure 4.1) [Gilbert et al., 2013]. The recruiting of KRAB to the sequence of interest as designated by the sgRNA by the dCas9 improved greatly the efficacy of the knock-down making this technique very appealing.

In 2016, a tool to generate efficient and specific guides was generated [Horlbeck et al., 2016], subsequently making CRISPRi technology more specific than RNAi. The employment of the dCas9-KRAB fusion protein that does not rely on DNA damage for its function, made this tool more reliable and less toxic than CRISPRn. These two features make CRISPRi technology well suited for genetic screens even in fragile cell types such as iPSC-derived neurons [Kampmann, 2018].

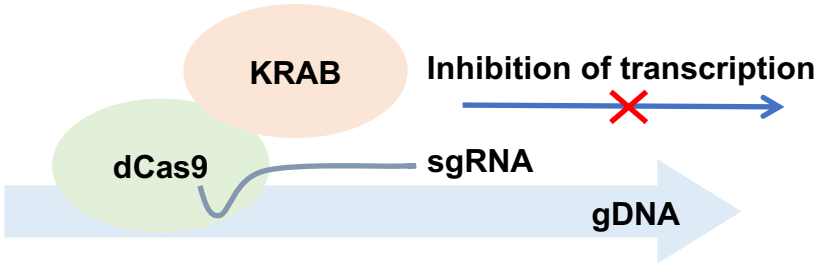


Figure 4.1: Cartoon depicting CRSPRi function
dCas9 docks the transcription repressor KRAB to the DNA region identified by the sgRNA.

Table 4.1: List of genes included in the ER and mitochondrial membrane CRISPRi panel

Gene symbol	Function	Localisation
ATP2A1 aka SERCA1	ER Ca^{2+} replenishment	ERM
ATP2A2 aka SERCA2	ER Ca^{2+} replenishment	ERM
RYR2	Ca^{2+}-induced Ca^{2+} release	ERM
RYR3	Ca^{2+}-induced Ca^{2+} release	ERM
MCU	Ca^{2+} uptake into the mitochondria (low affinity)	IMM
BCAP31 aka BAP31	Protein trafficking to the Golgi, ERAD, ER stress	MAMs / ERM
ITPR1 aka IP3R1	ER Ca^{2+} release in response to IP3	MAMs / ERM
ITPR2 aka IP3R2	ER Ca^{2+} release in response to IP3	MAMs / ERM
OSBPL5 aka ORP5	Lipid trafficking	MAMs / ERM
OSBPL8 aka ORP8	Lipid trafficking	MAMs / ERM
PACS2	ER transmembrane transporter and Ca^{2+} homeostasis	MAMs / ERM
RRBP1	Synthesis of secreted proteins	MAMs / ERM
FIS1	Mitochondrial fission	MAMs / OMM
MFN1	Mitochondrial fusion	MAMs / OMM
RMDN3 aka PTPIP51	Ca^{2+} homeostasis	MAMs / OMM
SYNJ2BP	Signal transduction	MAMs / OMM
VDAC1	Ions and small metabolites transporter	MAMs / OMM
MFN2	Mitochondrial fusion	MAMs/ OMM / ERM

ER and mitochondria play a crucial role in the Ca^{2+} homeostasis of a cell, and Ca^{2+} homeostasis is one of the main functions of MAMs. Therefore we sought to investigate the role of Ca^{2+} pumps and channels located at the ER and mitochondrial membranes, as well as several MAM-resident proteins, in Ca^{2+} homeostasis and dyshomeostasis in iPSC-derived DAns. The list of selected targets can be found in Table 4.1 and includes well-characterised Ca^{2+} channels and MAM proteins, some

of which are of particular interest in PD [Gómez-Suaga et al., 2018].

Interestingly, SERCA pumps might undergo aberrant post-transcriptional modifications that decrease their function [Solana-Manrique et al., 2021]. Moreover, it has been reported that in PD, pathologic α-synuclein might interact with the MAM protein VAPB and disrupt its interaction with PTPIP51, therefore increasing the distance between MAMs and causing a decrease in ER-mitochondrial Ca^{2+} shuttling [Paillusson et al., 2017].

Aims of the Chapter

- Generate, clone and prep a panel of sgRNA guides for the ER and mitochondrial membrane CRISPRi panel
- Perform a preliminary experiment to assess the effect of the knock-down of the genes in the CRISPRi panel on Ca^{2+} dynamics
- Generate a panel of control and patient-derived iPSC lines expressing the dCas9-KRAB machinery for future experiments in DAns

4.2 Generation of the ER and mitochondrial membrane protein CRISPRi panel

In order to study the involvement of ER and mitochondrial membrane proteins, we decided to employ a knock-down approach. The list of genes is detailed in Table 4.2. The sgRNA names are accompanied by the name of the target gene, the expression level of the transcript in iPSC-derived DAns and the sequence of the guide. The guide sequences were obtained from [Horlbeck et al., 2016].

The genes were selected based on their localisation and their involvement in Ca^{2+} handling. Wherever more than one isoform was present, the genes encoding for the highest expressed isoforms in DAns were prioritised; expression data was obtained from the scRNAseq dataset previously published in Lang *et al.* [Lang et al., 2019].

Table 4.2: List of guides included in the ER and mitochondrial membranes proteins panel

sgRNA symbol	Gene symbol	Expression level (TPM)	Sequence
ATP2A1-1	ATP2A1 aka SERCA1	80.90556585	GGGTGGCCGGCTGCTCAAGT
ATP2A1-2	ATP2A1 aka SERCA1	80.90556585	GTGTGGAGGGAAGAAAAACC
ATP2A2-1	ATP2A2 aka SERCA2	205.8282118	GGCCGCACGCCCGACAGCGG
ATP2A2-2	ATP2A2 aka SERCA2	205.8282118	GAGCGCCGCACGCCCGACAG
BCAP31-1	BCAP31 aka BAP31	1323.004432	GAGCACCTCAAGGCCCCATA
BCAP31-2	BCAP31 aka BAP31	1323.004432	GGCCCGCGAGGGCTACTGTA
FIS1-1	FIS1	1243.977998	GCACTGGGCCATGGAGACTG
FIS1-2	FIS1	1243.977998	GTGTAGTGTGAGGCTCGCGG
ITPR1-1	ITPR1 aka IP3R1	35.73030315	GCGGACATGGGATTACCCAG
ITPR1-2	ITPR1 aka IP3R1	35.73030315	GTCCCCGGGCACCAAGGTAG

ITPR2-1	ITPR2 aka IP3R2	89.8692283	GGCAGGGAGTGGACACGGAG
ITPR2-2	ITPR2 aka IP3R2	89.8692283	GCGCAGCGGGTCGCAGAGCA
MCU-1	MCU	138.0268558	GGCCGCCGCCCCGAGAGGAG
MCU-2	MCU	138.0268558	GAGCAGGAGCGATCTACCTG
MFN1-1	MFN1	107.8110922	GTGCCGGGTGATAGTTGGAG
MFN1-2	MFN1	107.8110922	GCTCCGCTCCAACTATCACC
MFN2-1	MFN2	102.6833803	GCGCGAGGCCGGGAAGGTGA
MFN2-2	MFN2	102.6833803	GTAAACAGGGCTGAACGAGA
OSBPL5-1	OSBPL5 aka ORP5	128.043705	GAAAGGAGCCGGGACCGCCA
OSBPL5-2	OSBPL5 aka ORP5	128.043705	GGAGCTCGCGGCACGGTAGG
OSBPL8-1	OSBPL8 aka ORP8	213.6917289	GCTACCGGCAGCGGCTACTG
OSBPL8-2	OSBPL8 aka ORP8	213.6917289	GCTCCCTGGGAGCTCCGCAC
PACS2-1	PACS2	320.1438396	GCCCAGGTCCCGAGCACCGG
PACS2-2	PACS2	320.1438396	GGCTTGCCGGAGCTGCGGGG
RMDN3-1	RMDN3 aka PTPIP51	161.204594	GACCCGGCCGCCAGCCACCA
RMDN3-2	RMDN3 aka PTPIP51	161.204594	GTGACAGCGTGAGCCCGCGG
RRBP1-1	RRBP1	402.7415504	GGTGCGCGCGTGTGGAGTCG
RRBP1-2	RRBP1	402.7415504	GCCCTGCCTACGCCCCGGTA
RYR2-1	RYR2		GGCGTCAGGGCATCCACTAG
RYR2-2	RYR2		GTCTGCCCGGACCCCGCTAG
RYR3-1	RYR3		GCGGCTGCCGGGGGAAGCAG
RYR3-2	RYR3		GGCAGAGGCGCCGGAGGCTG
SYNJ2BP-1	SYNJ2BP	221.83188	GGGTGAAGGTGAATCAATCT
SYNJ2BP-2	SYNJ2BP	221.83188	GCACTCCAGCTGACCCAAGT
VAPB-1	VAPB	164.8185364	GCGGGGGTCCTCTACCGGGT
VAPB-2	VAPB	164.8185364	GCTACGCGGTGCAGGCGCAG
VDAC1-1	VDAC1	893.327667	GCTCGCTCGGCTCCGCTCCC
VDAC1-2	VDAC1	893.327667	GGAGGCAGGGAGCCGAGCCA

The guides listed above were cloned in the H25-U6-sgRNA-NucBlue backbone as previously published in [Tian et al., 2019] using the method detailed in 2.3. Figure 4.2 shows the map of the expression vector and an example of a clone positive for sequencing. Guides VAPB-1, VAPB-2, ITPR1-1, ITPR1-2, ITPR2-1,

ITPR2-2, VDAC1-1, VDAC1-2, MCU-1, MCU-2, CTRL1 and CTRL1 were a gift from S. W. Humble.

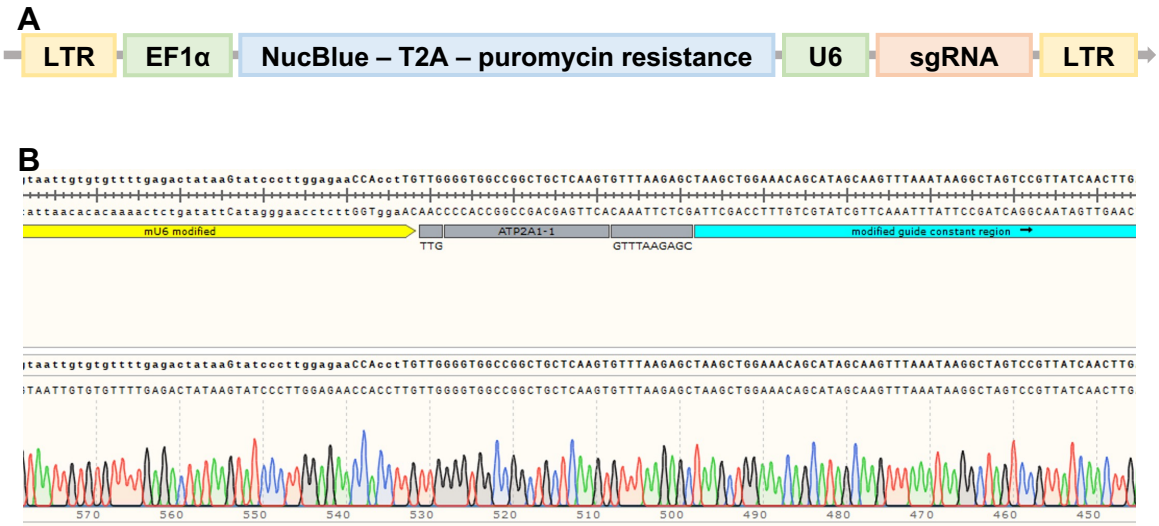


Figure 4.2: Cloning of sgRNAs into their lentiviral expression vector

(A) Cartoon of the H25-U6-sgRNA-NucBlue map. **(B)** Example of the sequencing of one of the clones positive after cloning.

4.3 Titration of the lentivirus driving the expression of the sgRNA

The cloned guides were packaged into lentiviruses in order to be delivered to neurons. Targeting and non-targeting guides were developed with the aim to compare them based on their effect on cells in phenotypic-based assays. In order to avoid differences that might have arisen from the application of different amounts of virus, a functional titration of the virus was performed, with the goal to deliver a similar number of infectious lentiviruses to the cells. This titration takes advantage of the NucBlue tag (NLS-mTag2BPF); cells are infected with increasing volumes of virus, the (# infected cells)/(total # of cells) ratio is measured and the volume that is required to obtain 65% of infection (i.e. (# infected cells)/(total # of cells) ratio = 0.65)

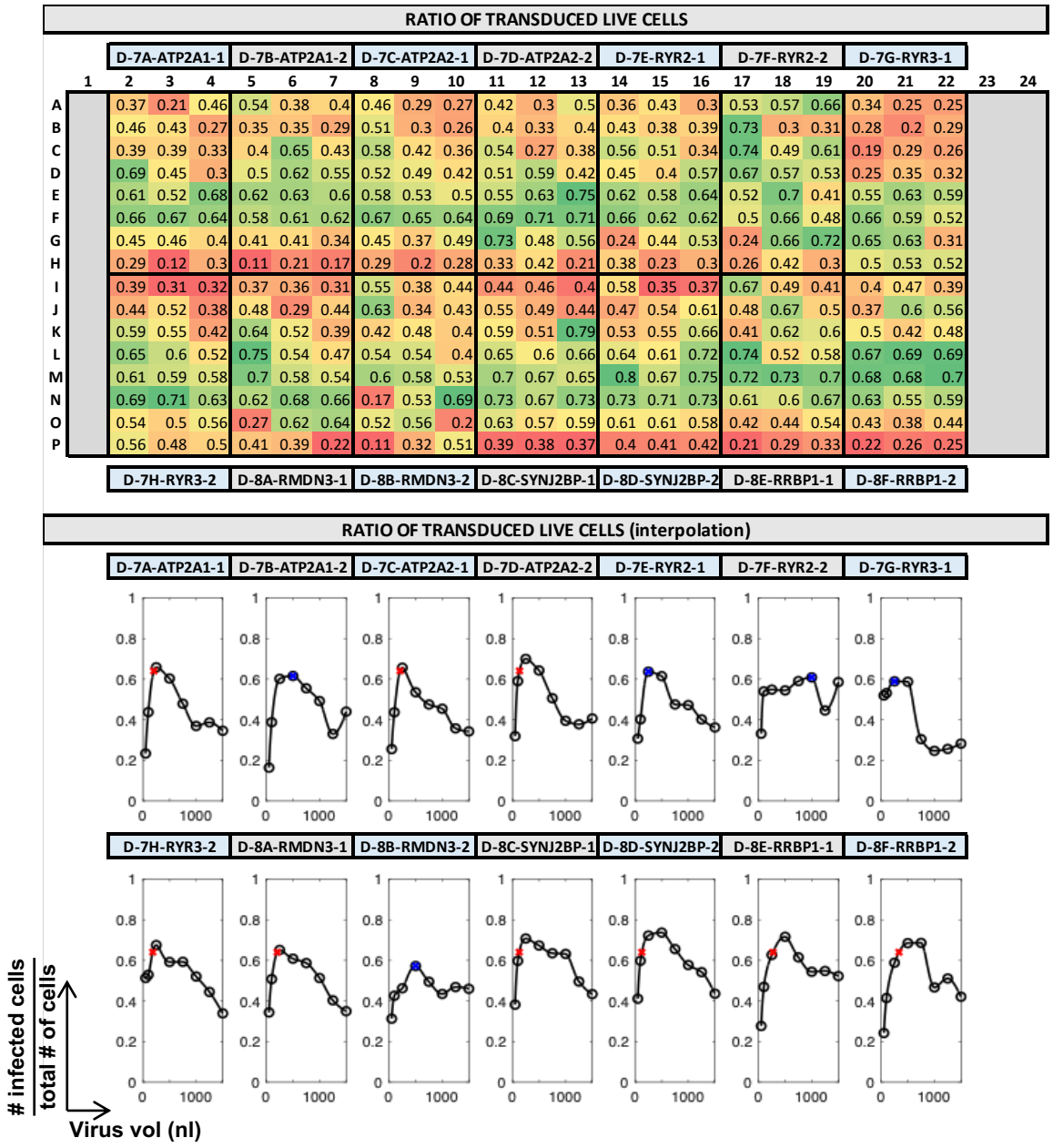


Figure 4.3: Titration of the lentiviruses for the expression of sgRNA (batch #1)

Well average of the ratio of transduced cells. Interpolation of the (# infected cells)/(total # of cells) ratio as a function of the volume of virus added (nl). The red Xs indicate the point corresponding to 65% of transduced cells. Whenever this percentage was not reached, the volume corresponding to the highest transduction rate was chosen as highlighted by the blue Xs.

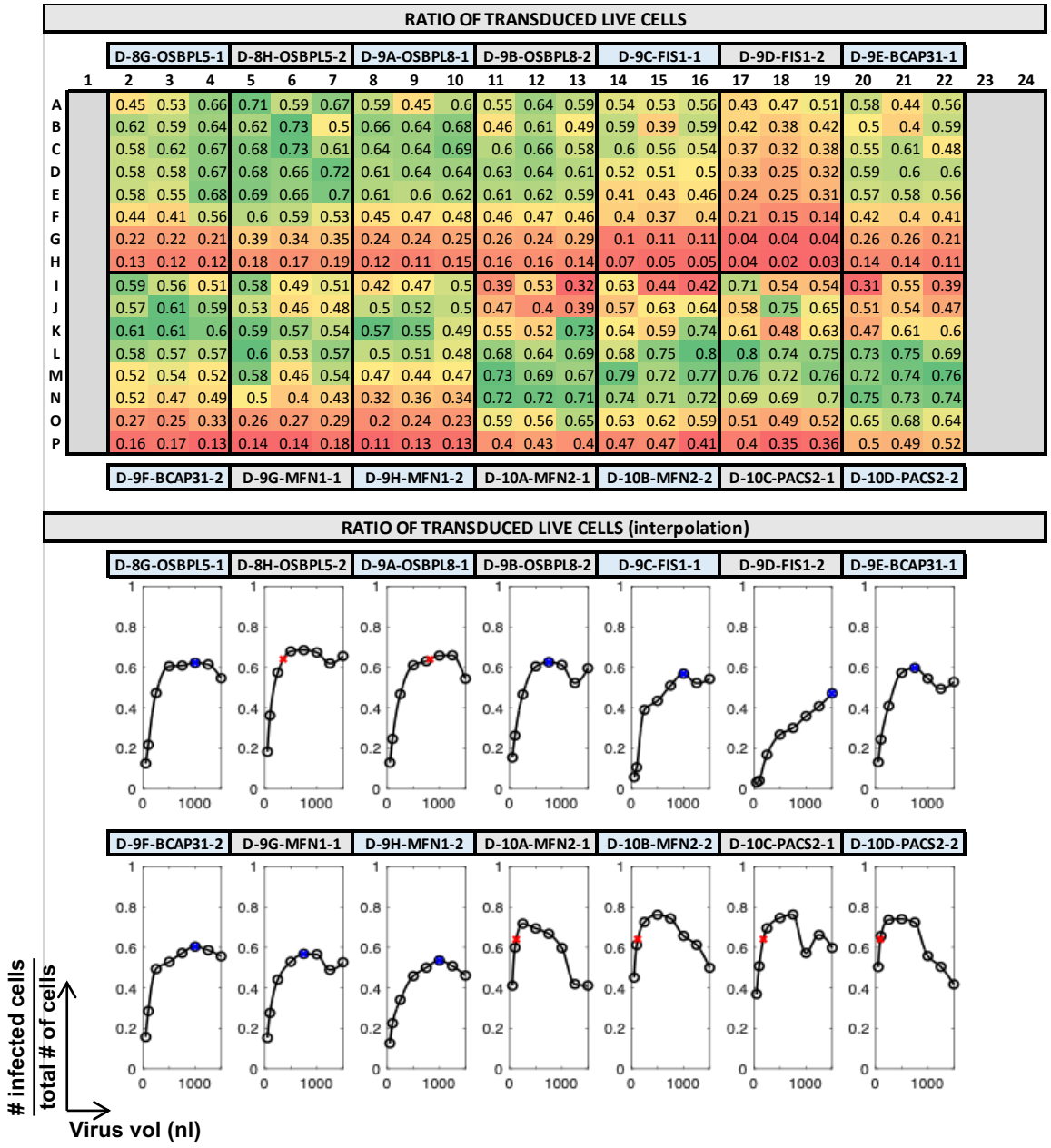


Figure 4.4: Titration of the lentiviruses for the expression of sgRNA (batch #2)

Well average of the ratio of transduced cells. Interpolation of the (# infected cells)/(total # of cells) ratio as a function of the volume of virus added (nl). The red Xs indicate the point corresponding to 65% of transduced cells. Whenever this percentage was not reached, the volume corresponding to the highest transduction rate was chosen as highlighted by the blue Xs.

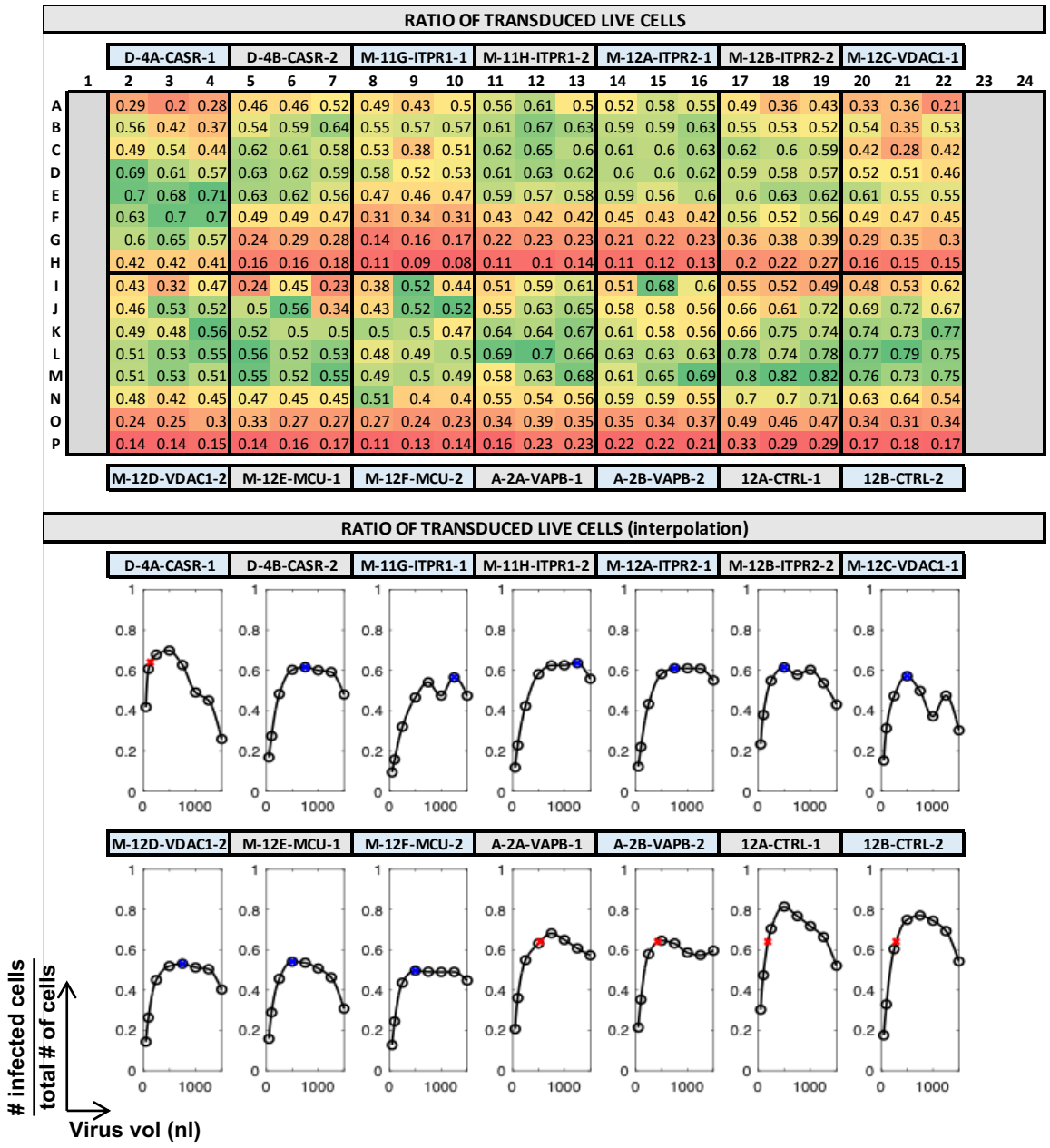


Figure 4.5: Titration of the lentiviruses for the expression of sgRNA (batch #3)

Well average of the ratio of transduced cells. Interpolation of the (# infected cells)/(total # of cells) ratio as a function of the volume of virus added (nl). The red Xs indicate the point corresponding to 65% of transduced cells. Whenever this percentage was not reached, the volume corresponding to the highest transduction rate was chosen as highlighted by the blue Xs.

is selected for further experiments.

Figures 4.3, 4.4, 4.5 show the results of the titration experiment performed in i^3 neurons. Some of the viruses show a saturation dose-response curve (e.g. D-8H-OSBPL5-2, Figure 4.4), suggesting that these viruses are not particularly toxic until the plateau is reached. Other viruses show an inverted U-shaped dose-response curve (e.g. D-7D-ATP2A2-2, Figure 4.3), suggesting that the highest viral concentrations might be toxic to the cells.

Whenever 65% efficiency of transduction is not reached by any virus volume, the volume corresponding to the highest infection rate was chosen instead. This approach was chosen in order to avoid any potential toxicity associated with treatment with different viral preparations. As a matter of fact, some of the viruses show a saturation dose-response curve where saturation is reached below 65% (e.g. M-12A-ITPR2-1, Figure 4.5), suggesting that increases in virus volume may not improve transduction efficiency, but toxicity may arise. In other cases, viruses show an inverted U-shaped dose-response curve (e.g. D-7B-ATP2A1-2, Figure 4.3), suggesting that the highest viral concentrations might be toxic to the cells, therefore the volume corresponding to the highest efficiency of transduction was chosen, even if it corresponded to less than 65% of positive cells.

4.4 Investigation of the effect of the ER and mitochondrial Ca^{2+} CRISPRi panel on Ca^{2+} release using a Fura-2 AM-based assay in i^3 neurons

In this Chapter, we sought to investigate the effect of genetic loss-of-function of the genes selected on Ca^{2+} homeostasis, using a Fura-2 AM-based assay. Despite the ultimate goal being to employ iPSC-derived DAns harbouring the *SNCA*-Trp and

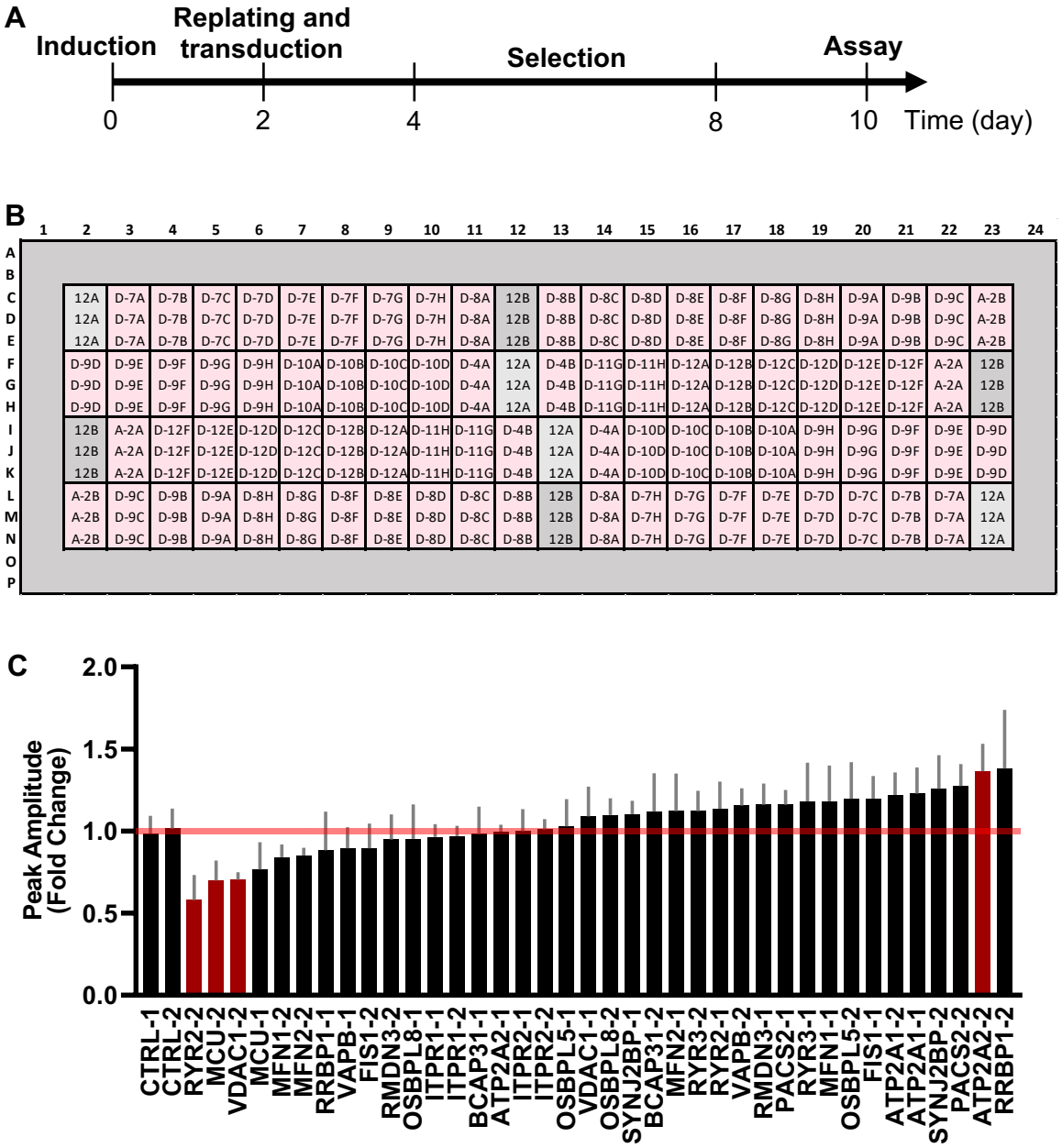


Figure 4.6: Effect of knock-down of ER and mitochondrial Ca^{2+}-related genes on Ca^{2+} dynamics

(A) Timeline of the experiment performed in i^3 neurons to assess the selected gene knock-downs on Ca^{2+} release using a Fura-2 AM-based assay. **(B)** Plate layout for the experiment. Control guides are depicted in grey and targeting guides in red. **(C)** Effect of the knock-down on ionomycin-induced Ca^{2+} release; each bar represents an individual sgRNA and shows the peak amplitude of the Fura-2 AM trace normalised to the two control sgRNAs. Data obtained from 1 differentiation; n=6 wells for the targeting guides and n=12 for the control guides on one single plate, as shown in the plate layout in B. Data represented as mean+SEM. RYR2-2 p=0.041, MCU-2 p=0.068, VDAC1-2 p=0.004, ATP2A2-2 p=0.088.Comparison between samples: two-tailed t-test.

GBA-N370S mutations, we performed a preliminary experiment in dCas9-KRAB-expressing i^3 neurons, which are glutamatergic in nature [Tian et al., 2019].

For this experiment, 48 h after transduction, transduced cells were selected using antibiotic in order to increase homogeneity. Cells were plated as shown in Figure 4.6 B; in particular, the plate is designed to have a central symmetry in order to counterbalance plate position effects. Controls (12A and 12B) are interspersed throughout the plate to keep track of potential left-to-right and top-to-bottom plate drifts. At the moment, no correction for plate drift is in place, but the control distribution will allow us to correct for plate drift if needed.

For the analysis, individual wells were used as technical replicates and as an N. For the analysis a t-test was used, to compare individual guides to the control non-targeting guides. No multiple test correction was performed in order to avoid losing significance considering the small Ns. As a future plan, the hits will then be validated in a smaller-scale experiment using multiple differentiations.

This preliminary experiment highlighted several potential hits. In particular, knock-downs of *RYR2*, *MCU* and *VDAC1* appear to decrease Ca^{2+} release upon ionomycin stimulation, while *ATP2A2* (*SERCA2*) knock-down appears to increase Ca^{2+} release upon ionomycin stimulation (see Figure 4.6 C). All these genes are well-characterised Ca^{2+} channels and pumps. This might suggest that the assay is sensitive enough to pick out relevant hits.

4.5 Establishment of dCas9-KRAB polyclonal patient-derived iPS cell lines

The ultimate goal of using dCas9-KRAB to knock-down genes encoding for ER and mitochondrial membrane proteins is to discover which of these genes are responsible for modulating Ca^{2+} release in DAns. In particular, we aim to phenocopy the

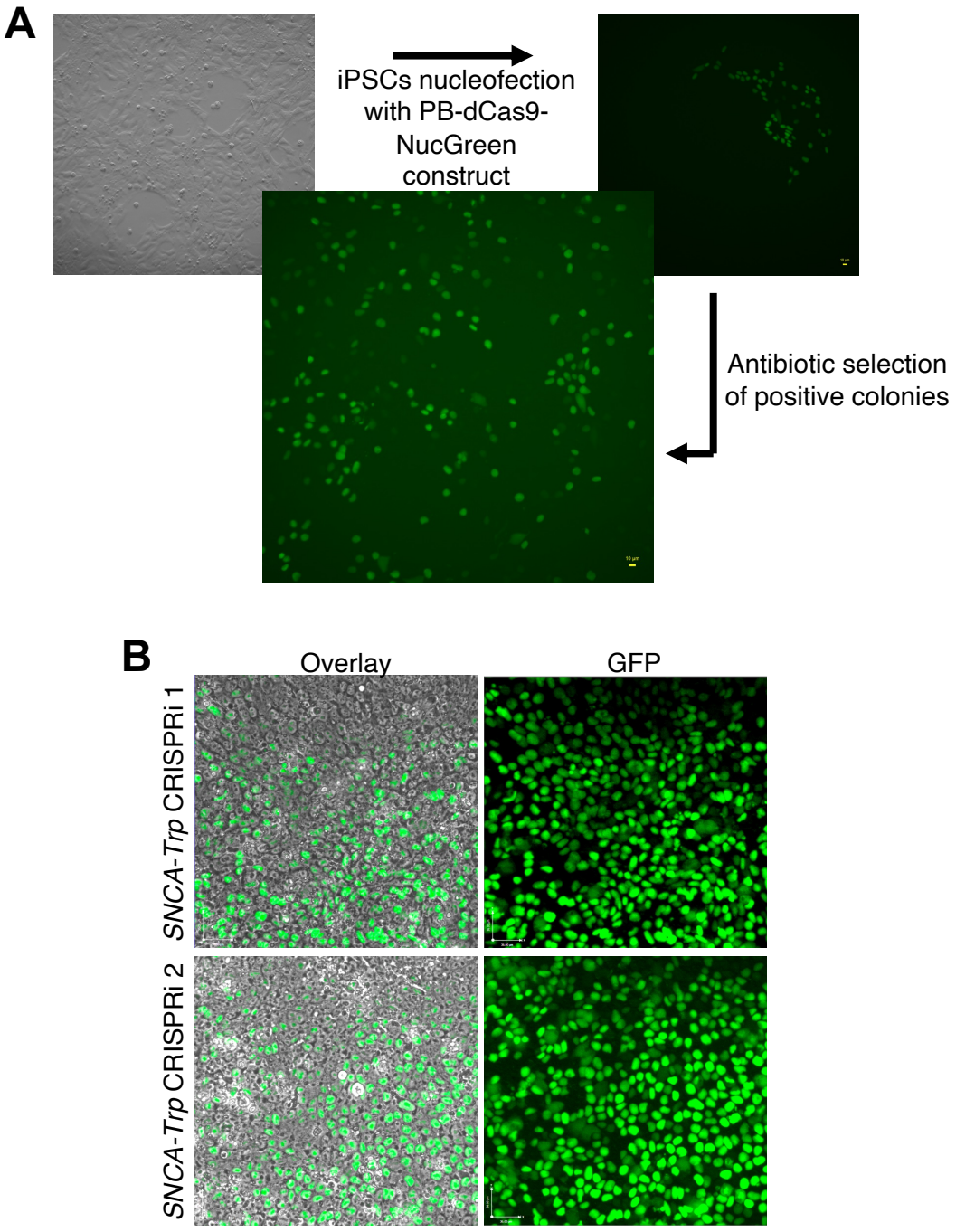


Figure 4.7: Generation of dCas9-KRAB polyclonal patient-derived iPS cell lines using a PiggyBac system

(A) Workflow for the generation of dCas9-KRAB polyclonal patient-derived iPS cell lines using a PiggyBac system. **(B)** Example image of two of the lines generated after the final selection. The PiggyBac construct has a nuclear NeonGreen marker to track the percentage of positive cells.

observations made in the patient lines and/or to rescue the Ca^{2+} dynamic defects in the patient lines.

In order to do so, it is necessary to generate iPSC lines from the pool of lines studied in Chapter 3. This was achieved by nucleofecting the cells at the iPSC stage with a PiggyBac construct for the expression of dCas9-KRAB in order to obtain stable polyclonal lines. The workflow to generate the lines is described in Figure 4.7.

Two control, two *SNCA*-Trp and one *GBA-N370S* dCas9-KRAB lines were generated. Figure 4.7 shows the two *SNCA*-Trp dCas9-KRAB iPSC lines at the end of selection.

These lines will provide a useful resource for the laboratory to test this panel of sgRNAs and others.

4.6 Discussion

In this Chapter we generate, clone and prep a medium-large sgRNA panel including sgRNAs targeting several ER and mitochondrial protein-encoding genes. The genes were selected based on their localisation and their involvement in Ca^{2+} handling. Wherever more than one isoform was present, the genes encoding for the highest expressed isoforms in DAns were prioritised. The panel was cloned successfully (Figure 4.2) and the viral preparations showed a good titer (Figures 4.3, 4.4 and 4.5).

In order to assess the effect of knock-down of the selected genes on Ca^{2+} dynamics, a Fura-2 AM experiment was performed. Even if Fura-2 AM-based assays give a rather crude measure of the Ca^{2+} dynamics and in combination with ionomycin it does not provide much spacial resolution, this assay is easily scalable to a medium-high throughput assay which is very fitting for this kind of screening.

A first preliminary experiment was performed on i^3 neurons where the dCas9-KRAB machinery was knocked-in in a safe-harbour locus [Tian et al., 2019]. After differentiation, these neurons are positive for markers of glutamatergic neurons. Even if this cell type may not be as relevant as SNpc DAns, some interesting information can be derived about the effect of these genes on Ca^{2+} dynamics in the general neuronal population. The stable integration of the dCas9 machinery and the fast and efficient differentiation process, make these neurons a great tool for functional genetic screenings. This experiment could provide a first understanding of the role of the protein encoded by the selected genes on the development of the Ca^{2+} mishandling in PD described in Chapter 3 provided that the Ca^{2+} response is homogeneous across neurons with different identities. The differentiation time of these cells is much shorter than that of DAns (Figure 4.6 A) and – deriving from a single clone of cells positive after the knock-in – 100% of the cells

express stably similar levels of dCas9-KRAB machinery, thus eliminating possible confounding factors coming from a non-homogeneous cell population. For these reasons, these cells are particularly suitable for knock-down screenings and they have been widely used to this end [Tian et al., 2019, Tian et al., 2021].

This preliminary experiment highlighted a few potential hits. In particular, knock-downs of *RYR2*, *MCU* and *VDAC1* appear to decrease Ca^{2+} release upon ionomycin stimulation, while *ATP2A2 (SERCA2)* knock-down appears to increase Ca^{2+} release upon ionomycin stimulation (see Figure 4.6 D). Even if this was just a preliminary experiment, it highlighted a number of genes that are known to be involved in Ca^{2+} homeostasis, suggesting that the assay might be sensitive enough for this screen.

However, some of the guides (such as RYR guides) do not appear to cluster together. This might be caused inefficacy of some of the guides to knock-down the gene of interest, therefore it could be necessary to test knock-down efficacy by qPCR. It is also possible that some of the guides may cause an almost complete knock-down of the gene of interest, which might result in cell toxicity and increased fitness of cells that escaped knock-down; in order to test this hypothesis it could be necessary to measure guides toxicity by ToxiLight assay and nuclei count.

One of the most reproducible effects was obtained with knock-down of SERCA pumps, as three of the four guides targeting *SERCA1* and *SERCA2* clustered together showing a similar phenotype, thus making this finding particularly compelling.

When ER Ca^{2+} is depleted, the ER is refilled by SERCA in combination with SOCE; SOCE caused an increase in cytoplasmic Ca^{2+} through the opening of membrane channels and then the Ca^{2+} is pumped back into the ER by SERCA. It is possible that in cells where SERCA has been knocked-down, stimulation of

Ca^{2+} release from the ER may be followed by SOCE, but – because of the knock-down – also by a slow refilling of the ER and more Ca^{2+} lingering in the cytoplasm for longer. If both isoforms were effectively knocked-down, this would result in a slow, but complete emptying of the ER and an overall increase of cytoplasmic Ca^{2+}. However, if the knock-down is partial and only affects one of the isoforms, it is possible that ultimately ER Ca^{2+} would be replenished, even if more slowly. In this scenario, the ER Ca^{2+} release elicited by ionomycin would be almost unaltered and even potentiated by SOCE. Therefore, it is possible the slower refilling would cause a bigger Ca^{2+} signal after stimulation, as observed in our experiment.

This hypothesis could be verified by performing the experiment in a Ca^{2+}-free environment and by performing multiple knock-downs of the genes encoding for the different isoforms at once.

Two guides targeting MCU clustered together showing a decrease in the ionomycin-induced Ca^{2+} signal; the fact that two biological replicates behave similarly suggests that MCU might be a real hit.

MCU is a Ca^{2+} uniporter located on the IMM and is responsible for Ca^{2+} entry into the mitochondrial matrix. In the presence of physiological concentrations of extracellular Ca^{2+} it has been demonstrated that MCU is necessary for SOCE and that MCU knock-down reduced SOCE Ca^{2+} current [Gonzalez-Sanchez et al., 2017, Samanta et al., 2019].

Therefore, we believe that the decrease in the ionomycin-induced Ca^{2+} signal that we observed might be caused by a decrease in SOCE.

The ultimate goal of the work in this Chapter is to bring this experiment into iPSC-derived DAns. Therefore we have generated two *SNCA*-Trp and *GBA-N370S* dCas9-KRAB lines. We expect that these lines in combination with the panel of

sgRNAs presented in this Chapter will allow us to phenocopy in the control lines the observations made in the patient lines and to rescue the Ca^{2+} dynamics defect in the patient lines. We believe that these findings will help us understand the disease mechanisms involved in Ca^{2+} mishandling in PD patients.

As an orthogonal technique to study ER and mitochondrial membrane proteins, we have optimised an APEX2-based subcellular compartment-specific proteomics experiment in iPSC-derived DAn cultures (see Chapter 5).

Chapter 5

Study of ER and mitochondrial membrane proteins using APEX2-based spatial proteomics

5.1 Introduction and Aims

In Chapter 3 we showed that iPSC-derived DAns carrying the *SNCA*-Trp mutation display ER and mitochondrial Ca^{2+} dyshomeostasis. In particular, we observed that patient-derived neurons may release less Ca^{2+} from the ER upon stimulation. Besides, Ca^{2+} uptake in the mitochondria may be reduced.

This dysregulation might be caused by a differential expression of the Ca^{2+} channels located on the membranes of ER and mitochondria and – more specifically – on the MAMs or by alterations in the ultrastructure of the MAMs themselves, which is crucial for Ca^{2+} regulation. Therefore, we would like to study the proteome of ERM, OMM and MAMs in order to highlight differences in protein expression between *SNCA*-Trp and controls, with the ultimate goal of unveiling the source of the described alteration in Ca^{2+} dynamics and investigating the possible involve-

ment of the protein α-synuclein.

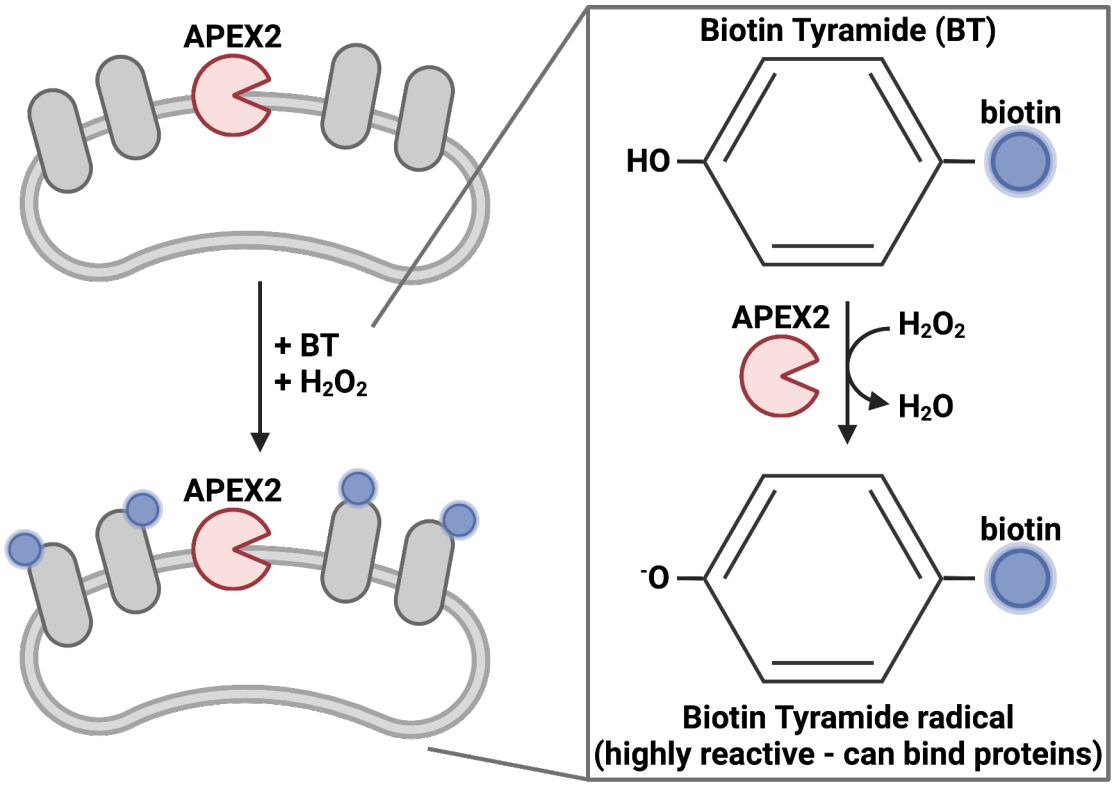


Figure 5.1: APEX2 catalysis of proximity biotinylation reaction

Traditionally, purification of mitochondria, ER and their membranes has been accomplished using subcellular fractionation, however, these approaches cannot guarantee fine spatial resolution between the two organelles. Therefore, we will take advantage of a recently developed technique: APEX2-catalised proximity labelling subcellular proteomics.

In APEX2-catalised proximity labelling subcellular proteomics, spatial resolution is obtained through genetic targeting of the peroxidase APEX2. In the presence of H_2O_2 and biotin tyramide, APEX2 catalyses a reaction that results in the biotinylation of all the proteins in close proximity to APEX2 itself (see Figure 5.1). This way, it is possible to specifically label the proteins resident in the region of interest with high spatial resolution. Labelled proteins are subsequently precipitated with

streptavidin beads and processed for mass spectrometry (see Figure 5.2).

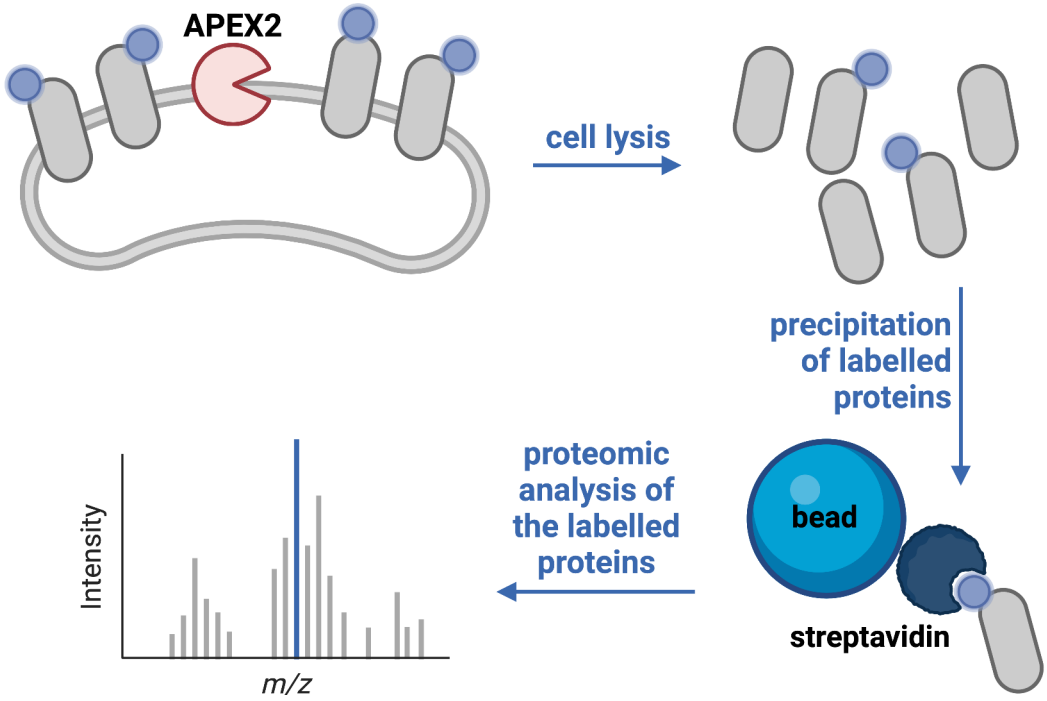


Figure 5.2: Proximity biotinylation for spatially-resolved proteomics

Our experimental design follows the one described by [Hung et al., 2017] and involves the use of an ER membrane-targeted APEX2 (ERM-APEX2) and an OMM-targeted APEX2 (APEX2-OMM) to label the two compartments. The two regions of interest are not membrane-bound; therefore, controlling for potential cytoplasmic protein contamination is necessary and is achieved by mapping the cytoplasmic proteome using a cytoplasmic APEX2 (APEX2-NES). Finally, biotinylated proteins naturally occur in cells so a non-transduced control will also be employed.

It will then be possible to generate a list of ERM-resident proteins and a list of OMM-resident proteins, which can be intersected. Proteins found in the intersection will constitute putative MAM-resident proteins. The lists obtained will be compared by genotype to highlight potential differences between genotypes.

Aims of the Chapter

- Clone ERM-APEX2, APEX2-OMM and APEX2-NES into an all-in-one Tet-ON expression system
- Generate a panel of control and patient-derived iPSC lines expressing ERM-APEX2, APEX2-OMM and APEX2-NES
- Optimise ERM-APEX2, APEX2-OMM and APEX2-NES in iPSC-derived DAns
- Perform a preliminary mass spectrometry experiment to assess the ability of ERM-APEX2 to label ERM proteins in iPSC-derived DAns

5.2 ERM-APEX2, APEX2-OMM and APEX2-NES cloning into a Tet-ON expression system

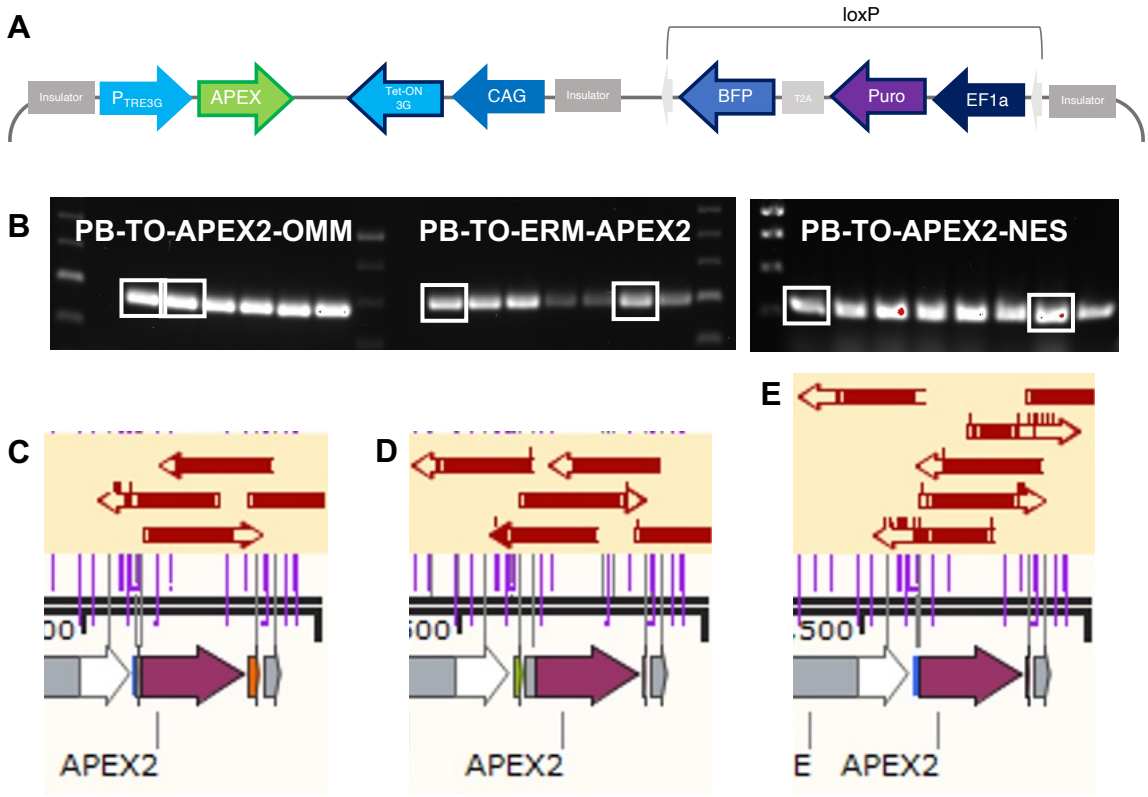


Figure 5.3: Cloning ERM-APEX2, APEX2-OMM and APEX2-NES into an all-in-one Tet-ON expression system

(A) Cartoon of PB-TO-APEX2. **(B)** cPCR-positive clones. **(C-E)** Sequencing-positive clones.

In order to generate the constructs PB-TO-APEX2-OMM, PB-TO-ERM-APEX2, and PB-TO-APEX2-NES the inserts were respectively amplified by PCR from Addgene plasmids #79056, #79055 and #92158 developed by [Hung et al., 2017]. The inserts were cloned into the PB-TO-NGN2 backbone. Colonies underwent a first round of screening using cPCR. Two cPCR-positive colonies underwent further screening via sequencing (see Figure 5.3). The methods are described in Section 2.3.

5.3 Establishment of ERM-APEX2, APEX2-OMM and APEX2-NES polyclonal patient-derived iPS cell lines

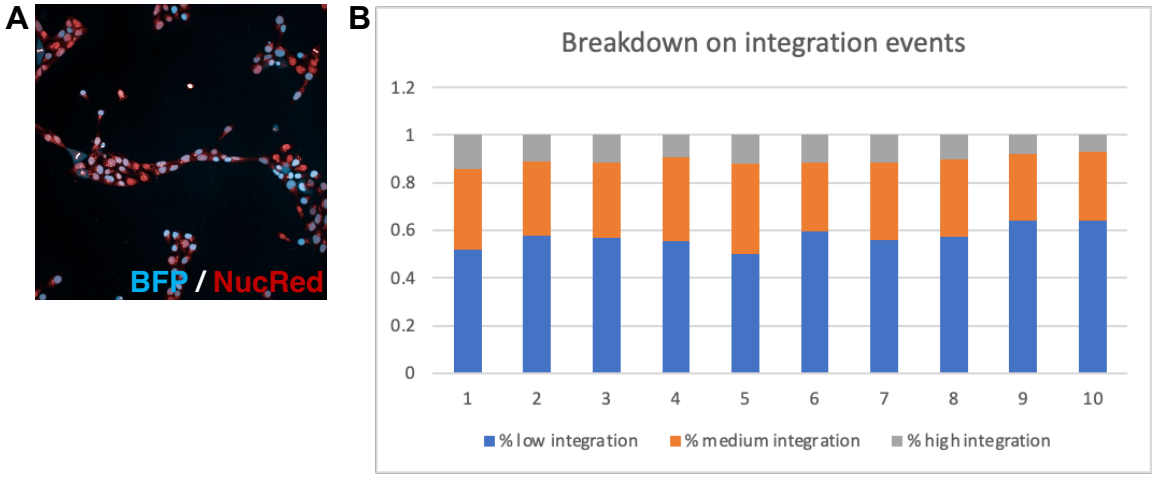


Figure 5.4: Generation of ERM-APEX2, APEX2-OMM and APEX2-NES polyclonal patient-derived iPS cell lines using a PiggyBac system

(A) Example image of one line generated after the final selection. The PiggyBac construct has a nuclear mTagBFP2 marker to track the percentage of positive cells. **(B)** Percentage of cells displaying low, medium or high copy numbers of the construct across the 10 of the 18 lines generated.

ERM and OMM constitute a subcellular compartments with specific biochemical properties and a specific proteome. However, they are not membrane-bound. When APEX biotinylates proteins, it does not show any selectivity. In fact, it tags any protein nearby and the more enzyme is expressed, the bigger the pool of targeted proteins. For membrane-bound organelles, no matter how high the APEX2 concentration is, the enzymatic activity of the protein will be confined within the membrane. Unfortunately, with ERM-APEX2 and APEX2-OMM, there is a risk that too high an expression of the constructs might cause a spill-over of the labelling to cytoplasmic proteins.

However, mass spectrometry requires a large amount of protein to work correctly, therefore there is a balance to be stuck between specificity and sample size.

To do so, we decided to increase specificity by putting the constructs under the TRE promoter which is a weaker promoter compared to promoters like EF1α and is inducible so the expression of the construct can be regulated. We decided to increase the sample size by trying to increase the number of cells expressing the construct by introducing the construct into stem cells and using antibiotic to select the transfected cells. Finally, APEX-NES will be employed as a control for potential cytoplasmic protein contamination.

We generated 3 control lines and 3 *SNCA*-Trp lines expressing the three constructs separately for a total of 18 lines (see Figure 5.5) with the ultimate goal to compare the proteomes of each subcellular comportment between patients and controls.

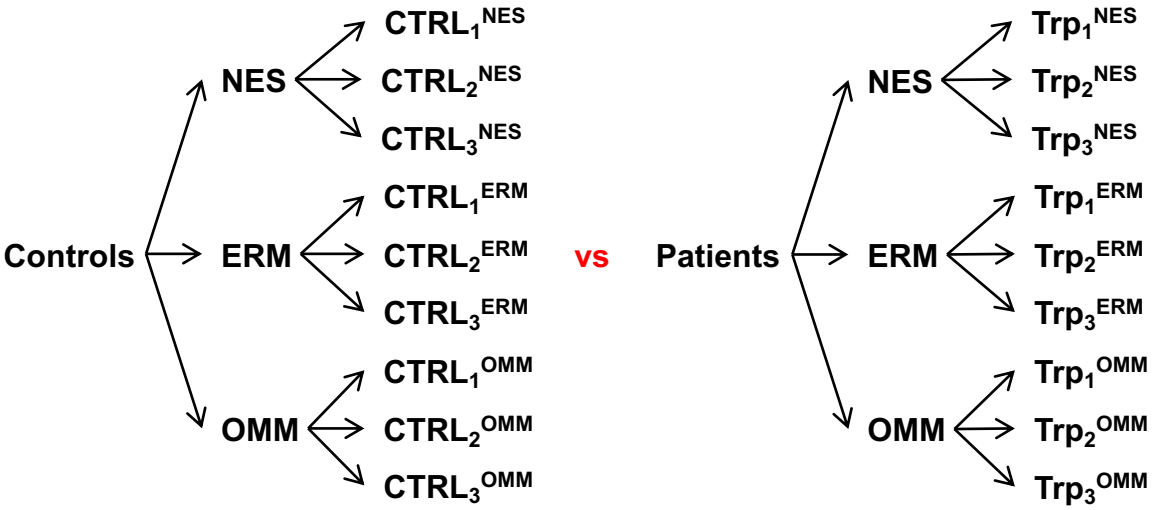


Figure 5.5: Diagram showing the lines generated

In order to compare the proteomes of different lines, it would be ideal to have a similar expression of the APEX constructs in the different lines. This way it is expected that a similar amount of protein will be labelled by the enzyme and pulled down thus making the proteomes of the different lines more comparable. Therefore

we decided to assess the number of integrations of the constructs in different lines. Figure 5.4 A shows an example image of an APEX line after selection. Because of the high number of lines to be generated, lines were nucleofected, selected and expanded in batches. In order to control for batch effect, we selected 10 lines from the different batches and analysed the intensity of the nuclear mTagBFP2 tag as a proxy for the number of integrations of the construct in the different batches. We set two arbitrary intensity thresholds to divide the cell population into low-, medium- and high-number of integrations. We then calculated the percentage of cells falling in each category for the 10 different lines and compared the distributions across lines. Figure 5.4 B shows a good degree of homogeneity across the lines.

5.4 Optimisation of ERM-APEX2, APEX2-OMM and APEX2-NES in iPSC-derived DAns

After the generation of the lines, we sought to evaluate the function of the constructs in DAns. First, we assessed the ability to induce the constructs using doxycycline. Figure 5.6 A shows the induction of the ERM-APEX2 construct; the construct has a V5 tag to allow for immunodetection. Unfortunately, it was not possible to visualise APEX2-NES and APEX2-OMM due to problems with the immunodetection of the Flag tag used to label them.

In order to assess APEX2 localisation, we fractionated the sample into cytoplasmic and membrane fractions. Figure 5.6 B shows that the ERM-APEX2 construct is enriched in the membrane fraction, as expected. Unfortunately, as mentioned above, it was not possible to visualise APEX2-NES and APEX2-OMM.

After assessing the correct expression and localisation of the construct, we sought to measure the enzymatic activity of APEX2 in DAns. In particular, we

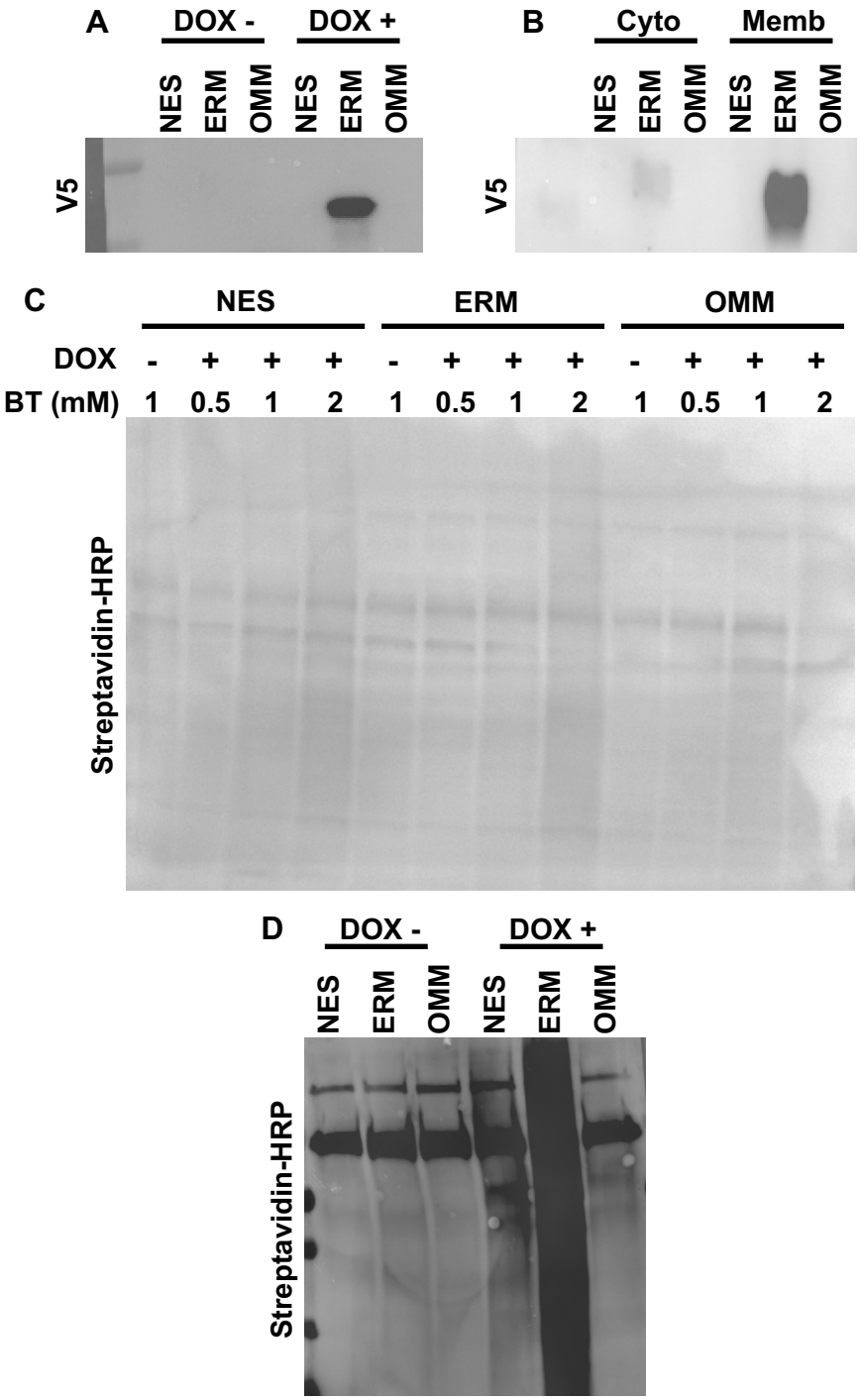


Figure 5.6: Optimisation of APEX2-NES, ERM-APEX2 and APEX2-OMM in iPSC-derived DAns

(A) Total cell lysate of APEX2-NES, ERM-APEX2 and APEX2-OMM iPSC-derived DAns. **(B)** Cytoplasm (Cyto) and membrane (Memb) fractionation of APEX2-NES, ERM-APEX2 and APEX2-OMM iPSC-derived DAns. **(C)** Total cell lysate of APEX2-NES, ERM-APEX2 and APEX2-OMM iPSC-derived DAns showing different biotinylation conditions. **(D)** Pulldown of biotinylated proteins in APEX2-NES, ERM-APEX2 and APEX2-OMM iPSC-derived DAns.

wanted to assess the effect of using different concentrations of the APEX2 substrate biotin tyramide (see Figure 5.1) on the efficacy of biotinylation.

Figure 5.6 C shows that biotin tyramide at 2 mM can increase the biotinylation of proteins in DAns compared to the non-induced control.

Finally, we precipitated the labelled proteins (see Figure 5.2) to see whether we could enrich for the labelled proteins. Figure 5.6 D shows that we can enrich for ERM-APEX2 labelled proteins and partially for APEX-NES and APEX2-OMM labelled proteins.

5.5 Preliminary mass spectrometry experiment to assess the ability of ERM-APEX2 to label ERM proteins in iPSC-derived DAns

Considering that we can enrich very well for ERM-APEX2 labelled proteins (see Figure 5.6 D), we wanted to assess whether the ERM-APEX2 labelled proteins in DAns resembled those published in [Hung et al., 2017].

The sample was submitted for mass spectrometry and the datasets were compared. The dataset from this Thesis is much smaller (559 proteins identified) than the one published by [Hung et al., 2017] (5270 identified) because we opted for low-depth processing for this preliminary experiment.

For their analysis, [Hung et al., 2017] cleaned their dataset from potential contaminants and from cytoplasmic-resident proteins. After this analysis, they obtained a list of *bona fide* ERM proteins (ERM proteome), which consists of (~12%) of the original dataset (see Figure 5.7 A).

Interestingly ~85% of our raw dataset overlaps with the ERM raw dataset published by [Hung et al., 2017] (see Figure 5.7 B). This suggests that the system may

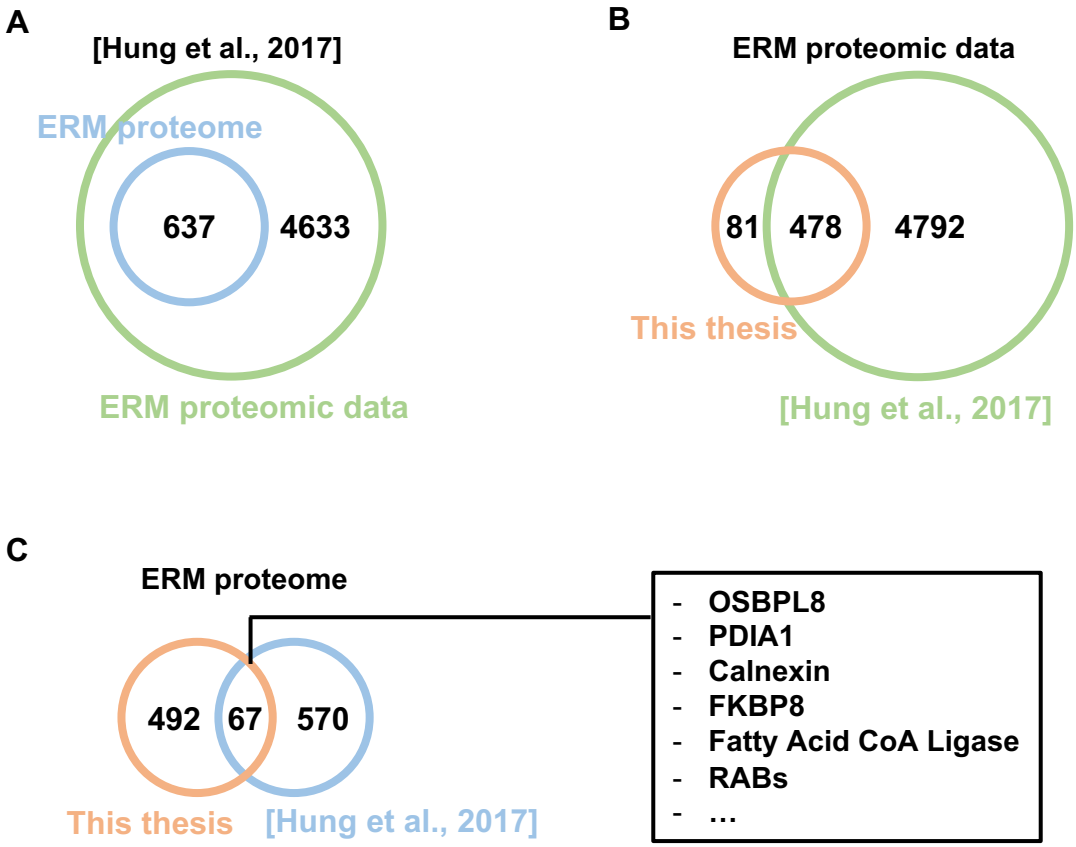


Figure 5.7: Mass spectrometry experiment to assess the ability of ERM-APEX2 to label ERM proteins in iPSC-derived DAn

(A) Diagram showing that out of 5270 proteins identified by [Hung et al., 2017] in the ERM-APEX2 sample, only 637 were confirmed (~12%). Data obtained from [Hung et al., 2017]. **(B)** Diagram showing that out of 559 proteins identified in the DAn ERM-APEX2 sample, 478 were also identified by [Hung et al., 2017] (~85%). **(C)** Diagram showing that out of 559 proteins identified in the DAn ERM-APEX2 sample, 67 were in the ERM confirmed proteome identified by [Hung et al., 2017] (~12%); a list of proteins found in the intersection is also presented.

work as expected in DAns and using an inducible system.

We also sought to analyse what fraction of our raw dataset overlapped with the ERM proteome. Interestingly ~12% of our raw dataset overlapped with the ERM proteome. Figure 5.7 C shows a list of some of the overlapping proteins.

5.6 Discussion

In this chapter, the ERM-APEX2, APEX2-OMM and APEX2-NES constructs were cloned into an all-in-one Tet-ON system. We also successfully generated 18 iPSC lines from 3 controls and 3 *SNCA*-Trp patients expressing the three constructs separately.

We then proceeded to the optimisation of the proximity biotinylation reaction in iPSC-derived DAns. Western-blot analysis proved successful for the ERM-APEX2 construct in one control line.

Unfortunately, the biotinylation reaction in the other two constructs was not as effective. In addition, we were not able to visualise the constructs by looking at the FLAG peptide used to tag them. The anti-FLAG antibody had many non-specific bands in non-transfected iPSC-derived DAns, which might mask the specific signal coming from the tagged APEX2. In addition, we believe that the APEX2-OMM and APEX2-NES might be expressed at lower levels than ERM-APEX2 constructs which could explain the lower biotinylation signal. It is possible to induce the construct for a longer period of time in order to increase expression and obtain better biotinylation and potentially manage to visualise the construct by Western blot.

A preliminary MS experiment shows a high degree of overlap (85%) between the DAns ERM raw dataset and the ERM raw dataset published by [Hung et al., 2017] However, only ~12% of our raw dataset overlapped with the ERM proteome. Although this number might appear quite small, it is interesting to observe that a similar percentage is obtained when comparing the ERM proteome and the ERM raw data published by [Hung et al., 2017]

The ERM is a non-membrane-bound subcellular compartment, therefore, it is possible that APEX2 biotinylation might spill over to the cytoplasm. In order to control for potential cytoplasmic protein contamination, [Hung et al., 2017] mapped

the cytoplasmic proteome using APEX2-NES. This way any cytoplasm-resident proteins in the ERM proteomic data (i.e. any protein appearing in both ERM and NES proteomic data) can be excluded from the ERM proteome.

However, this analysis excludes from the ERM proteome any real ERM that may also show cytoplasmic localisation, which could explain the low percentage of confirmed proteins.

Of interest, *bona fide* ERM-resident proteins in our dataset included:

- **OSBPL8 aka ORP8**, a MAM/ERM protein involved in lipid transport to the mitochondria
- **calnexin**, an ER Ca^{2+}-sensing chaperone involved in ERAD which shows preferential localisation in the MAMs
- **PDIA and FKBP**, ER chaperones
- **RABs**, involved in the secretory pathway
- **Fatty Acid CoA Ligase**, involved in lipid catabolism
- and others

These are well-known MAM, ERM and ER proteins and cover some of the most important ER functions.

Looking at differences in the expression of these proteins would be the next step.

The 18 APEX2 iPSC lines from 3 controls and 3 *SNCA*-Trp patients can now be employed for quantitative profiling of the proteomes of the ERM and the OMM in controls and patients. To perform a quantitative analysis, each sample will need

to be normalised against its respective NES control, in order to obtain an organelle enrichment score for each detected protein. The scores will then be averaged across lines belonging to the same genotype; a ratio of the score averages of the patients vs the score averages of the controls will be computed to highlight differentially expressed proteins in the ERM and OMM proteomes of *SNCA*-Trp patients. This approach, previously published in [Li et al., 2020] can be summarised by equations 5.1 and 5.2:

$$\frac{\sum Trp_i^{ERM}/Trp_i^{NES}}{\sum CTRL_j^{ERM}/CTRL_j^{NES}} \tag{5.1}$$

$$\frac{\sum Trp_i^{OMM}/Trp_i^{NES}}{\sum CTRL_j^{OMM}/CTRL_j^{NES}} \tag{5.2}$$

Through the organelle enrichment score, it will be possible to generate a list of ERM proteins and a list of OMM proteins and – from their intersection – a list of putative MAM proteins. It will then be possible to focus on the MAM proteins to see if any specific changes might occur, for instance, a change in the distribution; for example, an ERM protein may not display any changes in the expression level, but might relocalise to MAMs in the patients and, therefore, appear in the OMM proteome and the putative MAM proteins list.

This experiment will be performed in a single differentiation and individual patient lines will be used to account for the biological difference across individuals. The hits will then be validated by Western blot and ICC in multiple differentiations to account for technical differences arising from independent differentiations.

We believe that this proteomic approach will be very informative. By measuring the proteome of ERM and OMM and extrapolating the proteome of the MAMs, it gives us the possibility to explore many hypotheses at once:

- The ERM and OMM proteomes can provide information to verify or deny the hypothesis that the Ca^{2+} handling defect in PD patients might be arising from

Ca^{2+} channel dysfunction

- The MAM proteome can provide information to verify or deny the hypothesis that MAM dysfunction might be at the base of the Ca^{2+} phenotype.

This makes this approach very versatile and suitable for unbiased discovery of the mechanisms underlying Ca^{2+} release defects in PD patients. For a more focused study of the MAMs proteome, it could be possible to employ a split biotinylation enzyme design so that the complete and functional enzyme could only be localised to the MAMs [Cho et al., 2020].

We believe that proximity labelling subcellular proteomics could be performed in iPSC-derived DAns and could afford the possibility to dig deeper into the causes of the Ca^{2+} deficits described by studying the levels of Ca^{2+} transporters expressed in the ER and mitochondria of patient cells, with the ultimate goal to identify new therapeutic targets that can be used to ameliorate early PD disease phenotypes.

Chapter 6

Evaluation of FASN as a novel target for PD

6.1 Introduction and Aims

iPSC-derived DAns derived from patients are particularly suitable for phenotypic screenings. From the comparison with control cells, it is possible to highlight cellular phenotypes that one may aim to correct using libraries of drugs.

Recently, in the Wade-Martins laboratory, a screening of over 4000 compounds was performed in collaboration with AstraZeneca to correct the Ca^{2+} handling defects of *GBA-N370S*. In particular, for the screening a Fura-2 AM-based assay using ionomycin to measure intracellular Ca^{2+} release was performed. The assay was scaled up to a high-throughput assay and run in iPSC-derived DAn.

The primary screening was performed in a single *GBA-N370S* line and each compound was tested at a single concentration (10 μM). The primary screening identified 126 compounds that significantly increased Ca^{2+} release. These hits were confirmed in a secondary screening where each compound was administered at different concentrations to study the dose-response relationship and each com-

pound was administered to multiple lines (4 controls and 4 *GBA-N370S*) to evaluate the ability to increase Ca^{2+} release in multiple iPSC-DAns lines.

The secondary screening confirmed 23 hits and 17 individual targets. These targets were further validated in a second primary screening of over 1500 compounds from AstraZeneca known to show activity towards the 17 targets. These compounds included a number of chemical analogues of the original hit but also compounds with different chemical structures from the original hit. This screening confirmed 4 hits, which included FASN. Over 300 FASN inhibitors were tested and 49 (with 6 different chemistries) were able to increase Ca^{2+} release in a *GBA-N370S* line.

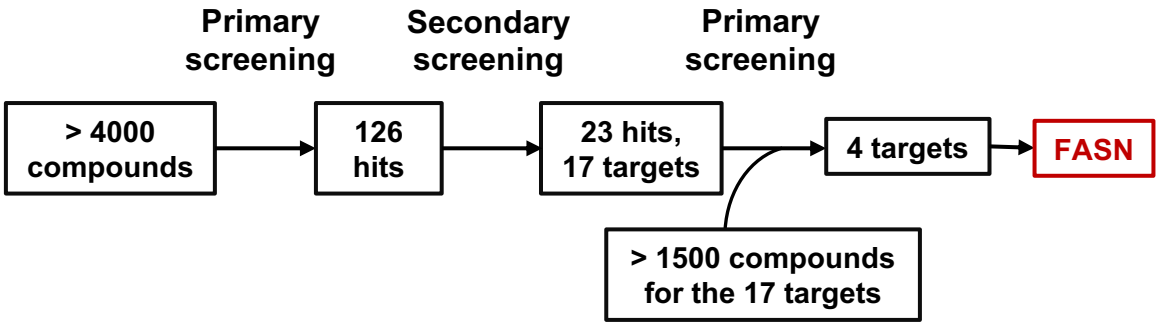


Figure 6.1: Screening pipeline

Out of the 4, FASN was selected for further investigations because this target was extensively studied by AstraZeneca in preclinical and clinical tests for different types of cancer. Therefore, AstraZeneca has developed a substantial panel of well-characterised compounds for this target. This has allowed the lab to select a number of compounds to test further based on their predicted ability to cross the blood-brain barrier and on their *in vivo* tractability, as well as their potency in iPSC-derived DAns.

FASN or fatty acid synthase is an enzyme at the base of the anabolism of free fatty acids (FFA), in particular, it catalyses the synthesis of palmitate, i.e. the

shortest saturated fatty acid. Recently, it has been suggested that FASN inhibition might be protective against mitochondrial damage in fly, mouse and iPSC-derived neuronal models of PD. In particular, FASN inhibition has been associated with increased levels of cardiolipin, an IMM lipid, and increased cardiolipin levels appear to be beneficial for mitochondrial health [Vos et al., 2017].

In this Chapter, the best-performing drug (referred to as FASN inhibitor 1) is tested to evaluate its ability to revert other phenotypes in *GBA-N370S* lines.

Aims of the Chapter

- Investigate the effects of FASN inhibition on ER health
- Investigate the effects of FASN inhibition on lysosomal health
- Perform a lipidomic analysis of FASN inhibitor-treated cells

6.2 Toxicity of FASN inhibitor 1

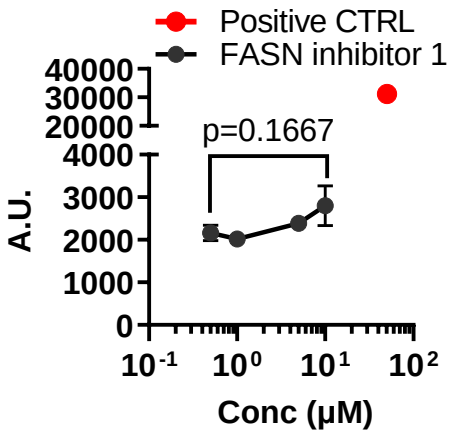


Figure 6.2: ToxiLight assay to evaluate FASN inhibitor 1 toxicity

First, we sought to measure FASN inhibitor 1 toxicity at different concentrations in DAns. Therefore, we measured adenylate kinase release in the cytoplasm from DAns treated with increasing concentrations of the drug using the Toxilight assay. Figure 6.2 shows that FASN inhibitor 1 does not display toxicity even at the highest concentration. Comparison between lowest and highest concentrations: one-tailed Mann-Whitney test.

6.3 Effect of FASN inhibitor 1 on ER health

FASN inhibitor 1 has been selected for its ability to rescue the Ca^{2+} handling defect in *GBA-N370S* patients. In addition to that, we wanted to assess its ability to rescue other phenotypes observed in these cells. In particular, we decided to focus on the ER Ca^{2+} release phenotype described in Chapter 3 and on ER stress as previously published in [Lang et al., 2019].

However, as published in [Lang et al., 2019], a pseudotime analysis of scRNAseq has shown that *GBA-N370S* DAns display different pathogenic events including

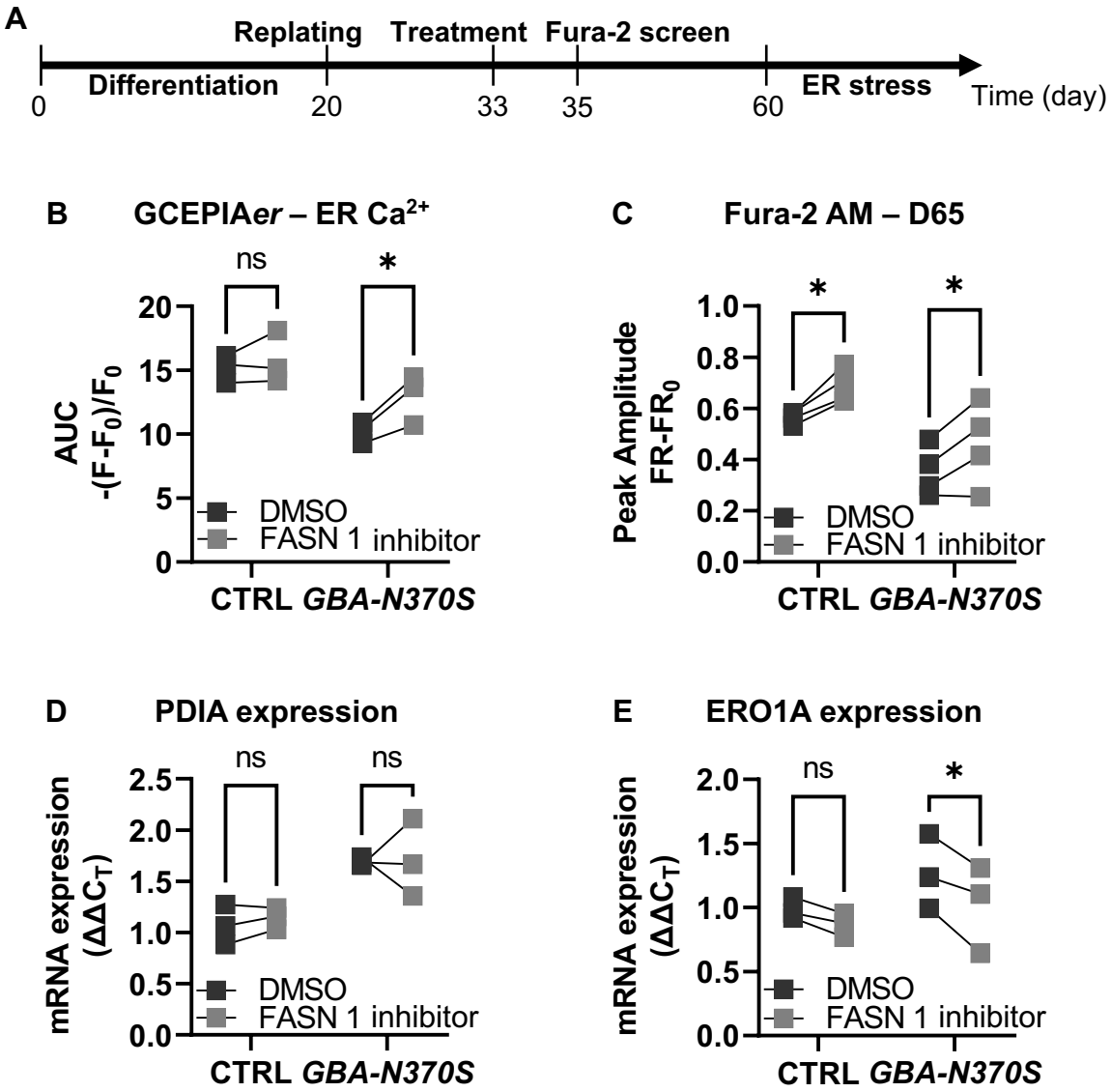


Figure 6.3: Effect of FASN inhibitor 1 on ER health

(A) Cartoon shows the screening timeline and the emergence of the ER stress phenotype. **(B)** Effect of FASN inhibitor 1 on ER Ca^{2+} release using a GCEPIA*er*-based assay. AUC of vehicle- and FASN inhibitor 1-treated CTRLs and *GBA-N370S*. Each data point represents an individual line averaged across 3 independent differentiations. Comparison between treatments: paired two-way ANOVA. **(C)** Effect of FASN inhibitor 1 on Ca^{2+} release at D65 of the differentiation using a Fura-2 AM-based assay. AUC of vehicle- and FASN inhibitor 1-treated CTRLs and *GBA-N370S*. Each data point represents an individual line averaged across 4 independent differentiations. Comparison between treatments: paired two-way ANOVA. **(D-E)** Effect of FASN inhibitor 1 on ER stress markers PDIA (D) and ERO1A (E). $\Delta\Delta C_T$ analysis of the expression of PDIA and ERO1A in vehicle- and FASN inhibitor 1-treated CTRLs and *GBA-N370S*. Each data point represents an individual line averaged across 3 independent differentiations. Comparison between genotypes: paired two-way ANOVA.

changes in the expression of HDAC4 regulated genes and ER stress at different stages of a hypothetical disease timeline. From this analysis, ER stress appeared to be a late event in this disease timeline. This is also evident from the fact that ER stress appears at a relatively late stage of cell maturation (D65). The Ca^{2+} phenotype appears at an early stage of maturation (D35), therefore, the screening was performed at D35 (see Figure 6.3 A).

This creates a mismatch between the timing of the two experiments that we need to keep in consideration.

Figure 6.3 B shows that FASN inhibitor 1 (5 μM) is able to increase Ca^{2+} release in response to ionomycin from the ER in *GBA-N370S* DAns. This suggests that there might be an increase in ER Ca^{2+} levels. It is known that a lack of ER Ca^{2+} can induce ER stress, therefore it is possible that the increase in the ER Ca^{2+} levels might also be reflected in reduced ER stress.

Before assessing ER stress levels at D65, we sought to investigate whether FASN inhibitor 1 (5 μM) was able to rescue the Ca^{2+} release phenotype in the Fura-2 AM-based assay at D65, therefore cells were treated at D63 and then assayed at D65. Figure 6.3 C shows that FASN inhibitor 1 (5 μM) is able to increase Ca^{2+} release in response to ionomycin in *GBA-N370S* and CTRL DAns in a Fura-2 AM-based assay at D65.

We then assessed ER stress by measuring the levels of two chaperones (PDIA and ERO1A) that were previously demonstrated to be upregulated in *GBA-N370S* iPSC-derived DAns [Lang et al., 2019]. Figure 6.3 E shows that FASN inhibitor 1 (5 μM) is able to decrease ERO1A levels, but not PDIA levels (D). This suggests that there might be a specific pathway through which FASN inhibitor 1 is able to decrease ERO1A.

6.4 Effect of FASN inhibitor 1 on lysosomal health

We sought to investigate the effect of FASN inhibitor 1 on lysosomal function. To do so we employed the DQ BSA reagent to measure active lysosome function and the MDW941 reagent to measure active GCase.

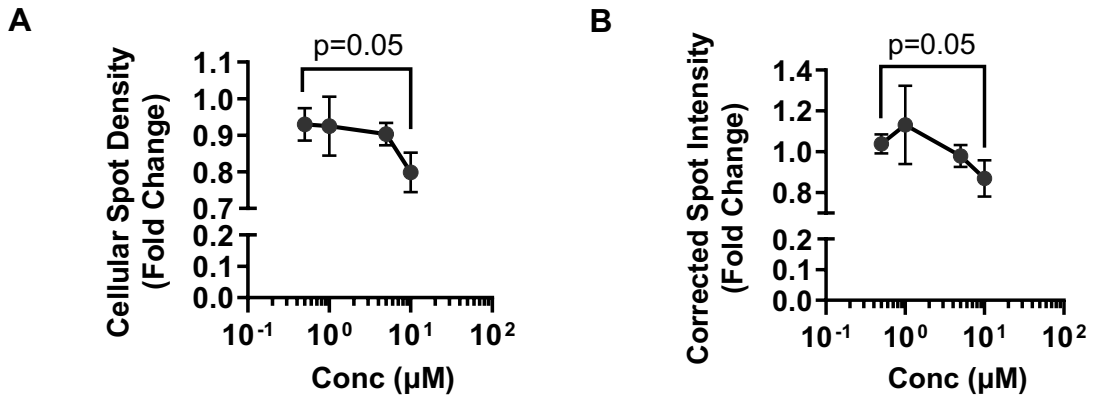


Figure 6.4: Effect of FASN inhibitor 1 on lysosomal function using a DQ BSA-based assay

(A) Effect of different concentrations of FASN inhibitor 1 on lysosome function. DQ BSA cellular spot density in response to different concentrations of FASN inhibitor 1. Each data point represents an individual line averaged across 3 independent differentiations. **(B)** Effect of different concentrations of FASN inhibitor 1 on lysosome function. DQ BSA corrected spot intensity in response to different concentrations of FASN inhibitor 1. Each data point represents an individual line averaged across 3 independent differentiations. Comparison between lowest and highest concentrations: one-tailed Mann-Whitney test.

DQ BSA reagent consists of BSA densely labelled with the fluorophore BODIPY that at high density shows self-quenching activity, therefore at baseline DQ BSA does not fluoresce. The reagent is internalised in the cell through the endosomal pathway; when the endosome fuses with the lysosome, the BSA peptides start to get degraded and the BODIPY fluorophores come apart. This results in a fluorescent spot that can be measured via imaging; the density of spots in the cell and the intensity of said spots can be used as a measure of lysosomal activity.

Figure 6.4 shows that FASN inhibitor 1 appears to slightly decrease lysosomal activity at the highest concentration. For further experiments, the second highest

concentration (5 μM) was selected.

GBA-N370S iPSC-derived DAns retain the lysosomal enzyme GCase in the ER and display decreased GCase activity [Fernandes et al., 2016]. Therefore, we wanted to investigate whether FASN inhibitor 1 could increase active GCase levels.

In order to measure active GCase levels, we employed the MDW941 reagent [Witte et al., 2010], which is a fluorescent probe that binds to active GCase, allowing us to measure the levels of lysosomal GCase via imaging. Once active GCase reaches the lysosome, MDW941 binds it and this results in a fluorescent spot; the density of spots in the cell and the intensity of said spots can be used as a measure of the levels of active GCase.

Figure 6.5 A shows that *GBA-N370S* iPSC-derived DAns display a 20% decrease in active lysosomal GCase compared to CTRLs. GCase spot intensity can be increased by FASN inhibitor 1 as shown in Figure 6.5 D, while the density of spots is unaltered (see Figure 6.5 C).

6.5 Lipidomic analysis of FASN inhibitor 1-treated cells

FASN inhibition should alter FFA concentrations in the cell, which should be reflected in an overall change in the lipid composition of the cell. Therefore, we decided to use a lipidomic analysis to measure lipid levels in CTRLs and *GBA-N370S* iPSC-derived DAns treated with different concentrations of FASN inhibitor 1. Here we will focus on the effect of FASN inhibition on phosphatidylcholine, phosphatidylethanolamine and phosphatidylserine levels.

These phospholipids are of particular interest because phosphatidylserine is synthesised in the ER, then shuttled to the mitochondria through the MAMs to

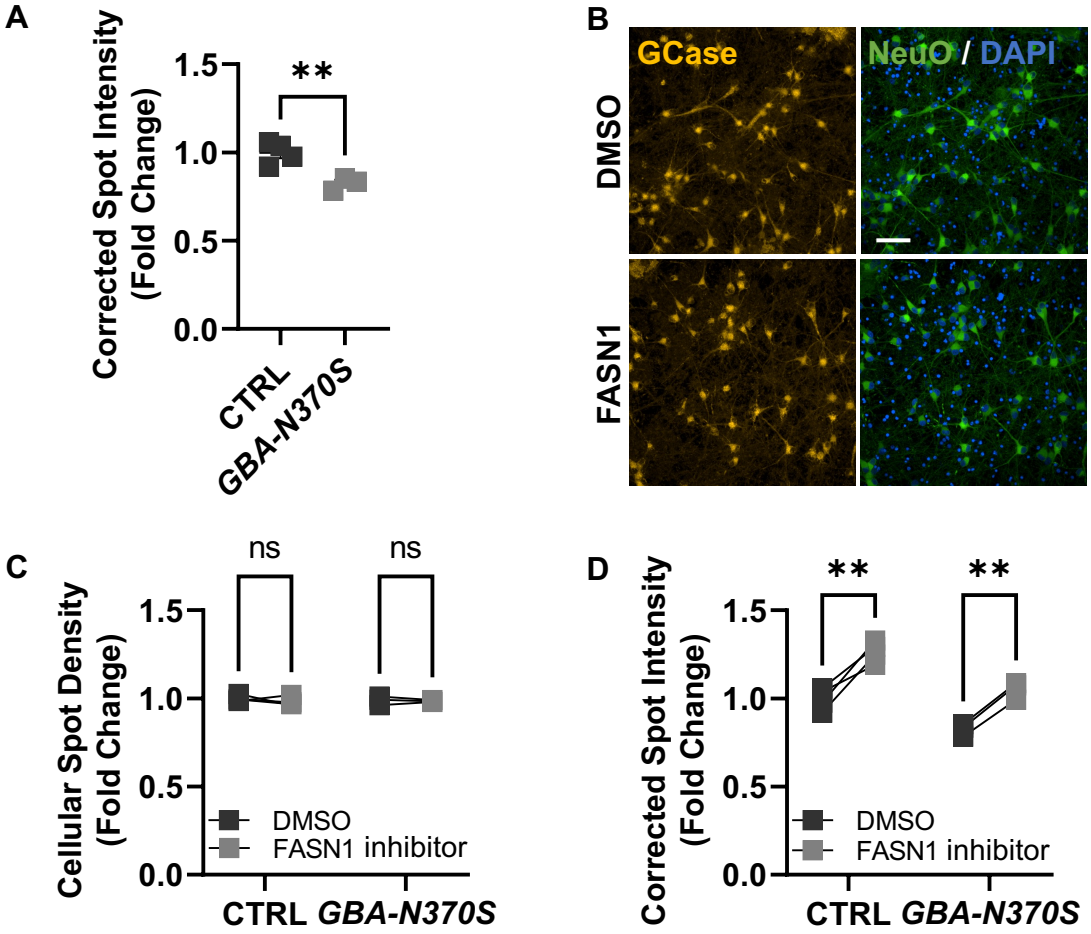


Figure 6.5: Effect of FASN inhibitor 1 on lysosomal function using a DQ BSA-based assay

(A) Active GCase in CTRLs and *GBA-N370S*. MDW941 corrected spot intensity in CTRLs and *GBA-N370S*. Each data point represents an individual line averaged across 3 independent differentiations. Comparison between genotypes: t-test. **(B)** Representative images of vehicle- and FASN inhibitor 1-treated CTRLs. Scale bar 100 µM. **(C)** Active GCase in vehicle- and FASN inhibitor 1-treated CTRLs and *GBA-N370S*. MDW941 cellular spot density in vehicle- and FASN inhibitor 1-treated CTRLs and *GBA-N370S*. Each data point represents an individual line averaged across 3 independent differentiations. Comparison between treatments: paired two-way ANOVA. **(D)** Active GCase in vehicle- and FASN inhibitor 1-treated CTRLs and *GBA-N370S*. MDW941 corrected spot intensity in vehicle- and FASN inhibitor 1-treated CTRLs and *GBA-N370S*. Each data point represents an individual line averaged across 3 independent differentiations. Comparison between treatments: paired two-way ANOVA.

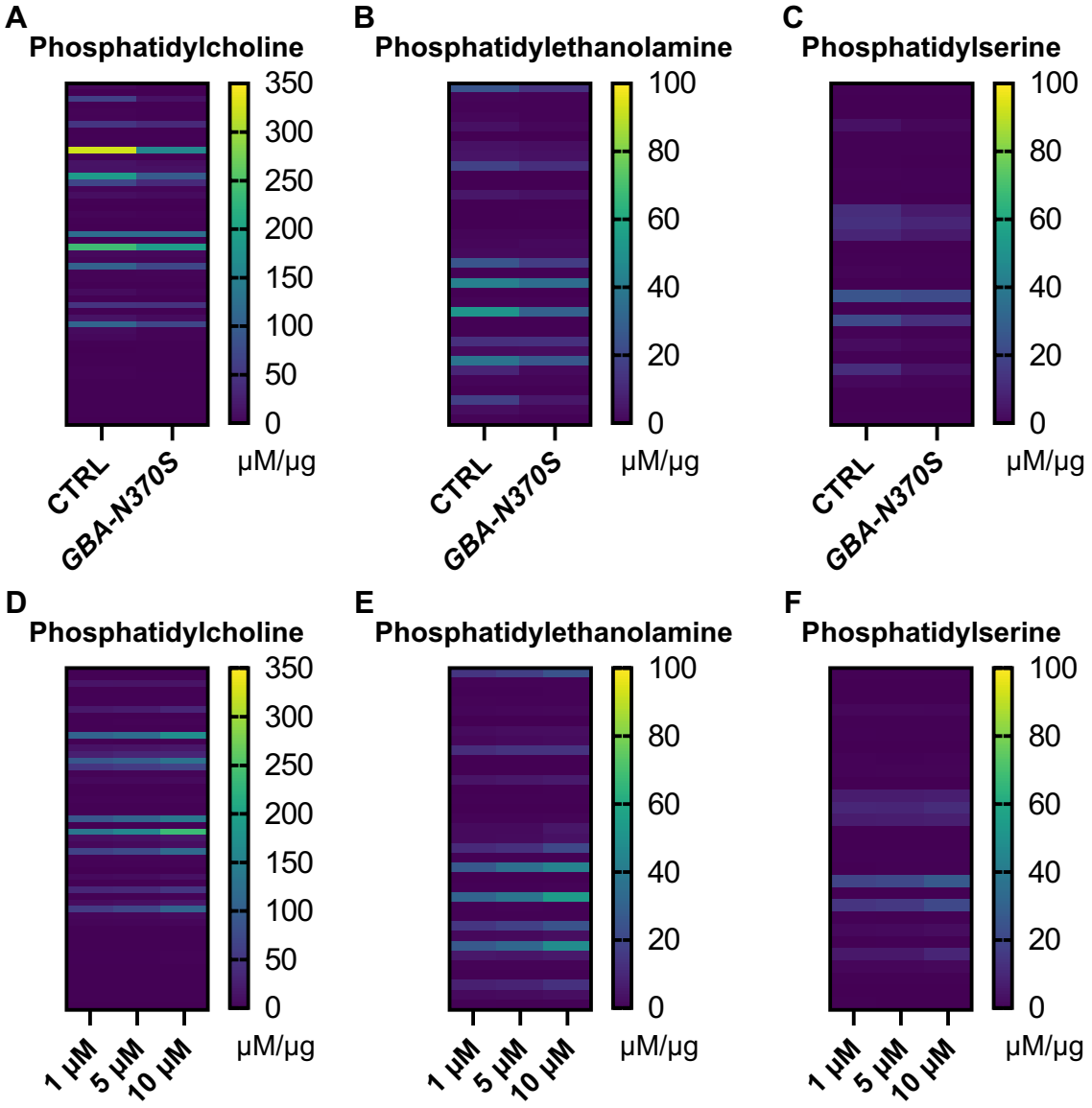


Figure 6.6: Effect of FASN inhibitor 1 on phospholipids levels

(A-C) Phosphatidylcholine, phosphatidylethanolamine and phosphatidylcholine levels in CTRLs and *GBA-N370S*. Data are normalised to total protein content, therefore the data are expressed as the concentration of lipid (µM) over the amount of protein (µg). Each data point represents an individual phospholipid species averaged across 3 lines. **(D-F)** Effect of different concentrations of FASN inhibitor 1 on phosphatidylcholine, phosphatidylethanolamine and phosphatidylcholine levels in *GBA-N370S* DAns. Data are normalised to total protein content, therefore the data are expressed as the concentration of lipid (µM) over the amount of protein (µg). Each data point represents an individual phospholipid species averaged across 3 *GBA-N370S* lines.

synthesise phosphatidylethanolamine [Vance, 1990, Xu and Huang, 2020]. In addition, LC3 binds phosphatidylethanolamine to initiate autophagy. Finally, phosphatidylcholine and phosphatidylethanolamine have been demonstrated to modulate SERCA function and therefore their levels can influence ER Ca^{2+} levels [Fu et al., 2011].

As shown in the previous Sections of this Chapter, FASN appears to increase ER Ca^{2+} and overall improve ER health in treated *GBA-N370S* iPSC-derived DAns. Because of their involvement in ER function and lysosomal function, we decided to specifically measure and analyse phosphatidylcholine, phosphatidylethanolamine and phosphatidylserine levels, with the ultimate goal of – at least partially – unveiling the mechanism through which FASN inhibitor 1 can increase intracellular Ca^{2+} release.

Interestingly, phosphatidylcholine, phosphatidylethanolamine and phosphatidylserine levels appear to be decreased in *GBA-N370S* lines compared to controls. The levels of these phospholipids in *GBA-N370S* are increased with increasing concentrations of FASN inhibitor 1.

6.6 Discussion

In this Chapter, we have evaluated the ability of FASN inhibitor 1 – a compound highlighted by a phenotypic screening in iPSC-derived DAns for its ability to increase Ca^{2+} release – to modify a number of cellular phenotypes described in *GBA-N370S* DAns.

Firstly, we decided to investigate the effect of FASN inhibitor 1 on ER stress. As published in [Lang et al., 2019], cytotoxic events appear at different stages of the disease pseudo timeline and ER stress appears at a relatively late stage of cell maturation (D65) compared to the Ca^{2+} handling defects (D35). The phenotypic screening was performed ad D35, but we have found that FASN is able to increase Ca^{2+} release also at D65, i.e. when phenotypes like ER stress are present.

We have also observed that FASN inhibitor 1 is able to decrease the expression of ERO1A – an ER chaperone used as a marker of ER stress – suggesting that it can decrease the ER stress response in *GBA-N370S* lines. ER stress can be induced by ER Ca^{2+} deficit, therefore it is possible that FASN inhibitor 1 decreases ER stress by increasing intracellular Ca^{2+}.

Interestingly, FASN inhibitor 1 appears to increase ER Ca^{2+}. SERCA pumps are responsible for the replenishment of ER Ca^{2+} levels. The activity of these transmembrane proteins is regulated by the membrane environment in which they are located. In particular, it can be regulated by the relative concentrations of phosphatidylcholine and phosphatidylethanolamine [Fu et al., 2011]. FASN is a crucial enzyme for the regulation of lipid synthesis, therefore we measured lipid levels in cells treated with FASN inhibitor 1. Interestingly, the inhibitor increases the levels of phosphatidylcholine and phosphatidylethanolamine.

We hypothesise that changes in phosphatidylcholine and phosphatidylethan-

olamine levels might positively modulate SERCA thus increasing their ER Ca^{2+} replenishment activity. This might result in an increase in ER Ca^{2+}, which in turn might be responsible for better ER chaperones function and decreased ER stress in the cells.

Secondly, we decided to investigate the effect of FASN inhibitor 1 on lysosomal health. *GBA-N370S* DAns display decreased GCase activity [Fernandes et al., 2016]. In this Chapter, we have measured active lysosomal GCase through imaging and we have used the intensity of the spots and density of spots in the cell as measures of active GCase. We have observed that FASN inhibitor 1 is able to increase the intensity of the spots; this can be interpreted as an increase in the amount of active GCase. The density of spots in the cell is unaltered, which suggests that the number of lysosomes (spots) containing active GCase is unaffected. Therefore, we believe that FASN inhibitor 1 might increase GCase protein activity rather than increasing lysosome biogenesis and genes involved in lysosomal function transcription as a whole.

This hypothesis is supported by the observation that FASN inhibitor 1 does not increase DQ BSA signal. In order to confirm that FASN inhibitor 1 does not increase lysosome biogenesis, it could be possible to measure lysosomal proteins level in treated and untreated cells.

We believe that FASN inhibitor 1 might increase GCase protein activity through LIMP2, a GCase chaperone, which is also a risk factor for PD [Reczek et al., 2007, Nalls et al., 2019]. In particular, the transcription factor SREBP1 is activated by decreased levels of fatty acids, therefore it is likely that FASN inhibitor 1 treatment could increase SREBP1 function. SREPB1 positively modulates a number of genes, including *SCARB2*, which encodes for LIMP2. We hypothesise that mutated *GBA* mutations encode for a form of GCase that is retained in the ER,

however, increased expression of LIMP2 could chaperone GCase out of the ER and through the exocytic pathway to the lysosomes. Therefore, FASN inhibitor 1 can increase the levels of active lysosomal GCase.

In order to confirm this hypothesis, it could be possible to measure *SCARB2* levels in treated and untreated cells. It could also be possible to measure the percentage of GCase retained in the ER as described in [Fernandes et al., 2016].

FASN appears to be a PD target with high potential and the drug-like compound FASN inhibitor 1 appears very appealing.

Some of the tools and datasets already described in this Thesis are suitable to further validate FASN inhibitor 1. In order to demonstrate target engagement, the lipidomic dataset is being employed by other members of the laboratory to assess the effect of FASN inhibitor 1 on well-known targets of the enzyme, such as cardiolipin [Vos et al., 2017]. In addition, the *GBA-N370S* dCas9 line described in Chapter 4 is being employed to knock-down FASN and validate the FASN inhibitor 1 target.

Chapter 7

Discussion

In this thesis, I employed iPSC-derived DAns to model PD. From this study, I was able to highlight intracellular Ca^{2+} handling defects in PD. The observation of phenotypes in this model offers a unique opportunity to aim to correct the phenotype in phenotypic screenings or reconstruct disease mechanisms with the ultimate goal of discovering new druggable targets in the very cells that degenerate in PD.

In this thesis, I tried to achieve both things. In order to study the mechanisms at the origin of the Ca^{2+} dynamics alterations, I carried out a preliminary functional genetic screening. I have also begun to optimise a proteomic analysis in DAns that could highlight differences in the proteome of PD lines vs controls and help in the dissection of this disease mechanism.

In addition, in collaboration with AstraZeneca, Janine Brandes and Dr Brent Ryan have recently screened more than 4000 compounds for their ability to recover the Ca^{2+} handling defect in *GBA-N370S* DAns. In this thesis, the best-performing drug-like compound highlighted by the screening was tested to evaluate its ability to revert other phenotypes in *GBA-N370S* lines.

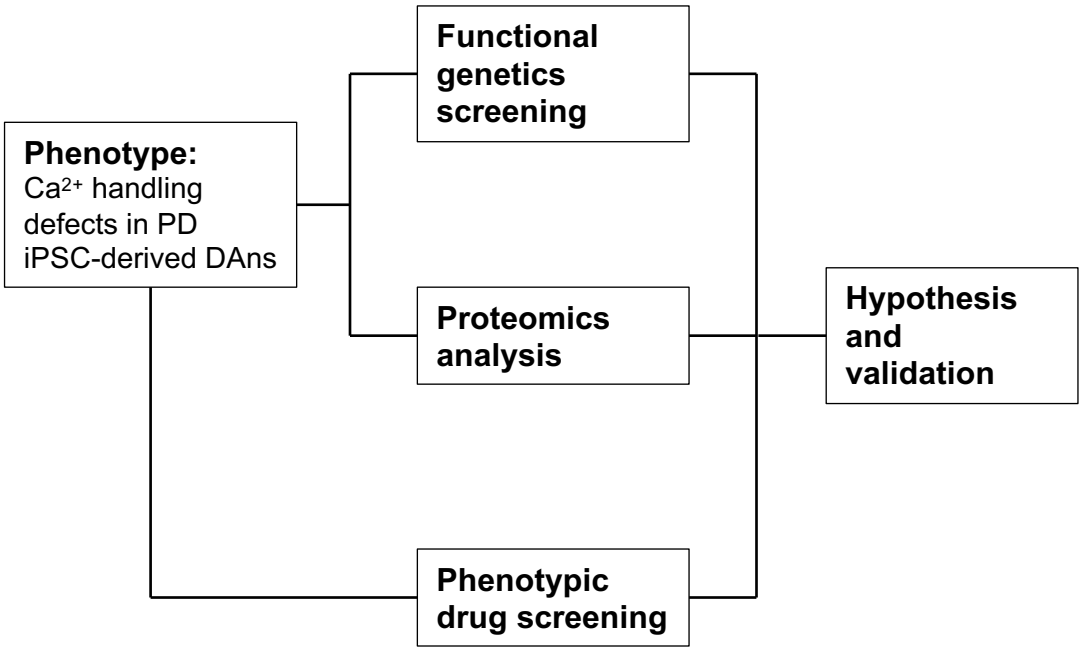


Figure 7.1: Thesis outline

7.1 Main findings and discussion

DAns degeneration in PD has been linked to alterations in mitochondria and ER physiology, the two main stores of Ca^{2+} within the cell. In the ER, Ca^{2+}-binding chaperones allow correct protein folding; therefore, alterations in Ca^{2+} levels may jeopardise proteostasis maintenance. In the mitochondria, Ca^{2+} is required for the correct functioning of the TCA cycle and therefore Ca^{2+} levels may be linked to the energy status of the cells. In addition, DAns require continuous Ca^{2+} influx to support dopamine release and these continuous Ca^{2+} oscillations, may make DAns very sensitive to alterations in Ca^{2+} homeostasis. Therefore, Ca^{2+} signalling and dynamics in the cells have drawn the attention of researchers in the field of PD. Therefore, in this thesis, I investigated the potential role of intracellular Ca^{2+} handling in Parkinson's disease using DAn cultures derived from patients harbouring the mutations *SNCA*-Trp and *GBA-N370S*. iPSC-derived DAns, therefore, offer the opportunity to culture in a dish the very same neurons that degenerate in the brains of PD patients. However, this technology also has some drawbacks. One of particular relevance for this thesis is that the small molecule-based protocol used in this thesis, generates a mixed neuronal culture where only about 60% of the cell population is TH+. Therefore, one needs to keep in mind that it is possible that observations made in these cultures may be influenced by TH- cells.

To probe Ca^{2+} dynamics, I employed the ionophore ionomycin to release Ca^{2+} from intracellular Ca^{2+} stores in conjunction with Fura-2 AM to monitor gross changes in Ca^{2+} dynamics, GECI entrapped in the ER and the mitochondria (GCEPIA*er* and RGECO*mt* respectively) to trace back the source of the defect in DAns.

I observed that *SNCA*-Trp, *SNCA-A53T* and *GBA-N370S* iPSC-derived DAns display a smaller cytoplasmatic Ca^{2+} wave upon ionomycin stimulation in a Fura-2 AM-based assay. In addition, I observed that *SNCA*-Trp and *GBA-N370S* iPSC-

derived DAns release less ER Ca^{2+} in response to ionomycin in a GCEPIA*er*-based assay. The reduced Ca^{2+} release from the ER is also accompanied by reduced Ca^{2+} uptake into the mitochondria as demonstrated in a RGECO*mt*-based assay.

I believe that the origin of these observations there might be a defect in the intracellular Ca^{2+} replenishment.

SOCE is initiated by STIM proteins upon ER Ca^{2+} depletion; when ER Ca^{2+} levels are low, these proteins are activated and activate the Orai Ca^{2+} channels on the plasma membrane which can create a large Ca^{2+} wave in the cytoplasm of the cell, and said Ca^{2+} can then be pumped back into the ER by SERCA to replenish ER Ca^{2+} levels.

Recently it has been suggested that SERCA pumps might be dysfunctional in PD [Solana-Manrique et al., 2021]. SERCA pumps are transmembrane proteins and are regulated by the composition of the membrane; in particular, phosphatidylcholine and phosphatidylethanolamine have been demonstrated to modulate SERCA function and therefore their levels can influence ER Ca^{2+} levels [Fu et al., 2011]. In Chapter 6, I have shown that phosphatidylcholine and phosphatidylethanolamine levels are altered in *GBA-N370S* iPSC-derived DAns and their levels are rescued by FASN inhibitor 1. It is possible that this lipidic alteration might be at least partially responsible for the decreased ER Ca^{2+} content. In order to confirm this hypothesis, it could be interesting to measure SERCA enzymatic activity to see if it is decreased. It would also be interesting to use positive modulators of SERCA such as CDN1163 to see if they could rescue the Ca^{2+} handling phenotypes in PD patients lines.

However, I believe that SERCA pump inhibition alone may not be sufficient to cause all the Ca^{2+} dynamics phenotypes observed in the patients cells. In Chapter

4, I used functional genetics to gain insight into the role of several Ca^{2+} regulating genes in ionomycin-induced Ca^{2+} dynamics. In the preliminary screening carried out and described in Chapter 4, I observed that knock-down of SERCA was associated with an increased cytoplasmic Ca^{2+} transient upon ionomycin stimulation. It is possible that in cells where SERCA had been knocked-down, stimulation of Ca^{2+} release from the ER may be followed by SOCE, and – because of the knock-down – also by a slow refilling of the ER causing a prolonged and more intense cytoplasmic Ca^{2+} transient. In addition, it is possible that in the presence of functional SOCE, it is possible that eventually the ER Ca^{2+} would be slowly replenished, even by less active SERCA.

From the functional genetics experiment in Chapter 4, I also observed that MCU knock-down was associated with decreased cytoplasmic Ca^{2+} transient. Interestingly, MCU is a Ca^{2+} uniporter located on the IMM and is responsible for Ca^{2+} entry into the mitochondrial matrix. In the presence of physiological concentrations of extracellular Ca^{2+}, it has been demonstrated that MCU is necessary for SOCE and that MCU knock-down reduced SOCE Ca^{2+} current [Samanta et al., 2019]. It is possible that SOCE might also be dysfunctional in PD lines. Intriguingly, *PLA2G6* or *PARK14* has been demonstrated to be a crucial regulator of SOCE and deficiency in PLA2G6 has been associated with decreased ER Ca^{2+}in human primary skin fibroblasts from patients with idiopathic PD and with *PLA2G6*-PD mutations [Zhou et al., 2016].

It is possible that SOCE might be altered in iPSC-derived DAns from PD patients and this alteration might be due to alterations in MCU activity. This hypothesis fits with the observation that iPSC-derived DAns from PD patients display decreased mitochondrial Ca^{2+} uptake. However, another intriguing hypothesis that fits with the mitochondrial Ca^{2+} observation is that MAMs might be dysfunctional in PD lines and this fact could cause a decrease in the intensity of the Ca^{2+} puffs

needed by MCU to transfer Ca^{2+} into the mitochondrial matrix.

MAMs dysfunction has been associated to PD in several studies (see Section 1.3.6). In addition, data collected in the Laboratory by Dr Nora Bengoa-Vergniory suggests that MAMs in *SNCA*-Trp might be slightly more distant than in controls.

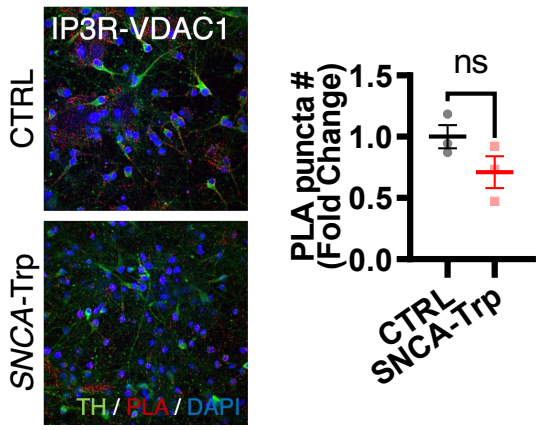


Figure 7.2: Proximity ligation assay showing the interaction between MAMs proteins IP3R and VDAC1

Data courtesy of Dr Nora Bengoa-Vergniory.

One of the first functions of the MAMs to be discovered was their involvement in lipid biosynthesis [Vance, 1990]. One of the functions of the ER is the metabolism of lipids, for example, anabolism of membrane lipids, such as phosphatidylserine. In Chapter 6, I have shown that *GBA-N370S* DAns display decreased levels of these phospholipids compared to controls. This finding further supports the hypothesis that MAMs might be dysfunctional in PD. It could be possible to compare the lipidomic profile of *SNCA*-Trp and controls in order to verify that lipid biosynthesis in the MAMs is altered in patients harbouring this mutation too.

For these reasons, I decided to employ proximity biotinylation assay to study the proteome of ERM, OMM and MAMs in control and patient lines. In Chapter 5 I showed that this assay might be feasible in iPSC-derived DAns.

It could be possible to further investigate MAMs dysfunction in PD lines with the use of electron microscopy to observe the ultrastructure of this compartment in

controls and patients lines.

Finally, in this thesis, I evaluated the ability of FASN inhibitor 1 – a compound highlighted by a phenotypic screening in iPSC-derived DAns for its ability to increase Ca^{2+} release – to revert other cellular phenotypes. In particular, this drug-like compound shows great potential as it appears to increase ER Ca^{2+} content, decrease ER stress and increase lysosomal GCase activity.

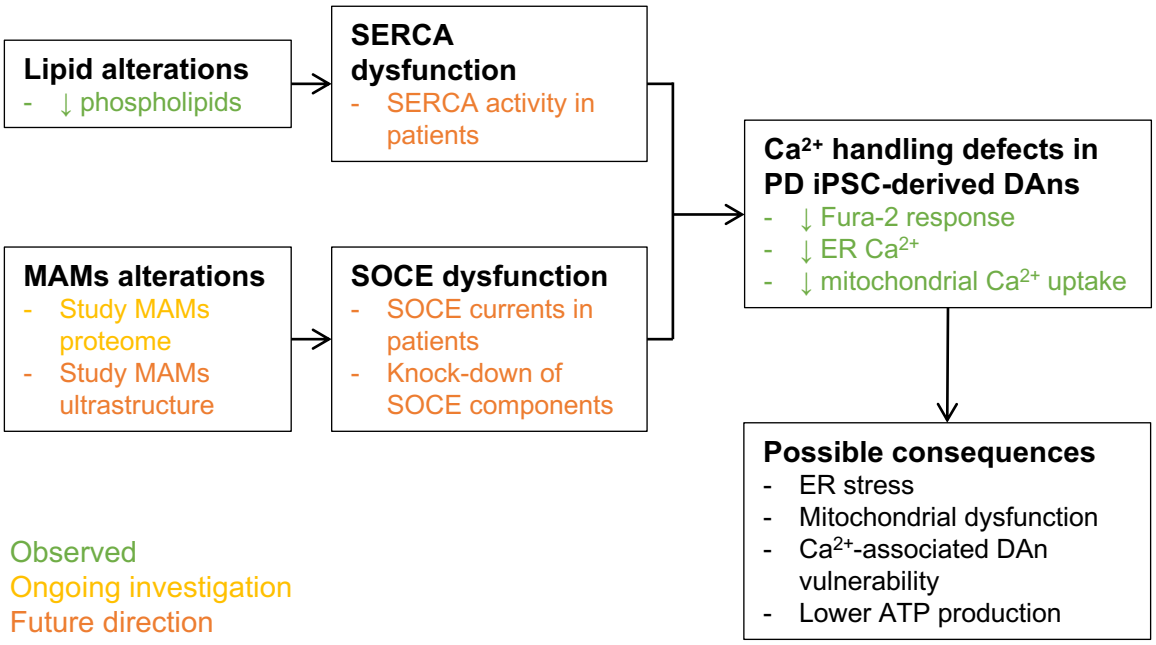


Figure 7.3: Summary of the observations made in this Thesis and future directions

7.2 Conclusions and future directions

The work described in this Thesis has demonstrated that intracellular Ca^{2+} handling might be altered in PD. This finding is particularly interesting in the context of Ca^{2+} dynamics-related hypotheses of preferential vulnerability of SNpc DAns in PD.

Through the use of a functional genomics screening and a phenotypic screening, I developed a working hypothesis on the mechanism at the origin of the Ca^{2+} mishandling in iPSC-derived DAns. Further studies including proteomics will be needed to corroborate this hypothesis. A number of follow-up validation experiments have also been suggested to validate the hypothesis and conclude this work.

This study could take several different avenues. I envision two very different approaches.

One approach could be using super-resolution imaging to observe spontaneous ER Ca^{2+} release and how the puff is uptaken into mitochondria. This approach would require the use of a Ca^{2+} indicator in the cytoplasm to measure the Ca^{2+} puff and a mitochondrial Ca^{2+} indicator to measure the uptake into the mitochondria. Using super-resolution microscopy would allow resolving individual spontaneously occurring Ca^{2+} puffs. Measuring the intensity of the puff would allow the possibility to measure the function of IP3Rs. It would also be possible to measure Ca^{2+} uptake into the mitochondria after such Ca^{2+} release events. Comparing Ca^{2+} puff amplitude and Ca^{2+} uptake into the mitochondria between control and patient-derived cell cultures containing DAns, would allow us to highlight differences between the different genotypes. This experiment would allow us to confirm or disprove the hypothesis that Ca^{2+} handling is altered in DAn cultures derived

from PD patients also in the absence of stimulation.

Another completely different approach would be focused on finding what genes are involved in the modulation of MAMs in human DAns with the ultimate goal to unveil a potential disease mechanism that could be pharmacologically targeted. This experiment would require a whole-genome screening using CRISPRi and CRISPR activation (CRISPRa) methodologies. iPSCs expressing the CRISPRi or the CRISPRa machinery could be differentiated into DAn mixed cultures using the methods described in this thesis. These neurons could be transduced with a whole-genome pooled sgRNA library and a MAM distance fluorescent reporter such as MAMtracker [Sakai et al., 2021] or the FRET version of MERLIN [Hertlein et al., 2019]. It could be possible to harvest the obtained cultures and stain them for TH, then proceed to flow sort them to select the TH+ cells only and to measure the MAM distance. It could be possible to select the cells where the MAM distance was decreased or increased and then sequence them to find out what gene they were knocking down. This approach would provide an unbiassed list of MAM modulators in DAns and could be used to draw mechanistic insights on the disease and highlight potential therapeutic targets.

Bibliography

[Agarwal et al., 2020] Agarwal, D., Sandor, C., Volpato, V., Caffrey, T. M., Monzón-Sandoval, J., Bowden, R., Alegre-Abarrategui, J., Wade-Martins, R., and Webber, C. (2020). A single-cell atlas of the human substantia nigra reveals cell-specific pathways associated with neurological disorders. *Nature Communications*, 11(1).

[Alfahel-Kakunda and Silverman, 1997] Alfahel-Kakunda, A. and Silverman, W. F. (1997). Calcium-binding proteins in the substantia nigra and ventral tegmental area during development: correlation with dopaminergic compartmentalization. *Developmental Brain Research*, 103(1):9–20.

[Beevers et al., 2017] Beevers, J. E., Lai, M. C., Collins, E., Booth, H. D., Zambon, F., Parkkinen, L., Vowles, J., Cowley, S. A., Wade-Martins, R., and Caffrey, T. M. (2017). MAPT genetic variation and neuronal maturity alter isoform expression affecting axonal transport in iPSC-derived dopamine neurons. *Stem Cell Reports*, 9(2):587–599.

[Benkert et al., 2019] Benkert, J., Hess, S., Roy, S., Beccano-Kelly, D., Wiederspohn, N., Duda, J., Simons, C., Patil, K., Gaifullina, A., Mannal, N., Dragicevic, E., Spaich, D., Müller, S., Nemeth, J., Hollmann, H., Deuter, N., Mousba, Y., Kubisch, C., Poetschke, C., Striessnig, J., Pongs, O., Schneider, T., Wade-Martins, R., Patel, S., Parlato, R., Frank, T., Kloppenburg, P., and Liss, B. (2019). Cav2.3 channels contribute to dopaminergic neuron loss in a model of parkinson's disease. *Nature Communications*, 10(1).

[Bootman et al., 2018] Bootman, M. D., Chehab, T., Bultynck, G., Parys, J. B., and Rietdorf, K. (2018). The regulation of autophagy by calcium signals: Do we have a consensus? *Cell Calcium*, 70:32–46.

[Braak et al., 2003] Braak, H., Tredici, K. D., Rüb, U., de Vos, R. A., Steur, E. N. J., and Braak, E. (2003). Staging of brain pathology related to sporadic parkinson's disease. *Neurobiology of Aging*, 24(2):197–211.

[Brimblecombe et al., 2015] Brimblecombe, K. R., Gracie, C. J., Platt, N. J., and Cragg, S. J. (2015). Gating of dopamine transmission by calcium and axonal n-, q-, t- and l-type voltage-gated calcium channels differs between striatal domains. *The Journal of Physiology*, 593(4):929–946.

[Brini et al., 2012] Brini, M., Calì, T., Ottolini, D., and Carafoli, E. (2012). Intracellular calcium homeostasis and signaling. In *Metal Ions in Life Sciences*, pages 119–168. Springer Netherlands.

[Brini and Carafoli, 2010] Brini, M. and Carafoli, E. (2010). The plasma membrane Ca^{2+} ATPase and the plasma membrane sodium calcium exchanger cooperate in the regulation of cell calcium. *Cold Spring Harbor Perspectives in Biology*, 3(2):a004168–a004168.

[Burbulla et al., 2017] Burbulla, L. F., Song, P., Mazzulli, J. R., Zampese, E., Wong, Y. C., Jeon, S., Santos, D. P., Blanz, J., Obermaier, C. D., Strojny, C., Savas, J. N., Kiskinis, E., Zhuang, X., Krüger, R., Surmeier, D. J., and Krainc, D. (2017). Dopamine oxidation mediates mitochondrial and lysosomal dysfunction in parkinson's disease. *Science*, 357(6357):1255–1261.

[Byers et al., 2011] Byers, B., Cord, B., Nguyen, H. N., Schüle, B., Fenno, L., Lee, P. C., Deisseroth, K., Langston, J. W., Pera, R. R., and Palmer, T. D. (2011). SNCA triplication parkinson's patient's iPSC-derived DA neurons accumulate α-synuclein and are susceptible to oxidative stress. *PLoS One*, 6(11):e26159.

[Caiazza et al., 2020] Caiazza, M. C., Lang, C., and Wade-Martins, R. (2020). What we can learn from iPSC-derived cellular models of parkinson's disease. In *Progress in Brain Research*, pages 3–25. Elsevier.

[Calì et al., 2019] Calì, T., Ottolini, D., Vicario, M., Catoni, C., Vallese, F., Cieri, D., Barazzuol, L., and Brini, M. (2019). splitGFP technology reveals dose-dependent ER-mitochondria interface modulation by α-synuclein a53t and a30p mutants. *Cells*, 8(9):1072.

[Calì et al., 2012] Calì, T., Ottolini, D., Negro, A., and Brini, M. (2012). α-synuclein controls mitochondrial calcium homeostasis by enhancing endoplasmic reticulum-mitochondria interactions. *Journal of Biological Chemistry*, 287(22):17914–17929.

[Camara et al., 2017] Camara, A. K. S., Zhou, Y., Wen, P.-C., Tajkhorshid, E., and Kwok, W.-M. (2017). Mitochondrial VDAC1: A key gatekeeper as potential therapeutic target. *Frontiers in Physiology*, 8.

[Chambers et al., 2009] Chambers, S. M., Fasano, C. A., Papapetrou, E. P., Tomishima, M., Sadelain, M., and Studer, L. (2009). Highly efficient neural conversion of human ES and iPS cells by dual inhibition of SMAD signaling. *Nat. Biotechnol.*, 27(3):275–280.

[Chandrasekhar et al., 2016] Chandrasekhar, R., Alzayady, K. J., Wagner, L. E., and Yule, D. I. (2016). Unique regulatory properties of heterotetrameric inositol 1, 4, 5-trisphosphate receptors revealed by studying concatenated receptor constructs. *Journal of Biological Chemistry*, 291(10):4846–4860.

[Chang et al., 2009] Chang, C.-W., Lai, Y.-S., Pawlik, K. M., Liu, K., Sun, C.-W., Li, C., Schoeb, T. R., and Townes, T. M. (2009). Polycistronic lentiviral vector for "hit and run" reprogramming of adult skin fibroblasts to induced pluripotent stem cells. *Stem Cells*, 27(5):1042–1049.

[Cho et al., 2020] Cho, K. F., Branon, T. C., Rajeev, S., Svinkina, T., Udeshi, N. D., Thoudam, T., Kwak, C., Rhee, H.-W., Lee, I.-K., Carr, S. A., and Ting, A. Y. (2020). Split-TurboID enables contact-dependent proximity labeling in cells. *Proceedings of the National Academy of Sciences*, 117(22):12143–12154.

[Chung et al., 2013] Chung, C. Y., Khurana, V., Auluck, P. K., Tardiff, D. F., Mazzulli, J. R., Soldner, F., Baru, V., Lou, Y., Freyzon, Y., Cho, S., Mungenast, A. E., Muffat, J., Mitalipova, M., Pluth, M. D., Jui, N. T., Schüle, B., Lippard, S. J., Tsai, L.-H., Krainc, D., Buchwald, S. L., Jaenisch, R., and Lindquist, S. (2013). Identification and rescue of α-synuclein toxicity in parkinson patient-derived neurons. *Science*, 342(6161):983–987.

[Clapham, 2007] Clapham, D. E. (2007). Calcium signaling. *Cell*, 131(6):1047–1058.

[Colla, 2019] Colla, E. (2019). Linking the endoplasmic reticulum to parkinson's disease and alpha-synucleinopathy. *Frontiers in Neuroscience*, 13.

[Connor-Robson et al., 2019] Connor-Robson, N., Booth, H., Martin, J. G., Gao, B., Li, K., Doig, N., Vowles, J., Browne, C., Klinger, L., Juhasz, P., Klein, C., Cowley, S. A., Bolam, P., Hirst, W., and Wade-Martins, R. (2019). An integrated transcriptomics and proteomics analysis reveals functional endocytic dysregulation caused by mutations in LRRK2. *Neurobiol. Dis.*, 127:512–526.

[Cooney et al., 2002] Cooney, J. R., Hurlburt, J. L., Selig, D. K., Harris, K. M., and Fiala, J. C. (2002). Endosomal compartments serve multiple hippocampal dendritic spines from a widespread rather than a local store of recycling membrane. *The Journal of Neuroscience*, 22(6):2215–2224.

[Cooper et al., 2012] Cooper, O., Seo, H., Andrabi, S., Guardia-Laguarta, C., Graziotto, J., Sundberg, M., McLean, J. R., Carrillo-Reid, L., Xie, Z., Osborn, T., Hargus, G., Deleidi, M., Lawson, T., Bogetofte, H., Perez-Torres, E., Clark, L., Moskowitz, C., Mazzulli, J., Chen, L., Volpicelli-Daley, L., Romero, N., Jiang, H., Uitti, R. J., Huang, Z., Opala, G., Scarffe, L. A., Dawson, V. L., Klein, C., Feng, J., Ross, O. A., Trojanowski, J. Q., Lee, V. M.-Y., Marder, K., Surmeier, D. J., Wszolek, Z. K., Przedborski, S., Krainc, D., Dawson, T. M., and Isacson, O. (2012). Pharmacological rescue of mitochondrial deficits in iPSC-derived neural cells from patients with familial parkinson's disease. *Science Translational Medicine*, 4(141).

[Csordaś et al., 2006] Csordaś, G., Renken, C., Vaŕnai, P., Walter, L., Weaver, D., Buttle, K. F., Balla, T., Mannella, C. A., and Hajnoćzky, G. (2006). Structural

and functional features and significance of the physical linkage between ER and mitochondria. *Journal of Cell Biology*, 174(7):915–921.

[Csordas et al., 2018] Csordas, G., Weaver, D., and Hajnoczky, G. (2018). Endoplasmic reticulum–mitochondrial contactology: Structure and signaling functions. *Trends in Cell Biology*, 28(7):523–540.

[Dahl, 2017] Dahl, R. (2017). A new target for parkinson's disease: Small molecule SERCA activator CDN1163 ameliorates dyskinesia in 6-OHDA-lesioned rats. *Bioorganic & Medicinal Chemistry*, 25(1):53–57.

[Dopeso-Reyes et al., 2014] Dopeso-Reyes, I. G., Rico, A. J., Roda, E., Sierra, S., Pignataro, D., Lanz, M., Sucunza, D., Chang-Azancot, L., and Lanciego, J. L. (2014). Calbindin content and differential vulnerability of midbrain efferent dopaminergic neurons in macaques. *Frontiers in Neuroanatomy*, 8.

[Dorsey and Bloem, 2018] Dorsey, E. R. and Bloem, B. R. (2018). The parkinson pandemic—a call to action. *JAMA Neurology*, 75(1):9.

[Duda et al., 2016] Duda, J., Pötschke, C., and Liss, B. (2016). Converging roles of ion channels, calcium, metabolic stress, and activity pattern of *Substantia nigra* dopaminergic neurons in health and parkinson's disease. *Journal of Neurochemistry*, 139(S1):156–178.

[Díaz-García et al., 2021] Díaz-García, C. M., Meyer, D. J., Nathwani, N., Rahman, M., Martínez-François, J. R., and Yellen, G. (2021). The distinct roles of calcium in rapid control of neuronal glycolysis and the tricarboxylic acid cycle. *eLife*, 10:e64821.

[Erustes et al., 2021] Erustes, A. G., D'Eletto, M., Guarache, G. C., Ureshino, R. P., Bincoletto, C., Pereira, G. J. S., Piacentini, M., and Smaili, S. S. (2021). Overexpression of α-synuclein inhibits mitochondrial Ca^{2+} trafficking between the endoplasmic reticulum and mitochondria through MAMs by altering the GRP75-IP3r interaction. *Journal of Neuroscience Research*, 99(11):2932–2947.

[Fedele et al., 2017] Fedele, S., Collo, G., Behr, K., Bischofberger, J., Müller, S., Kunath, T., Christensen, K., Gündner, A. L., Graf, M., Jagasia, R., and Taylor, V. (2017). Expansion of human midbrain floor plate progenitors from induced pluripotent stem cells increases dopaminergic neuron differentiation potential. *Scientific Reports*, 7(1).

[Fernandes et al., 2016] Fernandes, H. J. R., Hartfield, E. M., Christian, H. C., Emmanoulidou, E., Zheng, Y., Booth, H., Bogetofte, H., Lang, C., Ryan, B. J., Sardi, S. P., Badger, J., Vowles, J., Evetts, S., Tofaris, G. K., Vekrellis, K., Talbot, K., Hu, M. T., James, W., Cowley, S. A., and Wade-Martins, R. (2016). ER stress and autophagic perturbations lead to elevated extracellular α-synuclein in GBA-N370S parkinson's iPSC-derived dopamine neurons. *Stem Cell Reports*, 6(3):342–356.

[Fernandopulle et al., 2018] Fernandopulle, M. S., Prestil, R., Grunseich, C., Wang, C., Gan, L., and Ward, M. E. (2018). Transcription factor-mediated differentiation of human iPSCs into neurons. *Current Protocols in Cell Biology*, 79(1):e51.

[Foehring et al., 2009] Foehring, R. C., Zhang, X. F., Lee, J., and Callaway, J. C. (2009). Endogenous Calcium Buffering Capacity of Substantia Nigral Dopamine Neurons. *Journal of Neurophysiology*, 102(4):2326–2333.

[Fortin, 2004] Fortin, D. L. (2004). Lipid rafts mediate the synaptic localization of α-synuclein. *Journal of Neuroscience*, 24(30):6715–6723.

[Francardo, 2014] Francardo, V. (2014). Sigma-1 receptor: a potential new target for parkinson's disease? *Neural Regeneration Research*, 9(21):1882.

[Frankenfield et al., 2020] Frankenfield, A. M., Fernandopulle, M. S., Hasan, S., Ward, M. E., and Hao, L. (2020). Development and comparative evaluation of endolysosomal proximity labeling-based proteomic methods in human iPSC-derived neurons. *Analytical Chemistry*, 92(23):15437–15444.

[Fu et al., 2011] Fu, S., Yang, L., Li, P., Hofmann, O., Dicker, L., Hide, W., Lin, X., Watkins, S. M., Ivanov, A. R., and Hotamisligil, G. S. (2011). Aberrant lipid metabolism disrupts calcium homeostasis causing liver endoplasmic reticulum stress in obesity. *Nature*, 473(7348):528–531.

[Fusaki et al., 2009] Fusaki, N., Ban, H., Nishiyama, A., Saeki, K., and Hasegawa, M. (2009). Efficient induction of transgene-free human pluripotent stem cells using a vector based on sendai virus, an RNA virus that does not integrate into the host genome. *Proceedings of the Japan Academy, Series B*, 85(8):348–362.

[Giguère et al., 2018] Giguère, N., Nanni, S. B., and Trudeau, L.-E. (2018). On cell loss and selective vulnerability of neuronal populations in parkinson's disease. *Frontiers in Neurology*, 9.

[Gilbert et al., 2013] Gilbert, L., Larson, M., Morsut, L., Liu, Z., Brar, G., Torres, S., Stern-Ginossar, N., Brandman, O., Whitehead, E., Doudna, J., Lim, W., Weissman, J., and Qi, L. (2013). CRISPR-Mediated Modular RNA-Guided Regulation of Transcription in Eukaryotes. *Cell*, 154(2):442–451.

[Gómez-Suaga et al., 2011] Gómez-Suaga, P., Luzón-Toro, B., Churamani, D., Zhang, L., Bloor-Young, D., Patel, S., Woodman, P. G., Churchill, G. C., and Hilfiker, S. (2011). Leucine-rich repeat kinase 2 regulates autophagy through a calcium-dependent pathway involving NAADP. *Human Molecular Genetics*, 21(3):511–525.

[Gonzalez-Sanchez et al., 2017] Gonzalez-Sanchez, P., Pla-Martin, D., Martinez-Valero, P., Rueda, C. B., Calpena, E., del Arco, A., Palau, F., and Satrustegui, J. (2017). CMT-linked loss-of-function mutations in GDAP1 impair store-operated Ca^{2+} entry-stimulated respiration. *Scientific Reports*, 7(1).

[González-Hernández and Rodríguez, 2000] González-Hernández, T. and Rodríguez, M. (2000). Compartmental organization and chemical profile of dopaminergic and GABAergic neurons in the substantia nigra of the rat. *The Journal of Comparative Neurology*, 421(1):107–135.

[Grassi et al., 2018] Grassi, D., Howard, S., Zhou, M., Diaz-Perez, N., Urban, N. T., Guerrero-Given, D., Kamasawa, N., Volpicelli-Daley, L. A., LoGrasso, P., and Lasmézas, C. I. (2018). Identification of a highly neurotoxic α-synuclein species inducing mitochondrial damage and mitophagy in parkinson's disease. *Proceedings of the National Academy of Sciences*, 115(11).

[Grynkiewicz et al., 1985] Grynkiewicz, G., Poenie, M., and Tsien, R. Y. (1985). A new generation of ca^{2+} indicators with greatly improved fluorescence properties. *Journal of Biological Chemistry*, 260(6):3440–3450.

[Guardia-Laguarta et al., 2013] Guardia-Laguarta, C., Area-Gomez, E., Rub, C., Liu, Y., Magrane, J., Becker, D., Voos, W., Schon, E. A., and Przedborski, S. (2013). α-synuclein is localized to mitochondria-associated ER membranes. *Journal of Neuroscience*, 34(1):249–259.

[Gómez-Suaga et al., 2018] Gómez-Suaga, P., Bravo-San Pedro, J. M., González-Polo, R. A., Fuentes, J. M., and Niso-Santano, M. (2018). ER–mitochondria signaling in Parkinson's disease. *Cell Death & Disease*, 9(3):337.

[Görlach et al., 2015] Görlach, A., Bertram, K., Hudecova, S., and Krizanova, O. (2015). Calcium and ROS: A mutual interplay. *Redox Biology*, 6:260–271.

[Hamasaki et al., 2013] Hamasaki, M., Furuta, N., Matsuda, A., Nezu, A., Yamamoto, A., Fujita, N., Oomori, H., Noda, T., Haraguchi, T., Hiraoka, Y., Amano, A., and Yoshimori, T. (2013). Autophagosomes form at ER-mitochondria contact sites. *Nature*, 495(7441):389–393.

[Hayashi and Fujimoto, 2010] Hayashi, T. and Fujimoto, M. (2010). Detergent-resistant microdomains determine the localization of σ-1 receptors to the endoplasmic reticulum-mitochondria junction. *Molecular Pharmacology*, 77(4):517–528.

[Hayashi and Su, 2007] Hayashi, T. and Su, T.-P. (2007). Sigma-1 receptor chaperones at the ER- mitochondrion interface regulate Ca^{2+} signaling and cell survival. *Cell*, 131(3):596–610.

[Healy et al., 2008] Healy, D. G., Falchi, M., O'Sullivan, S. S., Bonifati, V., Durr, A., Bressman, S., Brice, A., Aasly, J., Zabetian, C. P., Goldwurm, S., Ferreira, J. J., Tolosa, E., Kay, D. M., Klein, C., Williams, D. R., Marras, C., Lang, A. E., Wszolek, Z. K., Berciano, J., Schapira, A. H., Lynch, T., Bhatia, K. P., Gasser, T., Lees, A. J., and Wood, N. W. (2008). Phenotype, genotype, and worldwide genetic penetrance of LRRK2-associated parkinson's disease: a case-control study. *The Lancet Neurology*, 7(7):583–590.

[Hernandez et al., 2016] Hernandez, D. G., Reed, X., and Singleton, A. B. (2016). Genetics in parkinson disease: Mendelian versus non-mendelian inheritance. *Journal of Neurochemistry*, 139:59–74.

[Hertlein et al., 2019] Hertlein, V., Flores-Romero, H., Das, K. K., Fischer, S., Heunemann, M., Calleja-Felipe, M., Knafo, S., Hipp, K., Harter, K., Fitzgerald, J. C., and García-Sáez, A. J. (2019). MERLIN: a novel BRET-based proximity biosensor for studying mitochondria–ER contact sites. *Life Science Alliance*, 3(1):e201900600.

[Higo et al., 2005] Higo, T., Hattori, M., Nakamura, T., Natsume, T., Michikawa, T., and Mikoshiba, K. (2005). Subtype-specific and ER lumenal environment-dependent regulation of inositol 1, 4, 5-trisphosphate receptor type 1 by ERp44. *Cell*, 120(1):85–98.

[Horlbeck et al., 2016] Horlbeck, M. A., Gilbert, L. A., Villalta, J. E., Adamson, B., Pak, R. A., Chen, Y., Fields, A. P., Park, C. Y., Corn, J. E., Kampmann, M., and Weissman, J. S. (2016). Compact and highly active next-generation libraries for CRISPR-mediated gene repression and activation. *eLife*, 5.

[Hou et al., 2013] Hou, P., Li, Y., Zhang, X., Liu, C., Guan, J., Li, H., Zhao, T., Ye, J., Yang, W., Liu, K., Ge, J., Xu, J., Zhang, Q., Zhao, Y., and Deng, H. (2013). Pluripotent stem cells induced from mouse somatic cells by small-molecule compounds. *Science*, 341(6146):651–654.

[Hou et al., 2020] Hou, X., Watzlawik, J. O., Fiesel, F. C., and Springer, W. (2020). Autophagy in parkinson's disease. *Journal of Molecular Biology*, 432(8):2651–2672.

[Hsieh et al., 2016] Hsieh, C.-H., Shaltouki, A., Gonzalez, A. E., Bettencourt da Cruz, A., Burbulla, L. F., St Lawrence, E., Schüle, B., Krainc, D., Palmer, T. D., and Wang, X. (2016). Functional impairment in miro degradation and mitophagy is a shared feature in familial and sporadic parkinson's disease. *Cell Stem Cell*, 19(6):709–724.

[Hung et al., 2017] Hung, V., Lam, S. S., Udeshi, N. D., Svinkina, T., Guzman, G., Mootha, V. K., Carr, S. A., and Ting, A. Y. (2017). Proteomic mapping of cytosol-facing outer mitochondrial and ER membranes in living human cells by proximity biotinylation. *eLife*, 6.

[Hung et al., 2016] Hung, V., Udeshi, N. D., Lam, S. S., Loh, K. H., Cox, K. J., Pedram, K., Carr, S. A., and Ting, A. Y. (2016). Spatially resolved proteomic mapping in living cells with the engineered peroxidase APEX2. *Nature Protocols*, 11(3):456–475.

[Hurley et al., 2013] Hurley, M. J., Brandon, B., Gentleman, S. M., and Dexter, D. T. (2013). Parkinson's disease is associated with altered expression of CaV1 channels and calcium-binding proteins. *Brain*, 136(7):2077–2097.

[Isacson and Deacon, 1997] Isacson, O. and Deacon, T. (1997). Neural transplantation studies reveal the brain's capacity for continuous reconstruction. *Trends Neurosci.*, 20(10):477–482.

[Jankovic, 2008] Jankovic, J. (2008). Parkinson's disease: clinical features and diagnosis. *Journal of Neurology, Neurosurgery and Psychiatry*, 79(4):368–376.

[John et al., 1998] John, L. M., Lechleiter, J. D., and Camacho, P. (1998). Differential modulation of SERCA2 isoforms by calreticulin. *Journal of Cell Biology*, 142(4):963–973.

[Kaji et al., 2009] Kaji, K., Norrby, K., Paca, A., Mileikovsky, M., Mohseni, P., and Woltjen, K. (2009). Virus-free induction of pluripotency and subsequent excision of reprogramming factors. *Nature*, 458(7239):771–775.

[Kamata et al., 2006] Kamata, A., Takeuchi, Y., and Fukunaga, K. (2006). Identification of the isoforms of Ca^{2+}/calmodulin-dependent protein kinase II and expression of brain-derived neurotrophic factor mRNAs in the substantia nigra. *Journal of Neurochemistry*, 96(1):195–203.

[Kamath et al., 2022] Kamath, T., Abdulraouf, A., Burris, S. J., Langlieb, J., Gazestani, V., Nadaf, N. M., Balderrama, K., Vanderburg, C., and Macosko, E. Z. (2022). Single-cell genomic profiling of human dopamine neurons identifies a population that selectively degenerates in parkinson's disease. *Nature Neuroscience*, 25(5):588–595.

[Kampmann, 2018] Kampmann, M. (2018). CRISPRi and CRISPRa Screens in Mammalian Cells for Precision Biology and Medicine. *ACS Chemical Biology*, 13(2):406–416.

[Kim et al., 2009] Kim, D., Kim, C.-H., Moon, J.-I., Chung, Y.-G., Chang, M.-Y., Han, B.-S., Ko, S., Yang, E., Cha, K. Y., Lanza, R., and Kim, K.-S. (2009). Generation of human induced pluripotent stem cells by direct delivery of reprogramming proteins. *Cell Stem Cell*, 4(6):472–476.

[Kim and Catterall, 1997] Kim, D. K. and Catterall, W. A. (1997). Ca^{2+}-dependent and -independent interactions of the isoforms of the α1a subunit of brain Ca^{2+} channels with presynaptic snare proteins. *Proceedings of the National Academy of Sciences*, 94(26):14782–14786.

[Korecka et al., 2019] Korecka, J. A., Talbot, S., Osborn, T. M., de Leeuw, S. M., Levy, S. A., Ferrari, E. J., Moskites, A., Atkinson, E., Jodelka, F. M., Hinrich, A. J., Hastings, M. L., Woolf, C. J., Hallett, P. J., and Isacson, O. (2019). Neurite collapse and altered ER ca^{2+} control in human parkinson disease patient iPSC-derived neurons with LRRK2 g2019s mutation. *Stem Cell Reports*, 12(1):29–41.

[Kriks et al., 2011] Kriks, S., Shim, J.-W., Piao, J., Ganat, Y. M., Wakeman, D. R., Xie, Z., Carrillo-Reid, L., Auyeung, G., Antonacci, C., Buch, A., Yang, L., Beal,

M. F., Surmeier, D. J., Kordower, J. H., Tabar, V., and Studer, L. (2011). Dopamine neurons derived from human ES cells efficiently engraft in animal models of parkinson's disease. *Nature*, 480(7378):547–551.

[Kumar et al., 2011] Kumar, K., Djarmati-Westenberger, A., and Grünewald, A. (2011). Genetics of parkinson's disease. *Seminars in Neurology*, 31(05):433–440.

[Kuzuhara et al., 1988] Kuzuhara, S., Mori, H., Izumiyama, N., Yoshimura, M., and Ihara, Y. (1988). Lewy bodies are ubiquitinated. *Acta Neuropathologica*, 75(4):345–353.

[Lang et al., 2019] Lang, C., Campbell, K. R., Ryan, B. J., Carling, P., Attar, M., Vowles, J., Perestenko, O. V., Bowden, R., Baig, F., Kasten, M., Hu, M. T., Cowley, S. A., Webber, C., and Wade-Martins, R. (2019). Single-cell sequencing of iPSC-dopamine neurons reconstructs disease progression and identifies HDAC4 as a regulator of parkinson cell phenotypes. *Cell Stem Cell*, 24(1):93–106.e6.

[Lanner et al., 2010] Lanner, J. T., Georgiou, D. K., Joshi, A. D., and Hamilton, S. L. (2010). Ryanodine receptors: Structure, expression, molecular details, and function in calcium release. *Cold Spring Harbor Perspectives in Biology*, 2(11):a003996–a003996.

[Lautenschläger et al., 2018] Lautenschläger, J., Stephens, A. D., Fusco, G., Ströhl, F., Curry, N., Zacharopoulou, M., Michel, C. H., Laine, R., Nespovitaya, N., Fantham, M., Pinotsi, D., Zago, W., Fraser, P., Tandon, A., George-Hyslop, P. S., Rees, E., Phillips, J. J., Simone, A. D., Kaminski, C. F., and Schierle, G. S. K. (2018). C-terminal calcium binding of α-synuclein modulates synaptic vesicle interaction. *Nature Communications*, 9(1).

[Li et al., 2020] Li, J., Han, S., Li, H., Udeshi, N. D., Svinkina, T., Mani, D., Xu, C., Guajardo, R., Xie, Q., Li, T., Luginbuhl, D. J., Wu, B., McLaughlin, C. N., Xie, A., Kaewsapsak, P., Quake, S. R., Carr, S. A., Ting, A. Y., and Luo, L. (2020). Cell-surface proteomic profiling in the fly brain uncovers wiring regulators. *Cell*, 180(2):373–386.e15.

[Malpartida et al., 2021] Malpartida, A. B., Williamson, M., Narendra, D. P., Wade-Martins, R., and Ryan, B. J. (2021). Mitochondrial dysfunction and mitophagy in parkinson's disease: From mechanism to therapy. *Trends in Biochemical Sciences*, 46(4):329–343.

[Marión and Blasco, 2010] Marión, R. M. and Blasco, M. A. (2010). Telomere rejuvenation during nuclear reprogramming. *Curr. Opin. Genet. Dev.*, 20(2):190–196.

[Mazzulli et al., 2016] Mazzulli, J. R., Zunke, F., Isacson, O., Studer, L., and Krainc, D. (2016). α-Synuclein-induced lysosomal dysfunction occurs through disruptions in protein trafficking in human midbrain synucleinopathy models. *Proc. Natl. Acad. Sci. U. S. A.*, 113(7):1931–1936.

[Medina, 2021] Medina, D. L. (2021). Lysosomal calcium and autophagy. In *International Review of Cell and Molecular Biology*, pages 141–170. Elsevier.

[Modi et al., 2019] Modi, S., López-Doménech, G., Halff, E. F., Covill-Cooke, C., Ivankovic, D., Melandri, D., Arancibia-Cárcamo, I. L., Burden, J. J., Lowe, A. R., and Kittler, J. T. (2019). Miro clusters regulate ER-mitochondria contact sites and link cristae organization to the mitochondrial transport machinery. *Nature Communications*, 10(1).

[Myhill et al., 2008] Myhill, N., Lynes, E. M., Nanji, J. A., Blagoveshchenskaya, A. D., Fei, H., Simmen, K. C., Cooper, T. J., Thomas, G., and Simmen, T. (2008). The subcellular distribution of calnexin is mediated by PACS-2. *Molecular Biology of the Cell*, 19(7):2777–2788.

[Nalls et al., 2019] Nalls, M. A., Blauwendraat, C., Vallerga, C. L., Heilbron, K., Bandres-Ciga, S., Chang, D., Tan, M., Kia, D. A., Noyce, A. J., Xue, A., Bras, J., Young, E., von Coelln, R., Simón-Sánchez, J., Schulte, C., Sharma, M., Krohn, L., Pihlstrøm, L., Siitonen, A., Iwaki, H., Leonard, H., Faghri, F., Gibbs, J. R., Hernandez, D. G., Scholz, S. W., Botia, J. A., Martinez, M., Corvol, J.-C., Lesage, S., Jankovic, J., Shulman, L. M., Sutherland, M., Tienari, P., Majamaa, K., Toft, M., Andreassen, O. A., Bangale, T., Brice, A., Yang, J., Gan-Or, Z., Gasser, T., Heutink, P., Shulman, J. M., Wood, N. W., Hinds, D. A., Hardy, J. A., Morris, H. R., Gratten, J., Visscher, P. M., Graham, R. R., Singleton, A. B., Adarmes-Gómez, A. D., Aguilar, M., Aitkulova, A., Akhmetzhanov, V., Alcalay, R. N., Alvarez, I., Alvarez, V., Bandres-Ciga, S., Barrero, F. J., Yarza, J. A. B., Bernal-Bernal, I., Billingsley, K., Blauwendraat, C., Blazquez, M., Bonilla-Toribio, M., Botía, J. A., Boungiorno, M. T., Bras, J., Brice, A., Brockmann, K., Bubb, V., Buiza-Rueda, D., Cámara, A., Carrillo, F., Carrión-Claro, M., Cerdan, D., Chelban, V., Clarimón, J., Clarke, C., Compta, Y., Cookson, M. R., Corvol, J.-C., Craig, D. W., Danjou, F., Diez-Fairen, M., Dols-Icardo, O., Duarte, J., Duran, R., Escamilla-Sevilla, F., Escott-Price, V., Ezquerra, M., Faghri, F., Feliz, C., Fernández, M., Fernández-Santiago, R., Finkbeiner, S., Foltynie, T., Gan-Or, Z., Garcia, C., García-Ruiz, P., Gasser, T., Gibbs, J. R., Heredia, M. J. G., Gómez-Garre, P., González, M. M., Gonzalez-Aramburu, I., Guelfi, S., Guerreiro, R., Hardy, J., Hassin-Baer, S., Hernandez, D. G., Heutink, P., Hoenicka, J., Holmans, P., Houlden, H., Infante, J., Iwaki, H., Jesús, S., Jimenez-Escrig, A., Kaishybayeva, G., Kaiyrzhanov, R., Karimova, A., Kia, D. A., Kinghorn, K. J., Koks, S., Krohn, L., Kulisevsky, J., Labrador-Espinosa, M. A., Leonard, H. L., Lesage, S., Lewis, P., Lopez-Sendon, J. L., Lovering, R., Lubbe, S., Lungu, C., Macias, D., Majamaa, K., Manzoni, C., Marín, J., Marinus, J., Marti, M. J., Martinez, M., Torres, I. M., Martínez-Castrillo, J. C., Mata, M., Mencacci, N. E., del Barrio, C. M., Middlehurst, B., Mínguez,

A., Mir, P., Mok, K. Y., Morris, H. R., Muñoz, E., Nalls, M. A., Narendra, D., Noyce, A. J., Ojo, O. O., Okubadejo, N. U., Pagola, A. G., Pastor, P., Errazquin, F. P., Periñán-Tocino, T., Pihlstrom, L., Plun-Favreau, H., Quinn, J., R'Bibo, L., Reed, X., Rezola, E. M., Rizig, M., Rizzu, P., Robak, L., Rodriguez, A. S., Rouleau, G. A., Ruiz-Martínez, J., Ruz, C., Ryten, M., Sadykova, D., Scholz, S. W., Schreglmann, S., Schulte, C., Sharma, M., Shashkin, C., Shulman, J. M., Sierra, M., Siitonen, A., Simón-Sánchez, J., Singleton, A. B., Suarez-Sanmartin, E., Taba, P., Tabernero, C., Tan, M. X., Tartari, J. P., Tejera-Parrado, C., Toft, M., Tolosa, E., Trabzuni, D., Valldeoriola, F., van Hilten, J. J., Keuren-Jensen, K. V., Vargas-González, L., Vela, L., Vives, F., Williams, N., Wood, N. W., Zharkinbekova, N., Zharmukhanov, Z., Zholdybayeva, E., Zimprich, A., Ylikotila, P., Shulman, L. M., von Coelln, R., Reich, S., Savitt, J., Agee, M., Alipanahi, B., Auton, A., Bell, R. K., Bryc, K., Elson, S. L., Fontanillas, P., Furlotte, N. A., Huber, K. E., Hicks, B., Jewett, E. M., Jiang, Y., Kleinman, A., Lin, K.-H., Litterman, N. K., McCreight, J. C., McIntyre, M. H., McManus, K. F., Mountain, J. L., Noblin, E. S., Northover, C. A., Pitts, S. J., Poznik, G. D., Sathirapongsasuti, J. F., Shelton, J. F., Shringarpure, S., Tian, C., Tung, J., Vacic, V., Wang, X., Wilson, C. H., Anderson, T., Bentley, S., Dalrymple-Alford, J., Fowdar, J., Gratten, J., Halliday, G., Henders, A. K., Hickie, I., Kassam, I., Kennedy, M., Kwok, J., Lewis, S., Mellick, G., Montgomery, G., Pearson, J., Pitcher, T., Sidorenko, J., Silburn, P. A., Vallerga, C. L., Visscher, P. M., Wallace, L., Wray, N. R., Xue, A., Yang, J., and Zhang, F. (2019). Identification of novel risk loci, causal insights, and heritable risk for parkinson's disease: a meta-analysis of genome-wide association studies. *The Lancet Neurology*, 18(12):1091–1102.

[Nguyen et al., 2011] Nguyen, H. N., Byers, B., Cord, B., Shcheglovitov, A., Byrne, J., Gujar, P., Kee, K., Schüle, B., Dolmetsch, R. E., Langston, W., Palmer, T. D., and Pera, R. R. (2011). LRRK2 mutant iPSC-derived DA neurons demonstrate increased susceptibility to oxidative stress. *Cell Stem Cell*, 8(3):267–280.

[Okita et al., 2008] Okita, K., Nakagawa, M., Hyenjong, H., Ichisaka, T., and Yamanaka, S. (2008). Generation of mouse induced pluripotent stem cells without viral vectors. *Science*, 322(5903):949–953.

[Ono et al., 2007] Ono, Y., Nakatani, T., Sakamoto, Y., Mizuhara, E., Minaki, Y., Kumai, M., Hamaguchi, A., Nishimura, M., Inoue, Y., Hayashi, H., Takahashi, J., and Imai, T. (2007). Differences in neurogenic potential in floor plate cells along an anteroposterior location: midbrain dopaminergic neurons originate from mesencephalic floor plate cells. *Development*, 134(17):3213–3225.

[Paillusson et al., 2017] Paillusson, S., Gomez-Suaga, P., Stoica, R., Little, D., Gissen, P., Devine, M. J., Noble, W., Hanger, D. P., and Miller, C. C. J. (2017). α-synuclein binds to the ER-mitochondria tethering protein VAPB to disrupt Ca^{2+} homeostasis and mitochondrial ATP production. *Acta Neuropathologica*, 134(1):129–149.

[Pankratov and Lalo, 2014] Pankratov, Y. and Lalo, U. (2014). Calcium permeability of ligand-gated Ca^{2+} channels. *European Journal of Pharmacology*, 739:60–73.

[Pasternak et al., 2012] Pasternak, B., Svanström, H., Nielsen, N. M., Fugger, L., Melbye, M., and Hviid, A. (2012). Use of calcium channel blockers and parkinson's disease. *American Journal of Epidemiology*, 175(7):627–635.

[Periasamy and Kalyanasundaram, 2007] Periasamy, M. and Kalyanasundaram, A. (2007). SERCA pump isoforms: Their role in calcium transport and disease. *Muscle & Nerve*, 35(4):430–442.

[Pinton et al., 2008] Pinton, P., Giorgi, C., Siviero, R., Zecchini, E., and Rizzuto, R. (2008). Calcium and apoptosis: ER-mitochondria Ca^{2+} transfer in the control of apoptosis. *Oncogene*, 27(50):6407–6418.

[Poulin et al., 2014] Poulin, J.-F., Zou, J., Drouin-Ouellet, J., Kim, K.-Y. A., Cicchetti, F., and Awatramani, R. B. (2014). Defining midbrain dopaminergic neuron diversity by single-cell gene expression profiling. *Cell Reports*, 9(3):930–943.

[Prakriya and Lewis, 2015] Prakriya, M. and Lewis, R. S. (2015). Store-operated calcium channels. *Physiological Reviews*, 95(4):1383–1436.

[Pringsheim et al., 2014] Pringsheim, T., Jette, N., Frolkis, A., and Steeves, T. D. (2014). The prevalence of parkinson's disease: A systematic review and meta-analysis. *Movement Disorders*, 29(13):1583–1590.

[Qi et al., 2013] Qi, L. S., Larson, M. H., Gilbert, L. A., Doudna, J. A., Weissman, J. S., Arkin, A. P., and Lim, W. A. (2013). Repurposing CRISPR as an RNA-Guided Platform for Sequence-Specific Control of Gene Expression. *Cell*, 152(5):1173–1183.

[Reczek et al., 2007] Reczek, D., Schwake, M., Schröder, J., Hughes, H., Blanz, J., Jin, X., Brondyk, W., Patten, S. V., Edmunds, T., and Saftig, P. (2007). LIMP-2 is a receptor for lysosomal mannose-6-phosphate-independent targeting of β-glucocerebrosidase. *Cell*, 131(4):770–783.

[Rizzuto et al., 1998] Rizzuto, R., Pinton, P., Carrington, W., Fay, F. S., Fogarty, K. E., Lifshitz, L. M., Tuft, R. A., and Pozzan, T. (1998). Close contacts with the endoplasmic reticulum as determinants of mitochondrial Ca^{2+} responses. *Science*, 280(5370):1763–1766.

[Roberts et al., 2015] Roberts, R. F., Wade-Martins, R., and Alegre-Abarrategui, J. (2015). Direct visualization of alpha-synuclein oligomers reveals previously undetected pathology in parkinson's disease brain. *Brain*, 138(6):1642–1657.

[Roderick et al., 2000] Roderick, H. L., Lechleiter, J. D., and Camacho, P. (2000). Cytosolic phosphorylation of calnexin controls intracellular Ca^{2+} oscillations via an interaction with serca2b. *Journal of Cell Biology*, 149(6):1235–1248.

[Rodriguez-Sabate et al., 2021] Rodriguez-Sabate, C., Gonzalez, A., Perez-Darias, J. C., Morales, I., and Rodriguez, M. (2021). The causal interaction in human basal ganglia. *Scientific Reports*, 11(1).

[Rouhani et al., 2014] Rouhani, F., Kumasaka, N., de Brito, M. C., Bradley, A., Vallier, L., and Gaffney, D. (2014). Genetic background drives transcriptional variation in human induced pluripotent stem cells. *PLoS Genet.*, 10(6):e1004432.

[Ryan et al., 2013] Ryan, S. D., Dolatabadi, N., Chan, S. F., Zhang, X., Akhtar, M. W., Parker, J., Soldner, F., Sunico, C. R., Nagar, S., Talantova, M., Lee, B., Lopez, K., Nutter, A., Shan, B., Molokanova, E., Zhang, Y., Han, X., Nakamura, T., Masliah, E., Yates, 3rd, J. R., Nakanishi, N., Andreyev, A. Y., Okamoto, S.-I., Jaenisch, R., Ambasudhan, R., and Lipton, S. A. (2013). Isogenic human iPSC parkinson's model shows nitrosative stress-induced dysfunction in MEF2-PGC1α transcription. *Cell*, 155(6):1351–1364.

[Sakai et al., 2021] Sakai, S., Watanabe, S., Komine, O., Sobue, A., and Yamanaka, K. (2021). Novel reporters of mitochondria-associated membranes (MAM), MAMtrackers, demonstrate MAM disruption as a common pathological feature in amyotrophic lateral sclerosis. *The FASEB Journal*, 35(7).

[Samanta et al., 2019] Samanta, K., Bakowski, D., Amin, N., and Parekh, A. B. (2019). The whole-cell ca2+ release-activated ca2+ current, icrac, is regulated by the mitochondrial ca2+ uniporter channel and is independent of extracellular and cytosolic na+. *The Journal of Physiology*, 598(9):1753–1773.

[Sandor et al., 2017] Sandor, C., Robertson, P., Lang, C., Heger, A., Booth, H., Vowles, J., Witty, L., Bowden, R., Hu, M., Cowley, S. A., Wade-Martins, R., and Webber, C. (2017). Transcriptomic profiling of purified patient-derived dopamine neurons identifies convergent perturbations and therapeutics for parkinson's disease. *Hum. Mol. Genet.*, 26(3):552–566.

[Sano et al., 2009] Sano, R., Annunziata, I., Patterson, A., Moshiach, S., Gomero, E., Opferman, J., Forte, M., and d'Azzo, A. (2009). GM1-ganglioside accumulation at the mitochondria-associated ER membranes links ER stress to Ca^{2+}-dependent mitochondrial apoptosis. *Molecular Cell*, 36(3):500–511.

[Schampel and Kuerten, 2017] Schampel, A. and Kuerten, S. (2017). Danger: High voltage—the role of voltage-gated calcium channels in central nervous system pathology. *Cells*, 6(4):43.

[Schöndorf et al., 2014] Schöndorf, D. C., Aureli, M., McAllister, F. E., Hindley, C. J., Mayer, F., Schmid, B., Sardi, S. P., Valsecchi, M., Hoffmann, S., Schwarz, L. K., Hedrich, U., Berg, D., Shihabuddin, L. S., Hu, J., Pruszak, J., Gygi, S. P., Sonnino, S., Gasser, T., and Deleidi, M. (2014). iPSC-derived neurons from GBA1-associated parkinson's disease patients show autophagic defects and impaired calcium homeostasis. *Nat. Commun.*, 5(1):4028.

[Schöndorf et al., 2018] Schöndorf, D. C., Ivanyuk, D., Baden, P., Sanchez-Martinez, A., De Cicco, S., Yu, C., Giunta, I., Schwarz, L. K., Di Napoli, G., Panagiotakopoulou, V., Nestel, S., Keatinge, M., Pruszak, J., Bandmann, O., Heimrich, B., Gasser, T., Whitworth, A. J., and Deleidi, M. (2018). The NAD+ precursor nicotinamide riboside rescues mitochondrial defects and neuronal loss in iPSC and fly models of parkinson's disease. *Cell Rep.*, 23(10):2976–2988.

[Shahmoradian et al., 2019] Shahmoradian, S. H., Lewis, A. J., Genoud, C., Hench, J., Moors, T. E., Navarro, P. P., Castaño-Díez, D., Schweighauser, G., Graff-Meyer, A., Goldie, K. N., Sütterlin, R., Huisman, E., Ingrassia, A., de Gier, Y., Rozemuller, A. J. M., Wang, J., Paepe, A. D., Erny, J., Staempfli, A., Hoernschemeyer, J., Großerüschkamp, F., Niedieker, D., El-Mashtoly, S. F., Quadri, M., IJcken, W. F. J. V., Bonifati, V., Gerwert, K., Bohrmann, B., Frank, S., Britschgi, M., Stahlberg, H., de Berg, W. D. J. V., and Lauer, M. E. (2019). Lewy pathology in parkinson's disease consists of crowded organelles and lipid membranes. *Nature Neuroscience*, 22(7):1099–1109.

[Shaltouki et al., 2018] Shaltouki, A., Hsieh, C.-H., Kim, M. J., and Wang, X. (2018). Alpha-synuclein delays mitophagy and targeting miro rescues neuron loss in parkinson's models. *Acta Neuropathol.*, 136(4):607–620.

[Sharifi et al., 2022] Sharifi, P., Bae, H., Gveric, D., Gentleman, S. M., Smith, P. J., Tierney, T. S., and Alavian, K. N. (2022). CAV2.3 expression is upregulated in the substantia nigra pars compacta of humans with parkinson's disease. *Brain Disorders*, 5:100031.

[Shergalis et al., 2020] Shergalis, A. G., Hu, S., Bankhead, A., and Neamati, N. (2020). Role of the ERO1-PDI interaction in oxidative protein folding and disease. *Pharmacology & Therapeutics*, 210:107525.

[Shioda et al., 2015] Shioda, N., Sawai, M., Ishizuka, Y., Shirao, T., and Fukunaga, K. (2015). Nuclear translocation of calcium/calmodulin-dependent protein kinase IIδ3 promoted by protein phosphatase-1 enhances brain-derived neurotrophic factor expression in dopaminergic neurons. *Journal of Biological Chemistry*, 290(35):21663–21675.

[Solana-Manrique et al., 2021] Solana-Manrique, C., Muñoz-Soriano, V., Sanz, F. J., and Paricio, N. (2021). Oxidative modification impairs SERCA activity in drosophila and human cell models of parkinson's disease. *Biochimica et Biophysica Acta (BBA) - Molecular Basis of Disease*, 1867(7):166152.

[Spillantini et al., 1998] Spillantini, M. G., Crowther, R. A., Jakes, R., Hasegawa, M., and Goedert, M. (1998). α-synuclein in filamentous inclusions of lewy bodies from parkinson's disease and dementia with lewy bodies. *Proceedings of the National Academy of Sciences*, 95(11):6469–6473.

[Stadtfeld et al., 2008] Stadtfeld, M., Nagaya, M., Utikal, J., Weir, G., and Hochedlinger, K. (2008). Induced pluripotent stem cells generated without viral integration. *Science*, 322(5903):945–949.

[Suzuki et al., 2014] Suzuki, J., Kanemaru, K., Ishii, K., Ohkura, M., Okubo, Y., and Iino, M. (2014). Imaging intraorganellar Ca^{2+} at subcellular resolution using CEPIA. *Nature Communications*, 5(1).

[Suzuki et al., 2017] Suzuki, S., Akamatsu, W., Kisa, F., Sone, T., Ishikawa, K.-I., Kuzumaki, N., Katayama, H., Miyawaki, A., Hattori, N., and Okano, H. (2017). Efficient induction of dopaminergic neuron differentiation from induced pluripotent stem cells reveals impaired mitophagy in PARK2 neurons. *Biochem. Biophys. Res. Commun.*, 483(1):88–93.

[Szabadkai et al., 2003] Szabadkai, G., Simoni, A. M., and Rizzuto, R. (2003). Mitochondrial Ca^{2+} uptake requires sustained Ca^{2+} release from the endoplasmic reticulum. *Journal of Biological Chemistry*, 278(17):15153–15161.

[Takahashi et al., 2007] Takahashi, K., Tanabe, K., Ohnuki, M., Narita, M., Ichisaka, T., Tomoda, K., and Yamanaka, S. (2007). Induction of pluripotent stem cells from adult human fibroblasts by defined factors. *Cell*, 131(5):861–872.

[Takahashi and Yamanaka, 2006] Takahashi, K. and Yamanaka, S. (2006). Induction of pluripotent stem cells from mouse embryonic and adult fibroblast cultures by defined factors. *Cell*, 126(4):663–676.

[Tanwar et al., 2021] Tanwar, J., Singh, J. B., and Motiani, R. K. (2021). Molecular machinery regulating mitochondrial calcium levels: The nuts and bolts of mitochondrial calcium dynamics. *Mitochondrion*, 57:9–22.

[Tian et al., 2021] Tian, R., Abarientos, A., Hong, J., Hashemi, S. H., Yan, R., Dräger, N., Leng, K., Nalls, M. A., Singleton, A. B., Xu, K., Faghri, F., and Kampmann, M. (2021). Genome-wide CRISPRi/a screens in human neurons link lysosomal failure to ferroptosis. *Nature Neuroscience*, 24(7):1020–1034.

[Tian et al., 2019] Tian, R., Gachechiladze, M. A., Ludwig, C. H., Laurie, M. T., Hong, J. Y., Nathaniel, D., Prabhu, A. V., Fernandopulle, M. S., Patel, R., Abshari, M., Ward, M. E., and Kampmann, M. (2019). CRISPR interference-based platform for multimodal genetic screens in human iPSC-derived neurons. *Neuron*, 104(2):239–255.e12.

[Vance, 1990] Vance, J. E. (1990). Phospholipid synthesis in a membrane fraction associated with mitochondria. *Journal of Biological Chemistry*, 265(13):7248–7256.

[Vicario et al., 2019] Vicario, M., Cieri, D., Vallese, F., Catoni, C., Barazzuol, L., Berto, P., Grinzato, A., Barbieri, L., Brini, M., and Calì, T. (2019). A split-GFP tool reveals differences in the sub-mitochondrial distribution of wt and mutant alpha-synuclein. *Cell Death & Disease*, 10(11).

[Visanji et al., 2013] Visanji, N. P., Brooks, P. L., Hazrati, L.-N., and Lang, A. E. (2013). The prion hypothesis in parkinson's disease: Braak to the future. *Acta Neuropathologica Communications*, 1(1).

[Vos et al., 2011] Vos, K. J. D., Mórotz, G. M., Stoica, R., Tudor, E. L., Lau, K.-F., Ackerley, S., Warley, A., Shaw, C. E., and Miller, C. C. (2011). VAPB interacts with the mitochondrial protein PTPIP51 to regulate calcium homeostasis. *Human Molecular Genetics*, 21(6):1299–1311.

[Vos et al., 2017] Vos, M., Geens, A., Böhm, C., Deaulmerie, L., Swerts, J., Rossi, M., Craessaerts, K., Leites, E. P., Seibler, P., Rakovic, A., Lohnau, T., Strooper, B. D., Fendt, S.-M., Morais, V. A., Klein, C., and Verstreken, P. (2017). Cardiolipin promotes electron transport between ubiquinone and complex i to rescue PINK1 deficiency. *Journal of Cell Biology*, 216(3):695–708.

[Wang et al., 2017] Wang, C., Ward, M. E., Chen, R., Liu, K., Tracy, T. E., Chen, X., Xie, M., Sohn, P. D., Ludwig, C., Meyer-Franke, A., Karch, C. M., Ding, S., and Gan, L. (2017). Scalable production of iPSC-derived human neurons to identify tau-lowering compounds by high-content screening. *Stem Cell Reports*, 9(4):1221–1233.

[Westermann, 2008] Westermann, B. (2008). Molecular machinery of mitochondrial fusion and fission. *Journal of Biological Chemistry*, 283(20):13501–13505.

[Williams and Fay, 1990] Williams, D. and Fay, F. (1990). Intracellular calibration of the fluorescent calcium indicator fura-2. *Cell Calcium*, 11(2-3):75–83.

[Witte et al., 2010] Witte, M. D., Kallemeijn, W. W., Aten, J., Li, K.-Y., Strijland, A., Donker-Koopman, W. E., van den Nieuwendijk, A. M. C. H., Bleijlevens, B., Kramer, G., Florea, B. I., Hooibrink, B., Hollak, C. E. M., Ottenhoff, R., Boot, R. G., van der Marel, G. A., Overkleeft, H. S., and Aerts, J. M. F. G. (2010). Ultrasensitive in situ visualization of active glucocerebrosidase molecules. *Nature Chemical Biology*, 6(12):907–913.

[Wu et al., 2013] Wu, J., Liu, L., Matsuda, T., Zhao, Y., Rebane, A., Drobizhev, M., Chang, Y.-F., Araki, S., Arai, Y., March, K., Hughes, T. E., Sagou, K., Miyata, T., Nagai, T., hong Li, W., and Campbell, R. E. (2013). Improved orange and red Ca^{2+} indicators and photophysical considerations for optogenetic applications. *ACS Chemical Neuroscience*, 4(6):963–972.

[Xu and Huang, 2020] Xu, J. and Huang, X. (2020). Lipid metabolism at membrane contacts: Dynamics and functions beyond lipid homeostasis. *Frontiers in Cell and Developmental Biology*, 8.

[Yan et al., 2005] Yan, Y., Yang, D., Zarnowska, E. D., Du, Z., Werbel, B., Valliere, C., Pearce, R. A., Thomson, J. A., and Zhang, S.-C. (2005). Directed differentiation of dopaminergic neuronal subtypes from human embryonic stem cells. *Stem Cells*, 23(6):781–790.

[Yang et al., 2020] Yang, M., Li, C., Yang, S., Xiao, Y., Xiong, X., Chen, W., Zhao, H., Zhang, Q., Han, Y., and Sun, L. (2020). Mitochondria-associated ER membranes – the origin site of autophagy. *Frontiers in Cell and Developmental Biology*, 8.

[Zambon et al., 2019] Zambon, F., Cherubini, M., Fernandes, H. J. R., Lang, C., Ryan, B. J., Volpato, V., Bengoa-Vergniory, N., Vingill, S., Attar, M., Booth, H. D. E., Haenseler, W., Vowles, J., Bowden, R., Webber, C., Cowley, S. A., and Wade-Martins, R. (2019). Cellular α-synuclein pathology is associated with bioenergetic dysfunction in parkinson's iPSC-derived dopamine neurons. *Hum. Mol. Genet.*, 28(12):2001–2013.

[Zhou et al., 2016] Zhou, Q., Yen, A., Rymarczyk, G., Asai, H., Trengrove, C., Aziz, N., Kirber, M. T., Mostoslavsky, G., Ikezu, T., Wolozin, B., and Bolotina, V. M. (2016). Impairment of PARK14-dependent Ca^{2+} signalling is a novel determinant of parkinson's disease. *Nature Communications*, 7(1).

[Zhou and Freed, 2009] Zhou, W. and Freed, C. R. (2009). Adenoviral gene delivery can reprogram human fibroblasts to induced pluripotent stem cells. *Stem Cells*, 27(11):2667–2674.